UV-assisted on-surface synthesis on metallic and insulating surfaces

Kathrin Schneider

THÈSE

En vue de l'obtention du

DOCTORAT DE L'UNIVERSITÉ DE TOULOUSE

Délivré par : *l'Université Toulouse 3 Paul Sabatier (UT3 Paul Sabatier)*

Présentée et soutenue le *27/08/2021* par :
KATHRIN SCHNEIDER

Synthèse sur surfaces conductrices et isolantes assistée par lumière UV
UV-assisted on-surface synthesis on metallic and insulating surfaces

JURY

GABOR MOLNAR	Directeur de Recherche	Président de Jury
SABINE MAIER	Professeure d'Université	Rapportrice
JÉRÔME LAGOUTE	Directeur de Recherche	Rapporteur
JACQUES BONVOISIN	Chargé de Recherche	Directeur de Thèse
VÉRONIQUE LANGLAIS	Chargée de Recherche	Membre Invité

École doctorale et spécialité :
> *SDM : Physique de la matière - CO090*

Unité de Recherche :
> *Centre d'Élaboration de Matériaux et d'Études Structurales (CEMES)- CNRS*

Directeur(s) de Thèse :
> *Jacques Bonvoisin* et *Véronique Langlais*

Rapporteurs :
> *Sabine Maier* et *Jérôme Lagoute*

Molecules are beautiful. . .

let's see if they can be useful too.

Contents

1 Introduction

Advanced functional materials are an important economic and employment generator. To achieve more ecological and energy efficient technologies, there is a need to design and simulate custom-made materials with new physical properties and performance. Covalent molecular nanostructures (CMNs), and among these graphenic nanoscale materials, exhibit tunable electronic, magnetic, optic, or chemical properties with potential relevance for applications in several fields representing societal challenges in the new digital society, like communications, energy storage or advanced material processing.

At the nanoscale, property and tunability is mainly achieved by the atomic-scale precision in structure, shape and chemical composition. In order to achieve this precision, "on-surface synthesis" (OSS) strategy is used to fabricate on a metal surface and under ultra-high vacuum conditions large, predesigned molecular structures by reactions of custom-made molecular precursors.

The main goal of this work is to explore UV light effect on the chemical reactions regarding catalytic activity enhancement of the metallic surfaces and milder conditions and to realize a direct synthesis on an ultrathin insulating film in order to decouple the reaction products from the metal.

This manuscript is organized as follows:

- The objectives, the strategy and the methodology of this work are presented in § 2.

- The determination of the growth parameter of an insulating MgO ultrathin film are detailed in § 3.

- The study of the UV light effect on the on-surface synthesis of a model system is reported in § 4.

- Finally, the results of direct synthesis on insulating surface are discussed in § 5.

2 Objectives, strategy and methodology

2.1 Objective

The main objective of this work is to achieve extended 1D covalent molecular wires directly on metallic and oxide surfaces under ultrahigh vacuum (UHV) by on-surface-synthesis and at studying their electronic properties.

2.1.1 Positioning

Using molecules as elementary building blocks is one of the most promising bottom-up strategies to achieve functional nanoarchitectures such as 1D nanowires, nanoribbons and 2D networks. Self-assembly of functional organic molecules on surfaces in ultrahigh vacuum (UHV) has been intensively studied for several decades and a large knowledge about controlling the structural order of the molecular systems on surfaces has been accumulated. In parallel to the fundamental research, molecules have been used in new technologies with an entirely new generation of ultralow-cost, lightweight and flexible electronic devices, replacing much more expensive components based on conventional semiconductor materials. Recently, technologies based on organic semiconductor devices such as organic light emitting diodes (OLEDs), organic photovoltaics (OPVs), organic field effect transistors (OFETs) and organic memory have seen major improvements and have already begun to penetrate the consumer electronic market with successful applications such as ultra-high-resolution OLED displays offering high brightness, extreme contrast ratios, rich colour reproduction and extended operating times.

2.1.1.1 Main results on molecular self-assembly

Molecules on surfaces have attracted a large scientific and technological interest over the last 40 years. The huge amount of studies, that were carried out, deals with self-assembly molecular monolayers. Indeed, molecular self-assembly allows to create highly ordered 2D arrays of organic or organometallic molecules or coordination complexes that could be either physisorbed or chemisorbed on surfaces over rather large area. Previous studies have demonstrated that the intermolecular interactions at play are rather weak, such as Van der Waals, electrostatic, metal-ligand, dipole-dipole and hydrogen or halogen bonding interactions.

Moreover, this type of nanoarrays fabrication can be also used at liquid-solid interfaces or at surfaces. At liquid-solid interface, a dynamic equilibrium between the dissolved molecules in solution and those adsorbed on the surface is established with constant adsorption and desorption dynamic. On solid surfaces (where there is no solvent) the weak intermolecular bonds can also be broken and recreated, which allows the defects self-healing identified as one of the main advantages of molecular self-assembly [1]. Of course,

the absence of solvent significantly reduces the complexity of the adsorption process as there are no molecule-solvent or solvent substrate interaction but only intermolecular and molecule-substrate interactions at play. The intermolecular interaction energy E_{int} should be slightly higher than the kinetic energy of the molecules E_{kin} to trap the molecules in a 2D matrix. Molecules should be mobile enough for defects self-healing and to form an ordered structure. The diffusion barrier E_{dif} of the molecules on the surface has to be smaller than E_{kin} to allow diffusion. In addition, to prevent desorption, the adsorption energy E_{ads} of the molecules on the substrate must be higher than E_{kin}, in summary [1]:

$$E_{ads} > E_{int} \geq E_{kin} > E_{dif}. \tag{2.1}$$

The competition between these energy values entails the appearance of a certain type of molecular arrangement over another. Further on, also kinetics play a role. If the adsorption rate is faster than the surface diffusion rate, then molecules are not able to reach the equilibrium structure and are trapped in a diffusion-limited state. On the other hand, if the adsorption rate is slower or comparable to that of surface diffusion, then a thermodynamically favoured equilibrium structure can be reached. E_{kin} is given by the substrate temperature, affecting both the thermodynamics as well as the kinetics of the system. Not only the annealing temperature but also the growth history, that is the detailed sequence of temperatures applied during and after deposition of molecules, is critical for the structuring process. Temperature control provides valuable information concerning diffusion and reaction rates, activation energies and thermodynamic parameters such as the entropy and enthalpy of various processes including surface-supported reactions and catalysis. The intermolecular interactions in self-assembled structures are characterized by non-covalent forces, mostly related with permanent or non-permanent molecular dipoles. Larger intermolecular distances yield weaker intermolecular interactions, so the surface coverage can influence the geometry of the resulting structure defining the available space per molecule on the surface. I will summarize here the main results obtained on molecule-substrate interactions (section 2.1.1.2) and on the electronic structure of organic-metal interfaces (section 2.1.1.3).

2.1.1.2 Molecule-substrate interactions

The molecular adsorption energy E_{ads}, and the diffusion energy E_{dif}, but also intermolecular interactions are directly related with the molecule-substrate interactions. If the attractive forces between molecules and substrate are stronger than those between molecules, the molecular arrangement in the self-assembled layer will be aligned along the substrate main crystallographic axes. Therefore, the molecules relative position and direction and intermolecular bond lengths in the 2D network depend on the substrate symmetry defining also the bond energy. In contrast, if the interaction with the substrate is rather weak, molecular structures follow their own symmetry and are not even disturbed by crossing step edges of the underlying substrate. Depending on temperature, STM studies have shown that in this case imaging single molecules becomes difficult because the

STM tip might sweep the molecules while scanning [2]. The adsorption energy depends on the chemical nature of the substrate and on the molecules. At step edges the interaction with the substrate is enhanced compared with an adsorption site on terraces. Strains because of a mismatch between the substrate lattice and molecular dimensions can decrease the adsorption energy. Finally, the STM tip can be used to influence the molecular growth creating new adsorption sites by applying bias pulses or enhancing the molecular transport by electric field effect on the molecules while scanning.

2.1.1.3 Electronic structure of organic-metal interfaces

Not only for molecular self-assembly but also for any metal–organic interface it is of fundamental interest to understand the rules steering electronic properties. Especially for applications towards electronic devices the determination of energy levels alignment directly at play in charge injection and transport is crucial. In the case of π-conjugated molecular film-substrate interaction, the electronic structure at metal-organic interface was initially assumed to be described by the Schottky-Mott limit originating from inorganic semiconductor interfaces as shown in fig. 2.1 (a), within the hypothesis that no significant interaction at the metal-organic interface occurs. According to this model, the organic and metal vacuum levels $E_{vac}(O)$ and $E_{vac}(M)$ are aligned and the electron-injection barrier Φ_e is done by the difference between the metal work function Φ_M and the electron affinity (EA) of the organic film, while the hole-injection barrier Φ_h is done by the difference between the ionization energy (IE) of the organic film and the metal work function Φ_M [3].
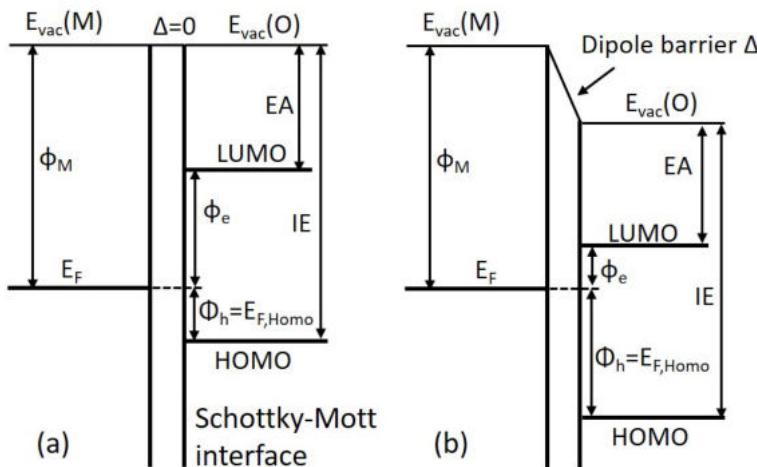
Figure 2.1 Energy diagram of an MO semiconductor interface (a) without and (b) with a dipole barrier (Δ). ϕ_e and ϕ_h are the electron and hole barriers and $E_{vac}(O)$ and $E_{vac}(M)$ are the organic and metal vacuum levels [3].

Nevertheless, the numerous studies carried out on different organic-metal systems have demonstrated that this simple description of the electronic properties at the interface could not properly describe the experimental results and thus the vacuum level alignment rule has to be revised. As it can be observed in fig. 2.1 (b), upon deposition of the first molecular layer onto the metal, an abrupt shift of E_{vac} between the metal and organic takes place

creating an interface dipole barrier Δ. Three different mechanisms might be at the origin of this effect:

- If before the interface formation the metal work function Φ_M is smaller or equal to the organic electron affinity (EA), there is a resulting electron transfer from the metal to the LUMO of the interface molecules. This lifts the organic electronic structure with respect to the metal Fermi level and creates a dipole barrier equal to an upward step of E_{vac} from the metal to the organic film. The partially occupied LUMO level relaxes into the gap, forming interface gap states above the HOMO and below E_F. The charges transferred from the metal to the organic film remain localized at the interface.

- If Φ_M falls in the molecular gap, there is no, a priori, reason for such an electron transfer, but measurements still show a dipole formation: a new organometallic complex with M-C and M-O covalent bonds is created between the metal surface atoms and the organic molecules, giving rise to a density of filled states with energy in the former gap of the organic layer. The Fermi level is pinned in the upper part of the organic gap. With the alignment of the Fermi level across the interface, a charge transfer from the organic to the metal coming from the interface states takes place. This covalent bond formation goes beyond the formation of a cation–anion pair with the transfer of a (partial) electron from the metal to the molecule, seen with alkali metal atoms for example.

- The metal work function Φ_M is lowered by the adsorbed molecules when the first monolayer of the organic material is deposited and remains at the low value for higher coverages. Φ_M is the sum of bulk and surface contributions, that is, the bulk chemical potential (μ) and surface dipole (SD). The latter depends sensitively on the surface structure and is in part set by the tail of electrons spilling out from the metal surface into the vacuum. Particularly large adsorbates such as conjugated organic molecules compress the electron tail by repulsion between the molecule electrons and the metal surface electrons and lower Φ_M (the pillow effect). This causes an abrupt downward shift of the vacuum level from the metal to the organic film at the interface and the molecular energy levels are decreased. Consequently, the hole-injection barrier is systematically increased with respect to the vacuum level alignment situation. This effect is particular important for interfaces with metals with a large SD contribution to Φ_M and is responsible for a significant fraction of the interface dipole barrier at organic-on-metal interfaces, see also [4]. In contrast interfaces with metals with a small SD contribution to Φ_M present a relatively small interface barrier.

These different mechanisms contribute to the measured interface dipole, which is the sum of various components. To understand the details helps to determine and to control the electronic structure at the interface. The dipole barrier can be oriented in different directions and is determined by the choice of the metal substrate with its specific work function Φ_M and the molecular energy levels of the adsorbate. Specific metal work functions are known from several studies and differ from and depend also on the crystallographic direction.

2.1.2 Objectives of the study

In self-assembly molecular film, the lack of strong interaction between molecules strongly limits their applications, in particular in term of electron transfer (hopping) through these self-assembled structures. Thus, creating strong molecular interactions such as covalent or coordinated bonds in self-assembly structures is of high interest and a strong motivation for research.

To address this limitation, during the past decade, on-surface-synthesis has gained increasing research attention and dozens of reactions such as Ullmann coupling [5], Glaser coupling [6], Bergman reaction [7], aryl–aryl dehydrogenation [8], Diels–Alder reaction [9], Schiff-base reaction [10], boronic acid condensation [11], cyclotretramerization [12], etc. have been successfully realized on different single crystal metal surfaces in UHV and investigated with the help of surface science techniques combined with theoretical calculations. Strong covalent bonds have been realized by homo- and heterocoupling between alkyl, alkenyl, alkynyl, aryl and other functional groups at mild conditions. The structures of the final products are dominated by the design of the molecular precursors and influenced by other conditions such as the chemical nature and lattice symmetry of the underlying substrates. It has been proved that, in most cases, the surfaces are not only used to support the reactions, but also can serve as reaction catalysts or directly participate in reactions via organometallic states. In order to reach the intrinsic properties of these on-surface-synthesized 1D wires or 2D networks, these structures should be transferred to insulators.

Up to date, only a few studies were reported on non-metallic surfaces either by direct chemical reactions on BN[9], HOPG[10], calcite[11], $H-Ge$[12] and $\gamma-Al_2O_3$[13] or by transferring the covalently bonded wires onto $NaCl$[14]. The main two emerging challenges in this field are to control the synthesis of these unique materials directly on insulating surfaces and to achieve well-defined covalently linked 2D structures on surfaces. Therefore, the aim of this work is to synthesize 1D wires on metallic and, more challenging, on insulating surfaces in order to study their intrinsic electronic properties.

2.1.3 Major Drawbacks

To fabricate covalent systems on insulating materials represents an important challenge for technological applications. The electronic properties of the adsorbates are largely quenched on a metal while they are preserved on an insulating substrate. The two major drawbacks to realize on surface synthesis on nonmetallic substrates are the weak binding energy of molecules on insulating surfaces, which is usually overcome by using low sample temperatures to enable their adsorption but is incompatible with the thermal activation of the precursors. The second one is the relative inertness of wide band gap insulating materials due to the lack of electrons at the Fermi level, therefore inducing a direct chemical reaction onto these substrates could hardly be performed.

2.2 Strategy

The complete strategy to achieve the desired products should consider the design of precursors (symmetry, size, sequential coupling, steric hindrance), the activation method (STM tip pulses, light exposition or heat), the growth parameters (substrate temperature, deposition rate, stoichiometry, coverage), the substrate (chemical nature, orientation, templating, epitaxial growth) and the supramolecular control (supramolecular template and metal coordination). Therefore, our strategy to reach our goal is to use ultrathin oxide films as decoupling layer from the metallic substrate, which allows the use of STM, and to activate Ullmann coupling between halogenated precursors by UV light and/or temperature. The different steps we will follow consist of:

- **To study the growth of an ultrathin oxide layer on top of a metallic substrate in order to control thickness, domain size and electronic properties (§ 3).**

- **To study simple precursors − model molecules, in order to characterize the different stages of the chemical reaction activated by temperature and UV light at metal surface (§ 4).**

- **To attempt direct chemical reaction between model molecules by UV light exposition at oxide surface (§ 4).**

- **To study the chemical reaction stages of more complex precursors and their properties on top of an ultrathin oxide layer with UV light (§ 5).**

2.2.1 Chemical reactions on surfaces

This approach relies on chemistry to design and to synthesize multi-functional molecules. However, some drawbacks have to be overcome to achieve devices since multi-functional molecules become large and fragile and their incorporation into solid environment remains limited to available transfer methods. Moreover, weak and reversible interactions in self-assembled molecular layers hardly provide effective intermolecular electron transport pathways. These two issues could be addressed by direct fabrication of extended molecular networks or wires on surfaces inducing covalent bonding between molecules that allows for efficient electron transport and, in addition, providing enhanced stability, in a solvent free, ultra-clean environment with a larger accessible temperature range than in solution.

To enable electron transport within the organic layer, chemical bonding has to be induced between molecular units. This could be done by using on-surface-synthesis, which consists in (1) activating the precursors by bond cleavage in order to get reactive species and (2) activating the diffusion on the surface in order to (3) induce a chemical reaction between the activated precursors (fig 2.2).

The final products obviously depend on the molecular precursors, but are also strongly influenced by the underlying substrates. Indeed, the surfaces serve as catalysts to induce
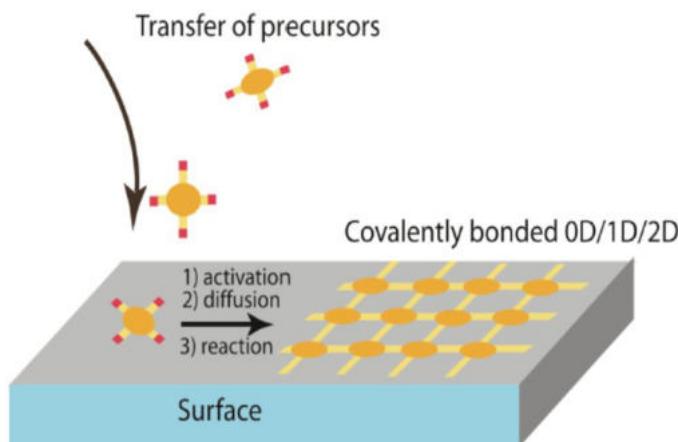
Figure 2.2 Schematic view of the steps to follow to perform on-surface synthesis

the chemical reaction and can even directly participate to the reaction with the formation of organometallic species through the incorporation of metallic adatoms. Interestingly, new species and nanoarchitectures not achievable by conventional wet chemistry can be formed by chemical reactions directly on surfaces. Up to date, a huge research effort has been dedicated on the creation of graphene nanoribbons (GNR) [13], [14] and long polyacenes [15] on different metallic surfaces. In all cases, the substrate plays an important role since the resulting products depend on its nature and its electronic and catalytic properties. The vast majority of the published studies was performed on metallic surfaces.

2.2.1.1 On metal surfaces

A number of excellent review articles has already been published on this topic,[16], [17], [18], [19], [20], [21], [22]. I will mainly refer here to 2 of them to illustrate the main results already obtained by on-surface-synthesis [17], [18]. On-surface-synthesis can be seen as an extension of heterogeneous catalysis, where the initial precursors, the intermediate states and the reaction products remain adsorbed on the surface in a submonolayer regime. This is worth to mention that this approach permits to synthesize directly on a surface polymers that could not be transferred onto the solid, as they become larger and more fragile, which limits the use of available transfer methods. In addition, the reaction takes place in a solvent free ultra-clean environment with a larger accessible temperature range than in wet chemistry. Another interesting point to underline is that intermediate states out of equilibrium could be studied by STM, while they are not accessible in solution. Finally, on-surface synthesis gives access to original reaction mechanisms under mild conditions, that would not be easily accessible in standard chemistry conditions such as the alkane polymerization, the formation of oligo-phenylene macrocycles or the synthesis of polyacenes, radialene, or arynes and these advantages are combined with the available surface science techniques, which permit to characterize each step of the reaction with atomic precision.

To provide a quick overview of the reactions that have been already successfully carried out by on-surface-synthesis, I report in fig. 2.3 a summary classified by reaction types extracted from [18].

Category	Reaction name	Chemical equation
SP⁰-C	N-heterocyclic carbenes formation and dimerization	
SP¹-C	Glaser coupling	
	Alkyne cyclotrimerization	
	Metalated carbyne	
	Bergman reaction	
	Azide-alkyne cycloaddition	
	Sonogashira coupling	
	Dehalogenative homocoupling of terminal alkynyl bromides	
SP²-C	Ullmann coupling	
	Aryl-aryl dehydrogenation coupling	
	Dehydrogenative homocoupling of terminal alkene	

Category	Reaction name	Chemical equation
	Dehalogenative homocoupling of terminal alkenyl bromides	
	Diels-Alder reaction	
SP³-C	Wurtz coupling	
	Linear alkane polymerization	
Carboxylic acid/ester/ ether/acetyls (C-O, C=O)	Decarboxylative polymerization	
	Dehydrogenative coupling	
	Dimerization and cyclotrimerization of acetyls	
	Dealkylation of ethers to alcohols	
	Reduction	
	Schiff-base reaction (imine formation)	
	Boronic acid condensation	
	Surface confined Metal-organic coordination	
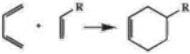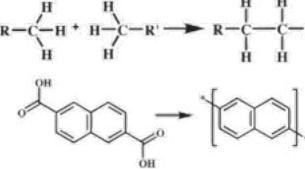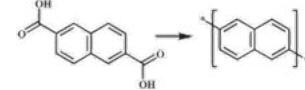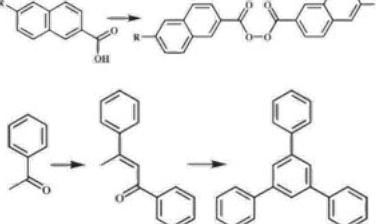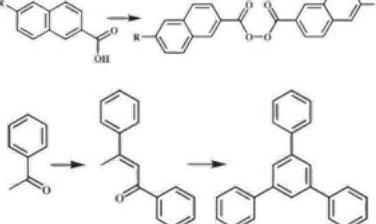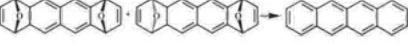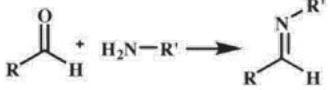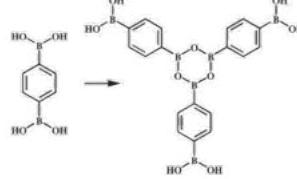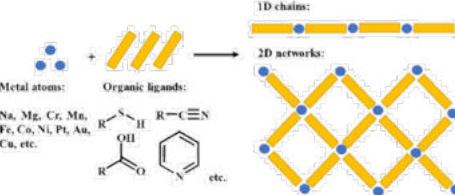
Figure 2.3 Classification and summary table of the on-surface chemical reactions. From [18]

Among these numerous reactions, the most commonly used in on-surface synthesis are dehalogenative coupling, alkyne coupling, condensation reactions, direct C-H activation and intramolecular dehydrogenation. Among them, Ullmann coupling belonging to dehalogenative reactions is the one that has been undoubtedly identified as the most efficient and robust, and has been largely and successfully used for GNR on-surface synthesis starting from different precursors with impressive results (summarized in fig. 2.4 from [17]).
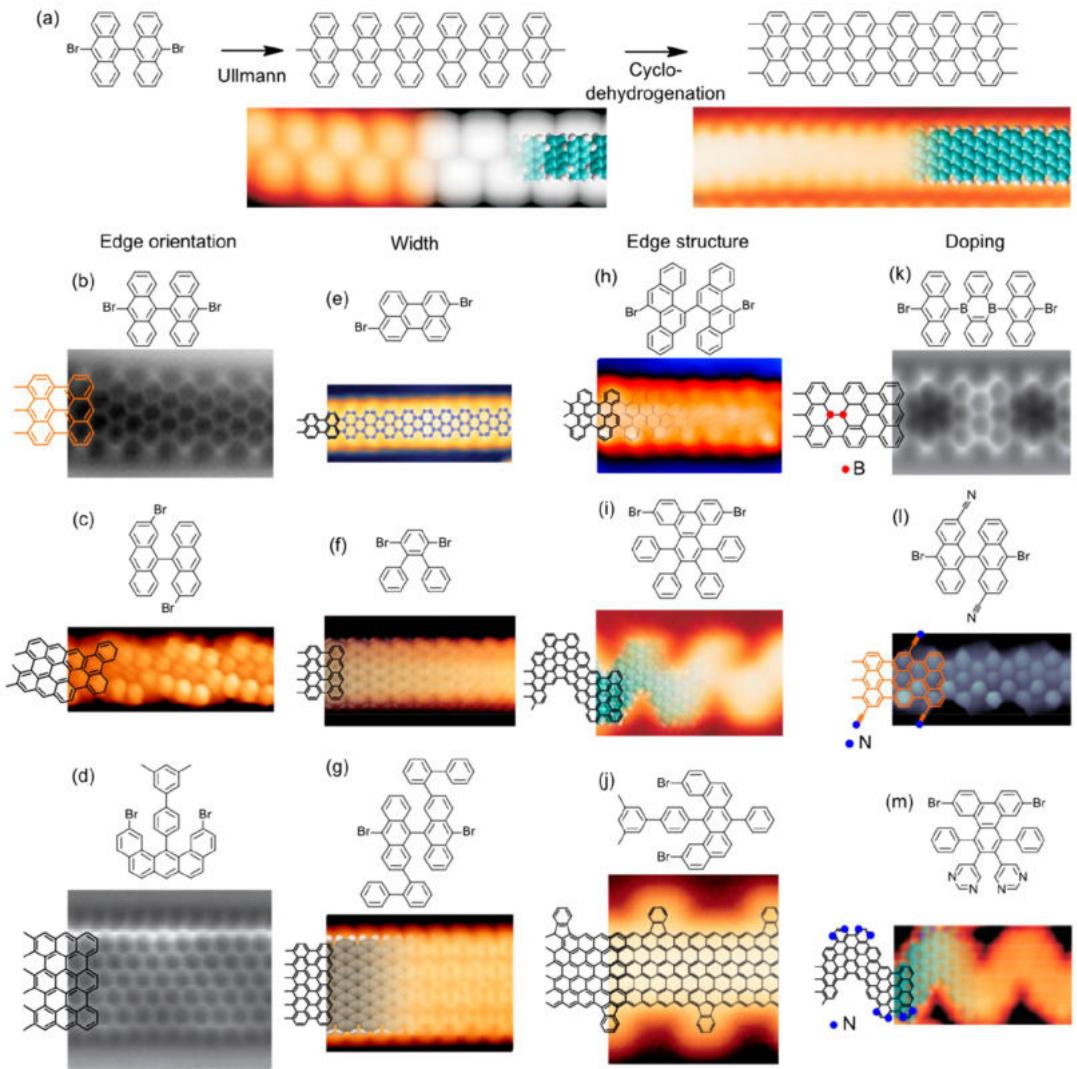
Figure 2.4 (a) Schematic representation of the reactant, intermediate polymer, and nanoribbon end product during synthesis of 7-aGNRs. Associated STM images with the overlaid models are displayed below the polymer and GNR. Different edge orientations are displayed (b, armchair; c, chiral; d, zigzag). Different widths of armchair ribbons are displayed (e, 5-aGNR; f, 9-aGNR; g, 13-aGNR). Different edge structures are shown (h, cove edge; i, chevron; j, fluoranthene functionalized zigzag edge). Differently doped structures are shown (k, boron heteroatoms; l, nitrile functional groups; m, N heteroatoms. From [17]

As reflected in fig.2.4 (a), a huge part of the research effort in this domain has been dedicated to GNRs directly synthesized on surfaces because of their intrinsic interest for many applications, but also because they demonstrate the atomic precision achievable by on-surface synthesis methods. Upon Ullmann coupling on $Au(111)$ and $Ag(111)$, the $10, 10'dibromo-9, 9'-bianthracene$ (DBBA) transforms into non-planar polymeric chains, which are converted by higher annealing temperature into 7-aGNR through a cyclode-hydrogenation process (fig. 2.4 a) [13]. Following a similar 2-step process, chevron-type GNRs were synthesized from tetraphenyl-triphenylene demonstrating the versatility of the method [13].

Other noteworthy results are those obtained by surface templating. The already 2D confined chemical reaction taking place at the surface is even more confined due to previous surface nanostructuring by employing $Cu(110)-(2x1)-O$ nanotemplate. Alternating stripes of $Cu-O$ chains and bare Cu regularly spaced on the surface permits to confine Ullmann coupling only on the bare metal producing zigzag chains, organometallic hexamers and organometallic tetramers depending on the annealing temperature and on the distance between the stripes from 4, 4"-dibromo-meta-terphenyl (DMTP) (fig. 2.5). This method enhances even more the control of the final products by including another constrain during the on-surface synthesis [23]. Other types of patterning were also proposed.
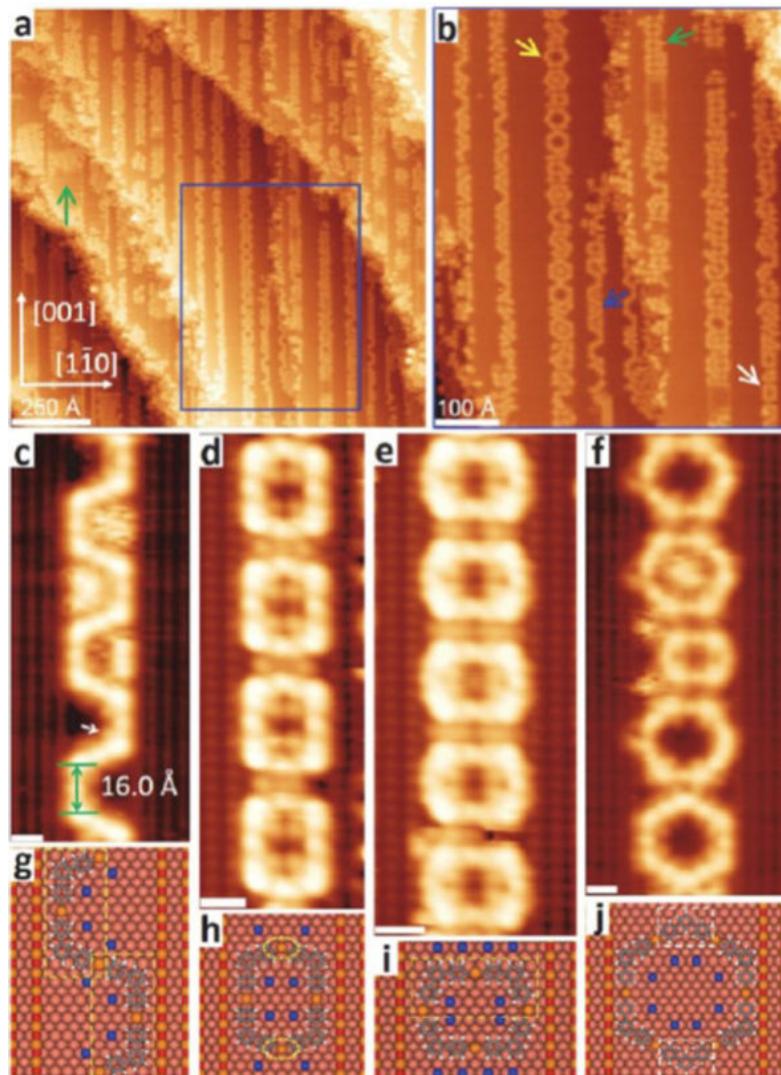
Figure 2.5 (a) Overview STM image taken after deposition of 0.22ML DMTP onto $Cu(110)-(2\times1)O(\Theta_O = 0.35\text{ML})$ held at 383K. (b)Zoom-in STM image of the blue-framed region in panel (a). The panels(c)-(f) show the magnified view of organometallic species formed on the sample in panel (a). The corresponding molecular models are shown in (g)-(j). (c,g) Section of trapezoid-wavelike oligomeric chains $(MTP-CU)_{4n}$. (d,h) Tetramer $(MTPCu)_4$. (e, i) Rotated tetramer $(MTP-Cu)_4$. (f, j) Hexamer $(MTPCu)_6$. Black spheres represent carbon atoms; white, hydrogen; blue, bromine; red, oxygen; coppery, copper atom. Tunneling parameters: (a, b) $U = 0.6\text{V}, I = 0.07\text{nA}$; (d, e) $U = 0.8\text{V}, I = 0.10\text{nA}$; (c, f) $U = 0.5\text{V}, I = 0.07\text{nA}$. From ([23].

In summary from this section, we can conclude that on metal surfaces a large amount of chemical reactions were successfully tested, among them dehalogenation reactions and in particular Ullmann coupling have attracted a special attention. Many types of GNRs were achieved and even enhanced surface confinement by nanopatterning can be used to steer the growth of oligomeric chains, tetramers and hexamers.

Finally, the parameters to take into account to design the final reaction products are (I) the precursors (size, shape and functionalization), (II) the substrate (chemical nature, orientation), (III) the growth conditions themselves (temperature, growth rate, coverage), (IV) the initiation process that depends on the functionalization of the precursors, (V) the activation process either by light exposition or activation temperature, (VI) the reaction yield or reaction type and (VII) the selectivity and product configuration.

2.2.1.2 On insulating surfaces

As I mentioned previously, much less work has been carried out on insulating surfaces. Nevertheless, some interesting studies were published on different non-metallic substrates. For example, photopolymerization of diacetylene self-assembled on a h-BN(001) surface was demonstrated to be successful resulting in long polyacetylene chains [24]. The measurements were carried out by AFM since the large band gap of this substrate prohibits the use of STM. A few examples are also found on calcite substrate, a strategy based on precursors design with a strong chemisorption of carboxylic acid groups on this surface [25] [26] [27]. This is worth to mention that dimaleimide precursors were also successfully polymerized on bulk KCl(001) surface either spontaneously or upon light irradiation [28]. Other attempts were conducted on semiconducting surfaces such as TiO_2(001) [29] [30] and passivated H-Ge(001) [31] [32] and H-Si(001) [33] with the formation of short oligomers. Another interesting alternative requiring attention is the use of ultrathin decoupling film instead of insulating bulk, which allows the use of STM imaging and spectroscopy (STS). A limited number of studies is reported using graphene or hexagonal boron-nitride (h-BN) layers [34] as well as NaCl [35] [36] and MoS_x islands [37].

2.2.1.3 Ullmann coupling

Looking through the literature, Ullmann coupling is clearly one of the most popular reactions that have been successfully used for on-surface synthesis because of its efficiency and robustness. I will describe here with more details the different steps of the reaction at a surface. This paragraph is a synthesis of the points raised in the very complete article by M. Lackinger on surface assisted Ullmann coupling [38].

Ullmann coupling is a well-known heterogeneous catalytic reaction in solution, which involves a reaction of aryl halides mediated by elemental copper established by Fritz Ullmann in 1901. In solution it has been described as an oxidative addition of copper resulting in substitution of the halogen, followed by an oxidative addition of a second aryl halide and a reductive elimination affording the biphenyl as reaction product and copper-halide as by-product.

This chemical reaction has been identified as one of the most suitable reactions for covalent bonding at solid metal surfaces under UHV conditions. The molecular building blocks usually consist of a carbon backbone functionalized with halogen side groups such as bromine or iodine. The molecules are deposited onto a reactive metal surface such as Cu, Ag, or Au. The Ullmann coupling reaction on the surface can be described by two basic reaction steps: (i) dehalogenation of the molecular building blocks and (ii) coupling of the dehalogenated monomers via $C - C$ bonds to covalent organic nanostructures. Nevertheless, an intermediate state resulting in the formation of an organometallic species is often observed depending on the metal at play (fig. 2.6).
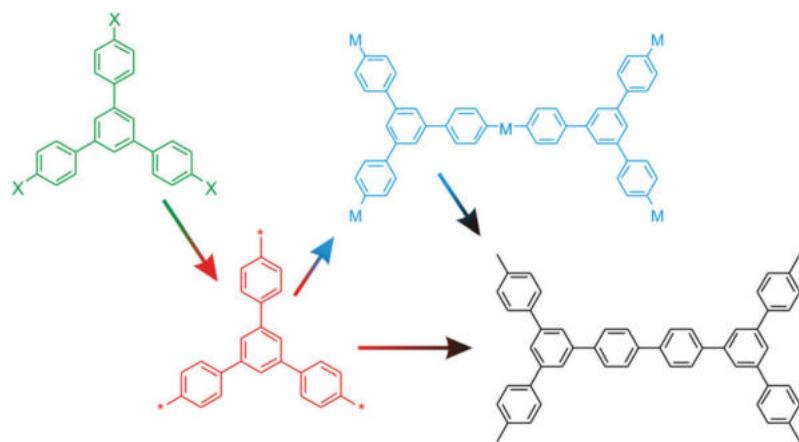

Figure 2.6 Basic reaction scheme of surface-assisted Ullmann coupling, exemplified with a three-fold triphenylbenzene precursor (depicted in green, $X : Cl, Br, I$). The surface reactivity promotes generation of an activated species by dehalogenation (depicted in red); depending on the metal surface the activated species can either recombine by directly forming $C\breve{~}C$ bonds (depicted in black) or form metastable organometallic intermediates with $C\breve{~}M\breve{~}C$ linkages (depicted in blue, M: metal atom); further annealing converts this metastable intermediate into covalent final products. From [38].

Since no side reactions occur, the products resulting from Ullmann coupling can be unambiguously identified by measuring the distance between the monomers in STM images. The existence of the organometallic species depends on the metal at play. When conducted on silver and copper substrates, the presence of adatoms yields most of time the formation of this intermediate organometallic state. On gold surface the polymers are usually formed directly without organometallic intermediate, unless a deposition of hetero-adatom was performed as in [39], where extrinsic Ag and Ni atoms were added at RT onto $Au(100)$ after the deposition of dibromo-biphenyl precursors, which immediately were converted into organometallic chains. Besides the intensive work that has been carried out on GNR's, on-surface-synthesis of 1D nanostructures by Ullmann reaction is also prominent in terms of research effort. Among the wires, poly-para-phenylene (PPP) is a classical target and remains a suitable model to study the reaction mechanism.

2.2.2 Choice of precursors

From the synthesis of the different studies that have been carried out it can be drawn already some conclusions to orient insightful choices of precursors. The first one is that

Ullmann reaction is one of the most robust and efficient coupling that can be achieved on metal surfaces through the activation of dehalogenation by the catalytic activity of the substrate. Therefore, the precursors that we will study will be halogenated precursors. The second one is that the number of halogens and the size and location of substituents are key parameters that fully determine the end product of the on-surface reaction. An excellent illustration of the role of these parameters is summarized in fig. 2.7 extracted from [38].
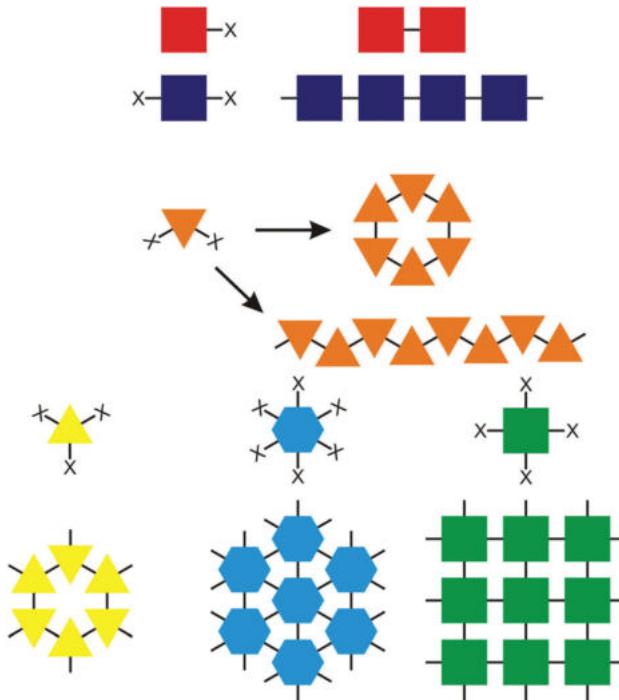

Figure 2.7 Illustration of the relation between halogen substitution pattern of precursors and dimensionality as well as topology of the resulting ideal covalent networks. X symbolises the halogens (Cl, Br, I) and the black lines indicate either $C - X$ bonds that are broken or $C - C$ bonds that are newly formed. Extracted from [38].

In order to obtain 1D wires, two different precursors were chosen. The first one is one of the simplest precursors that could be found consisting of three phenyl rings functionalized with two halogens, namely dibromo-p-terphenyl (DBTP) and diiodo-p-terphenyl (DITP), see fig. 2.8(a). They have been used in this work as model precursors to understand the different steps of the reaction and to determine the influence of the controllable parameters such as substrate temperature during deposition, deposition rate, annealing temperature, etc. The objective of this first study (detailed in § 4) is also to determine the influence of light exposure on the Ullmann reaction, since the final objective is to synthesize 1D wires on insulating layers.

The second precursor that we have chosen is a salen-type functionalized with halogens, I will name them from now on Cu-salen type and Ni-salen type (fig. 2.8(b)). The choice is based on several reasons, the first one is that the presence of metallic ion in the architecture of the precursor (coordination complex) is expected to change the molecule-surface interaction with a larger affinity towards the oxygen of an oxide than on metal. The second reason is that this kind of coordination complex precursor might present completely new
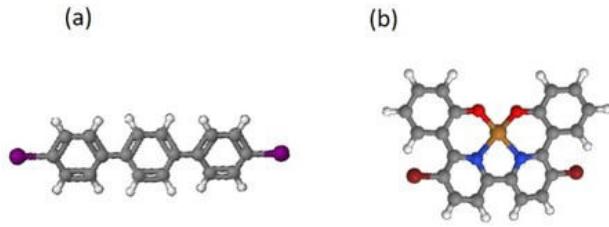
Figure 2.8 Schematic representation of the selected precursors (a) Di-halogenated-p-terphenyl, the atoms depicted in grey are C, in white H and violet halogen (I, Br). (b) di-halogenated salen-type. The atoms depicted in grey are C, in white H and dark red Br, in red oxygen, in blue N and in yellow Cu or Ni.

electronic and magnetic features due to covalent coupling upon reaction. The third reason is that this route is up to date completely unexplored (detailed in § 5).

2.2.3 Choice of MgO insulating ultrathin film

In order to be able to use STM and STS and to decouple efficiently the 1D nanowires that we plan to grow, we have explored materials presenting a wide band gap and epitaxial growth. An alternative to alkali halide films could be encountered in oxides, especially in ultrathin oxide films. Indeed, for several decades oxides have been the subject of intensive research efforts in both applied and fundamental fields. They are relevant materials from a technological point of view and have gained an enormous importance in economic world. They are widespread as robust and durable materials thanks to their chemical inertness, excellent temperature stability, high electrical resistivity and mechanical hardness. From the fundamental point of view, oxides offer an incredible richness and diversity of physical and chemical properties. The phenomena that can be studied on oxides are numerous and diverse including unusual and complex optical, structural, electronic and magnetic properties, rich phase diagram and occurrence of metal-insulator transitions as well as type II superconductivity. In this work we have focused our attention on the use of MgO ultrathin film as decoupling layer. Looking through the literature, MgO ultrathin films meet the requirements for this study with a band gap larger than 6eV even at very low coverage [40] [41]. Moreover, epitaxial growth of MgO ultrathin films has been successfully achieved on cleaved MgO(100) single crystal [42], GaAs(001)[43], Ge(001) [44], Si(100) [45], Si(111) [46], Mo(100)[47] [48] and Ag(001)[40],[49] [50] [51] [52] [53] [54] [55] [56] [57] [58] [59] [60] [61] surfaces by a number of techniques such as chemical vapor deposition, laser pulse deposition, Molecular Beam Epitaxy (MBE) and reactive deposition from an alumina crucible under oxygen partial pressure. In addition, MgO ultrathin films present other decisive advantages. The first one is their temperature stability up to 1300K [62], the second one, crucial to achieve our goal, is their relative reactivity. Indeed, Density Functional Theory (DFT) investigations conducted on CO oxidation on ultrathin MgO film grown on Ag(100) have shown that the combination of O_2 activation on this surface together with CO weak interaction converts the MgO/Ag system into an efficient catalyst at low temperature [63]. Further on, experimental evidence for the formation of O_2^- radicals was provided by electron paramagnetic resonance spectroscopy [64]. Along same idea,

other DFT calculations have shown an enhanced chemical activity for water dissociation on MgO/Ag(100) compared to bulk surface [65] and STM has been used to image the dissociation of a single water molecule adsorbed on an ultrathin MgO(001) film supported by an Ag(001) substrate [66]. Finally, the third strong argument in favour of MgO ultrathin films resides in the fact that the metallic substrate is never fully covered by the oxide letting place for chemical reaction on metal and tip sharpening procedures.

2.2.4 Photochemistry on surfaces

Shining light on solids to activate surfaces has been used for the last 40 years, especially in the domain of catalysis to enhance activity or selectivity properties of metals or oxides towards more effective dissociation of small molecules such as oxygen or water [67],[68]. Photoinduced processes of adsorbates on solid surfaces provoke a number of phenomena, that could be enumerated as (I) desorption, (II) dissociation and (III) reaction. In a number of photoinduced chemical reactions, dissociation takes place before reaction. The mechanisms at play involve different processes, either direct photon absorption by the adsorbates, or photon absorption by the substrate, or a combination of both of them. Then, in case of direct absorption by the adsorbate, electronic excitation might decay into photon emission, vibrational states de-excitation, or through other de-excitation channels opened by the presence of the substrate. When the photons are absorbed by the substrate, different phenomena might occur such as photoelectrons emission, surface plasmon, surface phonon, electron-hole creation and subsequent electron transfer to the adsorbate giving rise to negative ion resonances (NIRs) [69], [70], [71], [72]. The main advantage to use light instead of heat is to favour the polymerization process under mild conditions and to enhance selectivity promoting only certain chemical reactions.

2.2.4.1 Molecular vibrational excitation

To excite specifically vibrational transitions of an adsorbate, the light source has to be sharply in resonance with the energy of the vibrational modes, which is difficult to achieve, since the system detunes itself as soon as the excitation starts to take place. An alternative molecule-specific mechanism is to excite an energetically higher lying optically active vibrational mode of the adsorbed molecule, assuring initial specificity of the excitation. Subsequently, this high frequency mode might decay via energy transfer into low-frequency molecule-surface mode, which might result in desorption depending on the cumulated energy. However, on metal surfaces, due to direct coupling between adsorbate and substrate, the excitation relaxes faster into the heat bath provided by the solid than energy transfer into the low frequency molecule surface mode occurs, termed "resonant heating".

2.2.4.2 Molecular electronic excitation

The adsorbate-substrate complex can also be electronically excited. The system undergoes a transition from a bonding to an antibonding state. The molecule encounters a repulsive potential energy curve and is accelerated away from the surface. Then, the

excitation energy can be transferred to the metal. If this transfer occurs beyond a critical distance from the surface, it has already achieved sufficient kinetic energy to escape the ground state potential well. The process has been described by the model proposed by Menzel and Gomer [73] and Redhead [74] (MGR-model). Unfortunately, because of the ultra-short lifetime of electronically excited states in the vicinity of a metal or semiconductor substrate ($< 10^{-14}$s), the most likely event is the rapid decay of the electronically excited state, implying that the molecule returns onto the ground state potential curve after having only been slightly displaced. Consequently, due to natural lifetime distribution, only a fraction of molecules having spent a relatively long time in the excited state will have sufficient energy to escape the ground state well and to desorb or dissociate. The predominant fraction will be recaptured, reducing drastically the yield of such processes. In Antoniewicz' model, the electron is excited into a state more tightly bound to the substrate than the ground state. The consequence is that it is initially accelerated towards the surface. When returning to the ground state, kinetic energy is gained due to the steep repulsive wall of the ground state potential curve. If this energy is high enough, it can escape from the surface potential well and desorb, probably in a vibrationally and/or rotationally excited state. Like in the other scenario, only a small fraction of molecules will desorb or dissociate depending on the involved potentials and the lifetime of the excited state. Both models have in common that a short-lived electronic excitation decays into the molecule-surface vibration. However, due to short lifetimes, only a small fraction of those excited molecules, gain sufficient energy to allow bond cleavage. For the same reason, the dissociation of molecular bonds by direct adsorbate excitation occurs very rarely on metal surfaces. The origin of electronic excitation short lifetimes lies in the strong coupling of the adsorbate excited states with the nearly infinite number of electron-hole pair states provided by the substrate. Therefore, on metals, non-radiative quenching of the molecular excitation occurs most of time. The quenching rate depends on the substrate type. Nevertheless, on oxides, due to the existence of a band gap, this rate is less pronounced. Indeed, cross sections of photoinduced processes can expand over 5 orders of magnitude and decrease in the order oxides > semiconductors > noble metals [67],[68]. These conclusions support that using light to promote chemical reactions on oxide surfaces might be a successful strategy for direct polymerization.

2.2.4.3 Substrate mediated excitations

Besides direct excitation of the adsorbate or the adsorbate-substrate complex, photochemical processes can be excited via the substrate. Photoinduced plasmons characterised by low energy photon excitation can excite the adsorbate to provoke desorption or dissociation. The yield depends linearly on light intensity and, at specific frequencies, it might exponentially increase when resonance is reached related with the adsorbate size [75].

However, the creation of photoexcited free electrons, so called "hot electrons", within the substrate is the mechanism with the highest cross section, therefore, the most likely to occur. Light absorption by the metal creates electron-hole pairs. If they have sufficient energy, these electron-hole pairs are separated and so called "hot carriers" are created. By photon absorption, electrons arising from the occupied levels of the metal valence band

(VB) operate a transition towards unoccupied levels of the conduction band (CB) with an energy separation between these levels corresponding to the photon energy. Afterwards, a cascade of scattering events takes place, multiplying the number of hot electrons at lower energies. Scattering of hot electrons with others from the valence band maximum (VBM), i.e. close to the Fermi level, was found to be the dominant relaxation mechanism creating an energy distribution of hot electrons expanded over a wide energy range. Spatially, photon absorption extends over the range of the penetration depth of the incoming light. The electron mean free path, which depends on the electron energy, is of the same order. Therefore, the initial hot electrons created by photon absorption will reach the surface with high probability. On metallic surfaces, the penetration depth of photons with an energy of a few eV is in the order of 10nm corresponding to the electron mean free path at this energy [67]. The cross section of surface photoinduced processes due to hot-carrier interaction is proportional to the number of absorbed photons within a distance δ from the surface:

$$\sigma = [F(1-R)(1-e^{-\alpha\delta})]^m \qquad (2.2)$$

Where F is the number of incident photons per unit area and unit time, $(1-R)$ the absorbance, α the absorption coefficient of the metal and δ the distance from the surface. Therefore, the term $(1-e^{-\alpha\delta})$ is the fraction of photons absorbed within a distance δ from the surface, while m accounts for linear ($m=1$) or non-linear ($m \neq 1$) dependence on the incident light power [68].

The hot electrons created by metal photon absorption might then tunnel into the LUMO state of the molecules forming thus a transient anion by "Hot Electron attachment" (HEA), that leads to intramolecular bond dissociation by "Dissociative Electron Attachment" (DEA). In addition, in noble metals such as Ag strong plasmon resonances arising from the Drude-like property of sp-electrons enhance the HEA efficiency [76],[77],[78]. In fig. 2.9 two pathways of HEA are schematically depicted. In the first case, fig. 2.9 (a), the photoexcited electron created in the metallic substrate directly transfers to the LUMO generating a transient negative ion species. In the second case, fig. 2.9(b), the decay of the surface plasmon excites an electron from the HOMO to the LUMO of the adsorbate leaving the molecule in an excited state that might decay into vibrational states. An angle-resolved high-resolution electron-energy-loss-spectroscopy (AR-HREELS) study reports on a single loss energy of 3.69eV observed on Ag(100) [76], corresponding to a wavelength of 336nm.

For photon energy higher than the metal work function, photoemission occurs generating electrons with enough energy to overcome the vacuum level to be emitted by the substrate. They may also create negative ion species by resonant tunneling into an empty molecular state as well as secondary electrons with lower energies which might find themselves lower energy empty states to tunnel in.

An additional interesting feature to mention about light irradiation is that ultrathin films are transparent and their effect can be neglected when they fulfil the conditions expressed in eq. 2.3
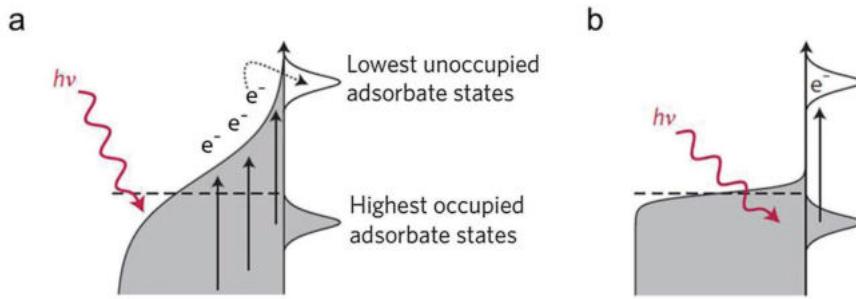
Figure 2.9 Schematic representation of HEA processes (a) photoexcited electron from the metal tunnels into the LUMO state of the molecule (b) Surface plasmon decay provoke electronic transition from the HOMO to the LUMO state. Extracted from [77].

$$\frac{d}{\sqrt{\epsilon}} \ll \lambda/4\pi \tag{2.3}$$

Where d is the thickness of the ultrathin film and ϵ is the complex dielectric constant of the film. For visible and UV regions, this condition is satisfied [79].

To conclude on this section, whatever the process at play, the adsorbed molecules will either transit through negatively charged or neutral excited species that might finally relax through Frank Condon vibrational states excitation causing bond cleavage, which is the aim here for on-surface-synthesis.

2.3 Methodology

The experimental results presented in the next chapters have been acquired in ultra-high vacuum environment (UHV) by low temperature scanning tunneling microscopy (LT-STM) at 5K (unless specified). This instrument devoted to surface science permits to follow the reaction steps with atomic precision and it's therefore the ideal technique to carry out this study. UV light from different sources is shined from outside through fused silica windows (see § 2.3.1.4 experimental setup).

2.3.1 Scanning Probe Microscopy

2.3.1.1 Principle

Scanning tunneling microscopy is based on quantum tunneling effect. This effect could be simply illustrated by two metal plates separated by a gap with a width d, this gap forms a potential barrier which prevents the electrons to pass from one plate to the other. Therefore, no any current could be measured. By applying a small potential difference between these two plates, electrons have now a certain probability to cross the potential barrier, and then a small current (I) could be measured between the metal plates. This phenomenon is known as tunneling effect.

The resolution of the Schrödinger equation within a unidimensional barrier along the z direction results in the following wavefunction: $\psi = e^{-\kappa z}$ where κ is the wavefunction

decay factor depending on the difference between the height of the potential barrier and the electron energy. For an electron at the Fermi level, this difference corresponds to the working function of the metal. The tunneling current I, which is proportional to the transmission probability, could be obtained by the square modulus of the wavefunction: $I \propto e^{-2\kappa d}$. For most of the metals, the working function being about $4 - 5\text{eV}$, the decay factor κ is about 1Å^{-1}, thereby the tunneling current I decays by one decade per angstrom as a function of the gap distance d between the electrodes. Therefore, for a distance larger than 20Å, no current could be measured. By replacing one of the two plates by a sharp metallic tip, the tunneling effect is still present but now very localized providing thus spatial resolution.

2.3.1.2 Scanning Tunneling Microscopy

In an STM, a metallic tip is used to scan the sample close to the surface ($d < 2\text{nm}$), without being in electrical contact. Ideally it is atomically sharp with only one atom at its tip apex. Both the tip and the sample have to be conductive and a bias voltage is applied between them. Since the distance is very small, the electrons can overcome the vacuum barrier and a tunnelling current is measured [80], [81].

The unidimensional square potential presented in the previous paragraph is only a very simple model, but already shows the exponential dependence between tunneling current and tip-sample distance. This strong sensitivity on the tip distance variation of the tunneling current is the key of the high spatial resolution. The precise lateral and vertical tip positioning is realized by piezoelectric tube scanners with controlled displacements smaller than 1Å. The cylindric piezo element at which end the tip is fixed can be bent and extended by an externally applied voltage [81]. The tip displacements through the piezotubes are controlled by a computer with the tip-sample distance ensured by a feedback loop. To obtain an STM image, the tip scans line by line a predefined area at regular intervals and the current and the tip height are recorded. The first setup was created by C. Binnig and H. Rohrer in 1982 [82]. A schematic drawing is shown in fig. 2.10

There are two different operation modes to record STM images [81]:

Constant height mode, illustrated in fig. 2.11 (a). In this mode the tip height is fixed at a constant value and the topography of the sample can be reconstructed out of the measured current. As the tip is very close to the surface and its height is not adjusted, there is a risk to crash into atomic steps or surface ad-atoms. Therefore, this mode can be used only for small and flat scanning areas, where there is no big change in the topography.

Constant current mode, illustrated in fig. 2.11(b). In this mode, an electrical feedback loop is used to readjust the tip height after each measuring point to keep the current constant at a preset value between some pA and a few nA. The topographical information of the sample surface is contained in the recorded tip height.

With this microscope it is also possible to perform scanning tunneling spectroscopy (STS). The tip is then positioned at a chosen location of the sample and the feedback loop is turned off, so that the distance between tip and sample is maintained constant. The bias voltage U_T is changed gradually in a predefined range and the current is recorded.
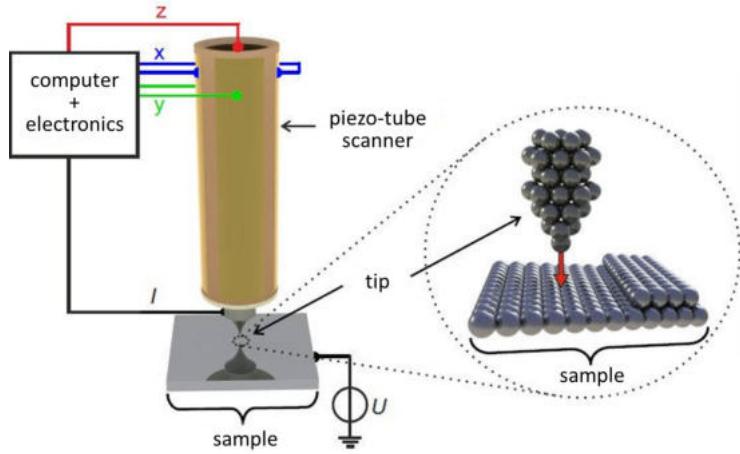
Figure 2.10 An atomically sharp tip is scanned over the sample and a bias voltage is applied. The tunnelling current is recorded. The precise tip positioning is realized by a cylindrical piezo-tube, which is bent and extended by an externally applied voltage. Both the tip positioning and the data acquisition is controlled by the electronic unit of the microscope. From J. Kügel [81].

Constant current STS could also be recorded, in this case the feedback loop is maintained active and the tip distance variation is recorded as a function of the bias voltage U_T. This second spectroscopy mode is used when damages due to high tunneling current might occur to the studied object.
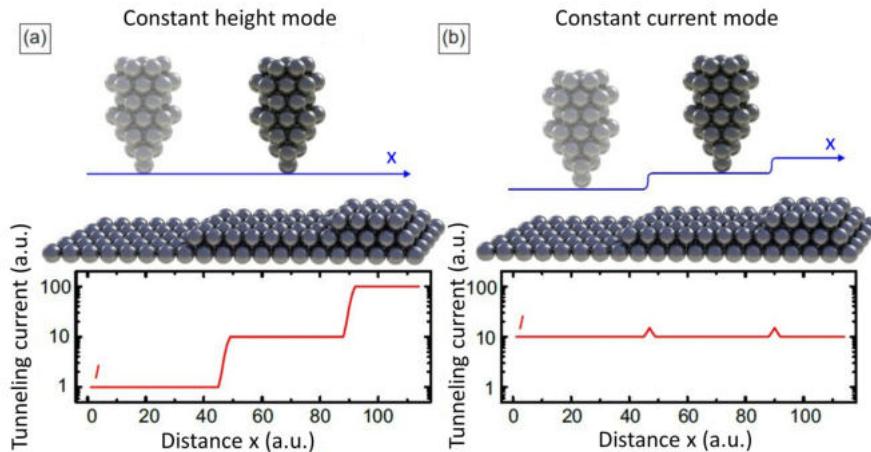

Figure 2.11 (a) Constant height mode: The tip height is fixed at a constant value, so that the topography of the sample can be reconstructed out of the measured current. In this mode there is a risk to crash the tip if there are steps on the surface, so that this mode can be applied only on flat surfaces. (b) Constant current mode: In this mode the tip height is readjusted after each measuring point by an electrical feed-back loop in order to keep the current constant. The topography is obtained with the recorded tip height. (adapted from J. Kügel [81]).

2.3.1.3 Tunneling current

In the unidimensional square potential model several details are not considered, as for example the material dependent density of states and the work functions of tip and sample.

To describe accurately the tunneling current, some corrections are required. Nevertheless, some of the simplifications are kept such as unidimensional system and considering tip and sample as ideal metals with their electronic states filled up to the Fermi energy E_F. The tip density of states is considered as energy independent [81], [83]. Fig. 2.12(a) shows the situation when no bias voltage U_T is applied. The resulting potential barrier between the tip and sample vacuum levels E_{vac} has a trapezoidal form, if the respective work functions ϕ_t and ϕ_s of tip and sample are different. d is the tip-sample distance and ρ_t and ρ_s the respective density of states of tip and sample. The two Fermi levels are aligned as long as $U_T = 0$. If a negative bias voltage is applied to the sample, 2.12(b)), the Fermi levels are shifted relatively to each other by eU_T, so that electrons arising from the occupied sample states with an energy $E_F - eU_T < E < E_F$ can tunnel into the unoccupied tip states. As it can be deduced from the equations 2.5 and 2.6 below, most of the tunneling electrons come from electronic states close to the Fermi level E_F. They encounter a smaller barrier than those in deeper energy levels. In 2.12(c) the opposite situation is sketched when a positive bias voltage is applied. Now, the electrons can tunnel from the occupied tip states into the unoccupied sample states with the energy $E_F < E < E_F + eU_T$.
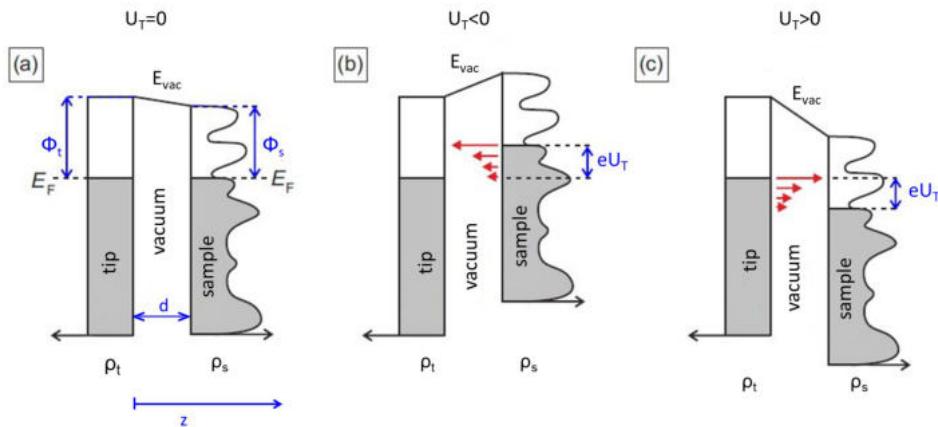

Figure 2.12 Potential barrier between tip and sample; the two electrodes with the distance d to each other have the material specific density of states ρ_t and ρ_s and work functions ϕ_t and ϕ_s. (a) No bias voltage is applied and the Fermi energies of tip and sample are aligned. (b) A negative bias voltage $U_T < 0$ is applied, so that electrons from occupied sample states can tunnel into unoccupied tip states. (c) A positive bias voltage $U_T > 0$ is applied, so that electrons from the occupied tip states can tunnel into the unoccupied sample states (adapted from J. Kügel [81]).

The topography and the density of states of the sample are two factors included in the tunneling current (see for example one of the early works of Feenstra et al. [84]). To distinguish between both, an interpretation is necessary.

To quantify the tunnelling current, the probability $|\psi(z)|^2$ for an electron of the tip with a wavefunction $\psi(z)$ to be localized at the distance z from the tip is given by [eq. 2.4]:

$$|\psi(z)|^2 = |\psi(0)|^2 e^{-2\kappa z}, \kappa = \sqrt{\frac{m_e}{\hbar^2}(\Phi_t + \Phi_s - eU_T)}. \tag{2.4}$$

This gives for the local density of states, that is the density of states per energy interval at a specific position:

$$\rho(z, E) = \sum_v |\psi_v(z)|^2 \delta(E_v - E). \tag{2.5}$$

We use the Fermi-Dirac distributions $f_t(E - eU_T)$ and $f_s(E)$ for the occupied and $1 - f_t(E - eU_T)$ and $1 - f_s(E)$ for the unoccupied tip and sample states to describe that tunneling is only possible from occupied states into unoccupied states considering both tunneling directions, from tip to sample and from sample to tip. For the tunneling current we can then write [Eq. 2.6]:

$$I_T = \frac{4\pi e}{\hbar} \int_{-\infty}^{\infty} \rho_t(E - eU_T)\rho_s(E)(f_t(E - eU_T) - f_s(E))|M(E - eU_T, E)|^2 dE \tag{2.6}$$

$$\propto \rho_t \int_0^{eU_T} \rho_s(E) dE$$

with the tunnelling matrix element [2.7]

$$|M(E - eU_T, E)|^2 = \exp\left[-2d\sqrt{\frac{m_e}{\hbar^2}(\Phi_t + \Phi_s - eU_T + 2E)}\right], \tag{2.7}$$

describing the probability of a single electron to pass from the tip to the sample or inversely [83], [85]. The second line of equation 2.7 shows the relation of the sample density of states with the tunneling current.

As U_T is small in comparison with the work functions ϕ_t and ϕ_s of tip and sample and the distance d is constant, the tunneling matrix element $|M(E - eU_T, E)|^2$ in equation 2.7 is approximately constant in the bias range. The derivative of the Fermi-Dirac distribution is a hyperbolic secant function, which is a δ-peak for low temperatures, $T \to 0$. The derivative of the tunneling current $\frac{\partial I_T}{\partial U}|_{U_T}$ at a certain value U_T is then given by for $T \to 0$ [eq. 2.8]:

$$\frac{\partial I_T}{\partial U}\Big|_{U_T} \propto \int_{-\infty}^{\infty} \rho_t(E - eU_T)\rho_s(E) \overbrace{\frac{1}{2k_BT} \text{sech}^2\left(\frac{E - eU_T}{2k_BT}\right)}^{f_s'(E - eU_T)} dE \tag{2.8}$$

$$\overset{k_BT \to 0}{=} \rho_t \int_{-\infty}^{\infty} \rho_s(E)\delta(E) dE = \rho_t \rho_s(eU_T).$$

$\frac{\partial I_\text{T}}{\partial U}|_{U_\text{T}} \propto \rho_\text{s}(eU_\text{T})$, if $T \to 0$. That means that the features in the density of states of the sample are given by the derivative of the tunneling current [83]. They can be directly visualized as function of the energy doing spectroscopy curves and calculating $\frac{\partial I_\text{T}}{\partial U}|_{U_\text{T}}$. Often a Lock-In amplifier is used to improve the signal to noise ratio applying a modulated voltage signal and obtaining directly $\rho_\text{s}(eU_\text{T})$.

From equation 2.8 it can be seen that, if $T > 0$, the density of states of the sample ρ_s is convoluted with a temperature dependent term in the integral, which is responsible for thermal broadening. This is the reason why the resolution increases by cooling the microscope down.

In equation 2.6 we considered a one-dimensional model with a well-defined tip-sample distance and an energy independent density of states of the tip. In reality, the tip density of states depending on the material (last atom at tip apex) varies with the energy . The simplification of extracting ρ_t out of the energy integral cannot always be done. Further on, the effective tip-sample distance depends on the geometric position of the atoms in the tip. More than one atom may contribute to the tunneling current. Therefore, the tip shape cannot be neglected. Despite of these difficulties, J. Tersoff and D.R. Hamann have successfully calculated the tunneling current within the simplification of an atomically sharp tip with only a single atom at the apex with a spherical s-orbital wave function [86],[87], based on first order perturbation theory results of Bardeen [88]. Further C. J. Chen et al. worked with a d-orbital tip shape model, which could explain the extremely high resolution achieved experimentally [89].

2.3.1.4 Experimental setup

The data I present in this work were obtained in a UHV experimental setup shown in fig. 2.13. The experimental setup comprises a preparation chamber equipped with classical UHV cleaning techniques such as Ar ion sputtering gun and resistive heating stage and a docking stage with 3 slots for molecular deposition to use the home-made transferable mini evaporator developed within the framework of the Interreg POCTEFA TNSI project, a schematic drawing and a picture are shown in fig. 2.14. In addition, a home-made fix evaporator with alumina crucible located in front of a quartz microbalance is dedicated to Mg evaporation. A K type-thermocouple inside the crucible allowed temperature measurement during the evaporation process. Gas microleak valves with oxygen and argon complete the equipment of the preparation chamber. A third chamber with a commercial Omicron LT-STM, a carrousel to store sample plates and tip holder and Xe introduction inlet is connected through a gate valve to the preparation chamber. The base pressure in both chambers is better than $1 * 10^{-10}$mbar.

The whole system rests on an isolated concrete floor slab and in addition pneumatic damping feet decouple the microscope from mechanical noise. The LT- STM is mounted at the bottom of a bath cryostat (4 litres), and hangs on springs for damping noise. As the cryostat can be filled either with liquid helium, or with liquid nitrogen, measurements can be performed at 4.8K and 78K.
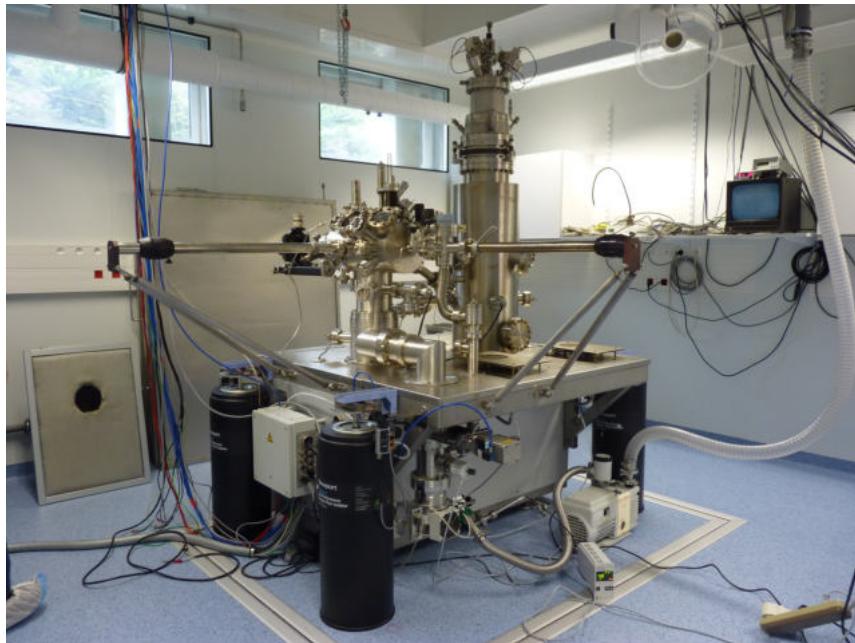
Figure 2.13 Experimental setup, ultra-high vacuum system with preparation chamber and LT-STM/AFM chamber with cryostat. The system is damped with pneumatic feet to avoid mechanical noise. Both chambers are pumped by an ion pump and a titanium sublimation pump. In addition, a turbo-pump with a primary pump installed upstream can be connected to the preparation chamber if necessary. The preparation chamber is equipped with a sputter gun, argon and oxygen leak valves, a magnesium evaporator, and a quartz micro-balance.
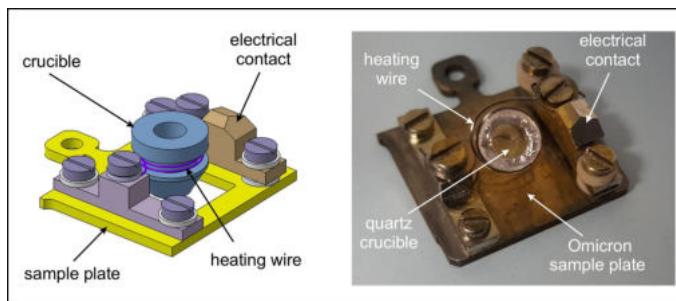

Figure 2.14 Schematic drawing (a) and picture (b) of a transferable mini evaporator for molecules. The quartz crucible is heated by a tungsten filament, the whole system mounted on a sample plate serving as support and electrical contact [90].

Two fused silica windows were mounted for UV light exposition of the sample, one in the preparation chamber and the other one in the front of the STM whose one of the cryostat windows has been holed for low temperature deposition.

2.3.1.5 Tip preparation

A tungsten wire 250μm in diameter is electrochemically etched in a 2 M NaOH solution. Then, a voltage of 1.5V is applied between the tip and an inox plate used as counter electrode, until the wire breaks at the liquid-air interface. Before introducing it into the vacuum chamber it was rinsed in deionised water and in alcohol. The tip holder shaped as a tripod is shown in fig. 2.15. The electrical contact is realized through one of the leg of the

tripod. Before introducing the tip into the microscope it was degassed at about 160°C on the heating stage in the preparation chamber. Typically, the tip has to be further prepared in the microscope to get sharper and to get rid of multiple tips and unstable parts. For this purpose, tip sharpening processes on a metal surface have to be performed.
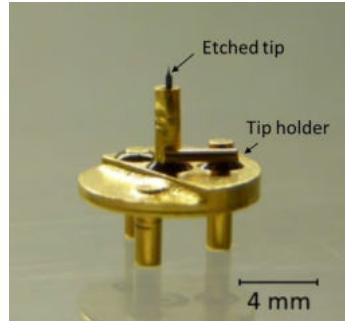

Figure 2.15 Tripod tip holder with etched tip. One leg is isolated from the metal and electrically contacted with the tip. Picture extracted from [91]

2.3.1.6 Sample preparation

Single crystal surfaces $Ag(111)$ and $Ag(001)$ were used as substrates. They were cleaned by sputtering-annealing cycles. For sputtering, the accelerated Ar-ions are focused on the sample surface. With the kinetic energy they have, they knock out the surface atoms and remove adsorbates from the surface. To get the whole sample surface cleaned, we used a combination of sputtering cycles with 600V and 1kV accelerating voltage (ion current $\sim 8-12\mu$Amp). During the sputtering process the sample was rotated by 45° with respect to the incoming ion beam to increase the efficiency of the sputtering process. To flatten the surface after the ion bombardment, the sample was subsequently heated up to 500°C. Usually for cleaning the surface 2 or 3 cycles of 30min sputtering followed by 30min annealing are necessary. The quality and cleanness of the surface was then checked by STM.

Before the deposition of MgO, the Mg-cell was carefully outgassed controlling the pressure inside the chamber. This allowed to get rid of adsorbed water molecules and to crack an eventual oxide layer at the top most surface of the Mg ingot. For ultrathin films MgO deposition, several parameters such as substrate temperature, oxygen partial pressure and deposition rate are determining the size and the quality of grown MgO islands. The deposition rate can be tuned by the heating power applied to the filament of the crucible. Fig. 2.16 shows the temperature in the crucible measured by the thermocouple as a function of the heating time for different heating power.

A strong temperature increase is observed in the first 5min until a constant temperature is reached after about 10min. To make sure to have stable and reproducible evaporating conditions, we set a preheating time of 30min and followed this procedure for every deposition. The substrate temperature is also a crucial factor regarding the growth. We noticed that during deposition both sample and crucible temperature increased by
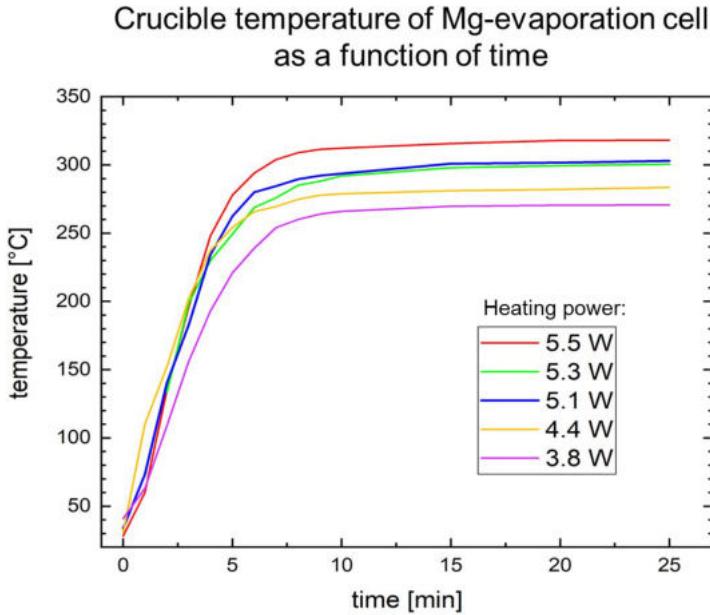
Figure 2.16 Temperature measured inside the Mg crucible by a thermocouple as a function of time for different power values. It increases strongly with time in the first 5 minutes of heating and stabilizes at a constant value after about 10min.

some degrees when positioning the sample in front of the crucible due to their mutual influence. The details of MgO deposition parameters will be given in § 3: "MgO ultrathin films growth studies".

2.3.2 UV-light

For the UV-light assisted polymerization, special fused silica windows with a high transmittance in UV were used. In fig. 2.17 the transmission curve of such a fused silica window is shown.
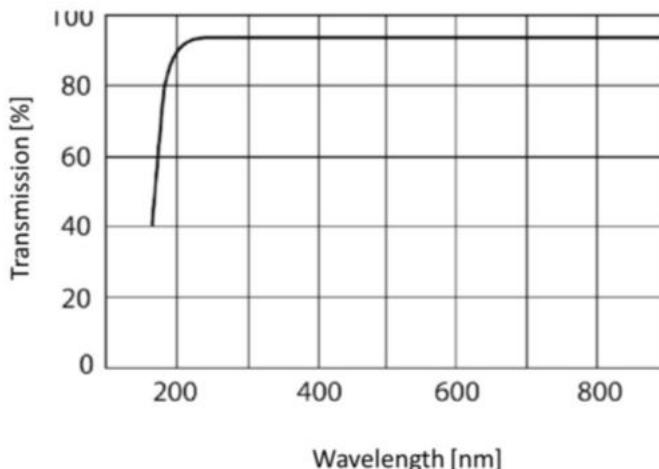

Figure 2.17 Transmission curve of a fused silica UHV window [92]

Three different light sources have been used during this work:

- A light emitting diode with an emitted wavelength of 375nm, maximum operating power of 20mW; a condenser was used to convert the divergent emitted light into a parallel beam. The system (diode + condenser) was attached directly in front of the fused silica window with a LED-Sample distance of about 20cm. The measured optical power at this distance from the LED was about 2mW.

- A Hg arc-discharge lamp, Oriel Newport, operating power 50W; the emitted wavelength spectrum is shown in fig. 2.18 (a). The emitted light was focused with a collimator to the entrance of an optical fibre (transmittance range $260 - 2200$nm), then guided in front of the window and focused on the sample. Unfortunately, most of the intensity got lost by passing through the fibre. The optical power measured at the fibre entrance was about 3mW, resulting in about 100μW at the fibre exit.

- A Xe arc-discharge lamp, Oriel Newport, operating power 150W; the emitted wavelength spectrum is shown in fig. 2.18 (b). As for the Hg arc lamp the emitted light was focused with a collimator to the entrance of an optical fibre, then guided in front of the window and focused on the sample. The optical power, measured on the entrance of the fibre, was 1.6W, resulting in 360mW at the fibre exit, probably some tens of mW reaching the sample.

The experimental setup for UV light exposure is shown in fig 2.18(c).
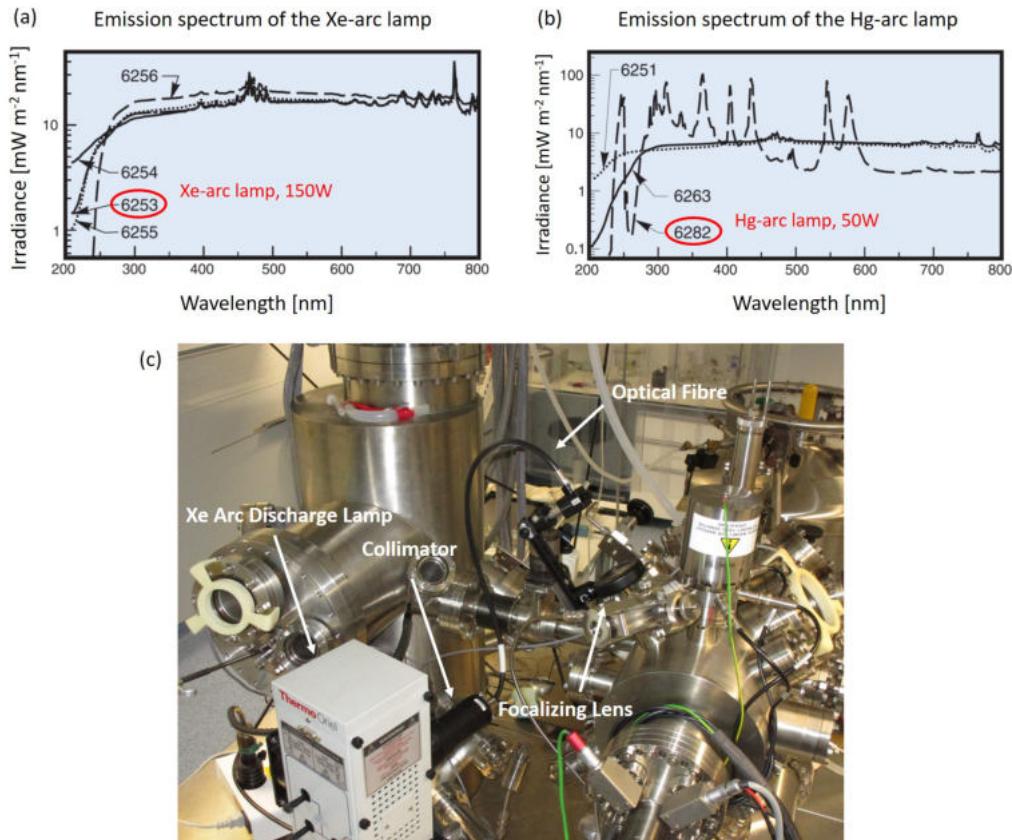
Figure 2.18 Emission spectra of the Xe (a) and Hg (b) arc-lamp. The spectrum corresponding to the lamp we have used is marked by red circle [93],(c) Experimental setup for UV-light irradiation; the light, emitted by the Xe arc-lamp, is collimated into the optical fibre entrance and guided in front of the window of the vacuum chamber. It was then focused onto the sample inside the chamber, probably some tens of mW optical power reached the sample.

3 MgO ultrathin films growth studies

Magnesium oxide crystallizes with a rock-salt structure with a lattice constant of 421.1pm [94]. The small lattice misfit (3.1%) with the (100) surface of fcc Ag renders possible the epitaxial growth of MgO thin films on top of it with MgO[100] parallel to Ag[100] [95]. Oxide films adopt a layer-by-layer growth and are pseudomorphic at the early stage, i.e. the epitaxial layer is laterally strained (compressed) in order to keep the lattice of the crystalline substrate. Above the critical thickness the strain is released through misfit dislocations with {110} glide planes relaxation. For MgO thin films the critical thickness is about $1-2$ML. For thicker films the relaxation process leads to the formation of mosaics on the film surface [49], and the lattice constant increases gradually from bulk Ag(100) to that of bulk MgO(100). The lattice constant of the film is nearly equal to that of bulk MgO for films thicker than 20ML [60]. Finally, this is worth to mention that any significant intermixing with the Ag substrate has been ruled out [62].

About the electronic structure, a wide band gap in bulk of about 7.8eV was measured by Reflection Electron Energy Loss Spectroscopy (REELS)[94]. On thin films, the band gap was experimentally measured by STS and High-Resolution Electron Energy Loss Spectroscopy (HREELS) and calculated by DFT. Defects strongly affect the electronic properties and in particular the band gap. The main defects are coloured centres such as oxygen ion vacancy (F centre) and oxygen ion vacancy $+1$ electron ($F+$) [96]. From HREELS measurements, the surface band gap width was found to be ~ 6.3eV [94], while STS on a 3ML thick film gave a band gap of about 6eV [41]. The electronic calculations of MgO monolayer show a more interesting behaviour than its bulk phase, such as decreasing the band gap from 7.8eV to 3.1eV (for GGA) and 4.2eV (for GGA-mBJ)[97].

The growth of MgO ultrathin films on Ag(100) has been studied for long by different techniques and conducted under very different conditions. Table 3.1 summarizes the growth conditions (substrate temperature, treatments, deposition rate, partial oxygen pressure, thickness) which were tested and the main results of the growth studies reported in the literature (island size, shape, coverage when indicated).

From the analysis of the literature, Mg deposition followed by post oxidation can readily be excluded. Moreover, it appears that the critical parameter is the deposition rate, for very low deposition rates, very disordered small islands presenting non-regular shapes like flakes and mosaics were observed. The best results were obtained for a substrate maintained at relatively high temperature. Therefore, we have conducted a first study by Grazing Incidence X-ray Diffraction (GIXRD) to determine the influence of the substrate temperature between 620K and 670K (see § 3.1) and a second study by LT-STM to study the influence of the deposition rate (see § 3.2).

Ref	Techn.	T_{Ag} (K)	Dep. Rate (ML/min)	P_{O_2} (mBar)	Treatments	Thick. ML	Island size (nm)	Main results
[59]	XPS, LEED	200	0.5	3×10^{-7}	Mg deposition, Post oxidation, Post annealing @700K	7		MgO + non stoichiometric species, MgO-rotational grains
[41]	STM, DFT	500	0.1-1	1×10^{-6}	Reactive deposition	1-3	10-15	1 ML-surface state@1.7 eV, Gap~4.7-6.5 eV
[98]	Nc-AFM		0.75	5×10^{-7}	Reactive deposition	4		Atomic resolution
[40]	LT-STM	500		1×10^{-6}	Reactive deposition	0.3-5	10-15, 50@2ML	Band gap 6eV@3ML
[99]	XPS, IR refl., DFT	573	1	1×10^{-6}	Reactive deposition	2, 5 and 20		Lower barrier of surface hydroxylation on ultrathin film
[49]	LEED	350	0.16	1×10^{-6}	Reactive deposition			Not well-ordered films, Mosaic formation @2ML
[100]	LT-STM	570	1	1×10^{-6}	Reactive deposition	3	5-10	Charged Au atoms on MgO films
[62]	LT-STM, HREELS	350		6.5×10^{-7}	Reactive deposition + annealing @500K			60% coverage @1ML
[101]	LT-STM	550	0.75	1×10^{-6}	Reactive deposition	4		Manipulation of charge state of defect with STM tip
[102]	LT-STM	773		2.5×10^{-7}	Reactive deposition	2		Water molecule dissociation
[103]	LT-STM	550		1×10^{-6}	Reactive deposition	1-2	5-10	Charged Au island due to electron confinement
[95]	LEED, STM	460	1	1×10^{-6}	Reactive deposition	1-20		Small islands
[50]	RHEED, Auger, EELS, UPS	450	1		Reactive deposition	1-20		Upward shift of the valence band with decreased film thickness
[52]	Auger, LEED, DFT	460	1	1×10^{-6}	Reactive deposition	1-5		Significant corrugation for 1 ML, Removed for the second layer
[51]	LEED, RT-STM	670	0.25	7×10^{-7}	Reactive deposition	1-2		Very small flake islands
[58]	RT-STM	470	1		Reactive deposition		10	Very small island + 3D pyramidal islands

Table 3.1 summary of the conditions of MgO growth on Ag(100) and main results of the studies found in the literature.

3.1 Results of GIXRD study

One of the main difficulties for growth studies is to monitor the film characteristics during the deposition. This could be achieved by Grazing Incidence X-ray Diffraction (GIXRD), which permits to analyse the structure not only once the layer is deposited but also during the growth. From the analysis of the results the lattice parameters, domain size and interface properties can be precisely extracted. This study was carried out in collaboration with Dr. Maurizio de Santis from the Néel Institute and Dr. Xavier Torrelles from the Institute of Materials Science of Barcelona (ICMAB).

The present experimental results were obtained at the European Synchrotron Radiation Facility (ESRF, Grenoble, France) with the dedicated In Situ Nanostructures and Surfaces (INS2) apparatus of the BM32 beamline. The X-ray source is a bending magnet and the monochromator is a Si(111) double crystal with the second crystal bent to give sagittal focusing on the sample. The vertical focusing is provided by two mirrors resulting in a spot size of about (0.2×0.3)mm^2. The experimental station consists of an ultrahigh vacuum chamber with base pressure in the low 10^{-10}mbar range and fully equipped for sample preparation, which is mounted on a Z-axis diffractometer. Further degrees of freedom are available to align the sample at the centre of the diffractometer with the surface normal parallel to the sample azimuthal rotation axis. The measurements were performed at photon energy of 19.8keV and at grazing incidence angle of $0.48°$ corresponding to about three times the Ag critical angle for total reflection.

The polished surface of a Ag(001) single crystal (MaTeck, Jülich, Germany) with a 10mm diameter and a miscut of less than $0.1°$ was cleaned through successive cycles of Ar^+ ion sputtering and annealing at 800K. The substrate temperature was measured using an infrared pyrometer and is eventually subject to a systematic error of a few tens of degrees at most, due to the low Ag emissivity. Cleanliness was checked by Auger electron spectroscopy (AES), such that all contaminants were below the detection limit. MgO was grown by reactive molecular beam epitaxy. Metallic Mg was evaporated by a water-cooled Knudsen cell with the chamber backfilled with molecular oxygen at a partial pressure of 1×10^{-6}mbar. The magnesium flux has been previously calibrated by using a quartz crystal microbalance. The deposition rate was about 0.2 monolayer (ML) per min, where we define 1ML as the number of atoms in a Ag(001) plane. Several samples were grown with the same nominal thickness of 0.8ML at a substrate temperature T_s of 620K, 670K and 720K, respectively. The composition was checked by AES measuring the Ag, O, and Mg Auger peaks at 356eV, 513eV and 1200eV, respectively. The samples grown at 620K and 670K give a very close MgO signal amplitude, while for that one elaborated at 720K this signal is very week showing that Mg is desorbed from the surface before a stable MgO layer can form. The growing conditions are close to those that were shown to give large flat terraces with a low defect density [40] [51], except for a bit higher temperature. On the first two samples surface x-ray diffraction (SXRD) measurements were collected at room temperature to solve the structure. The diffraction data were recorded using a 2D detector (MAXIPIX, ESRF).

SXRD is a powerful probe of the structure of crystalline surfaces. The diffracted intensity from a truncated crystal shows a sharp scattering line-shape scanning the momentum transfer parallel to the surface and a continuous line-shape in the out-of-plane direction. This out-of-plane intensity distributions at integer (HK) indexes of the surface mesh is known as (HK) crystal truncation rod (CTR)[104]. When a film grows in registry with the substrate, it gives a scattering contribution, which interferes with the substrate CTR. The film structure can then be solved by a fine analysis of these CTR intensities [105]. The surface unit-cell of Ag(001) is defined by the three vectors of a tetragonal body centred cell related to the fcc substrate, $\vec{a}_S^1 = \frac{a_{Ag}}{2}[1\bar{1}0]$, $\vec{a}_S^2 = \frac{a_{Ag}}{2}[110]$ and $\vec{a}_S^3 = a_{Ag}[001]$, with $a_{Ag} = 408.5$pm. Data were collected using the standard method for quantitative analysis. The diffractometer axes are settled to define a (HKL) node of the sample's reciprocal space, and the diffracted intensity is integrated while rocking the sample around the surface normal, which results in a ΔL portion of the CTR crossing the detector area. The structure factor amplitudes |FHKL| are then extracted by applying standard correction factors [106]. Finally, the data are averaged according to the substrate's symmetry ($P = 4$mm in our case) and the agreement factor between the structure factors of equivalent reflections is used as a systematic error estimation for the final experimental error calculation [107]. A set of 140 reflections 83, of which non-equivalents, distributed along the (10), (11), and (20) CTRs were measured on each sample with an agreement between the structure factors of equivalent reflections of 1.7% and 2.5% for the sample grown at 620K and 670K, respectively. This very good agreement between equivalent reflections allows for a reliable structural refinement, which is done comparing the calculated structure-factor amplitudes for trial models with measured ones and using a χ^2 minimization to find the best model and fit parameters. This was performed with the ROD package [105].

Figure 3.1 shows the experimental structure factor amplitudes obtained for the samples grown at 620K and 670K. The two datasets differ in the region in-between Bragg peaks suggesting a different growth mode. The data of the sample grown at lower temperature (full circles, black online) shows a bump in the middle between two Bragg peaks. In SXRD this behaviour is characteristic of a bilayer growth mode.
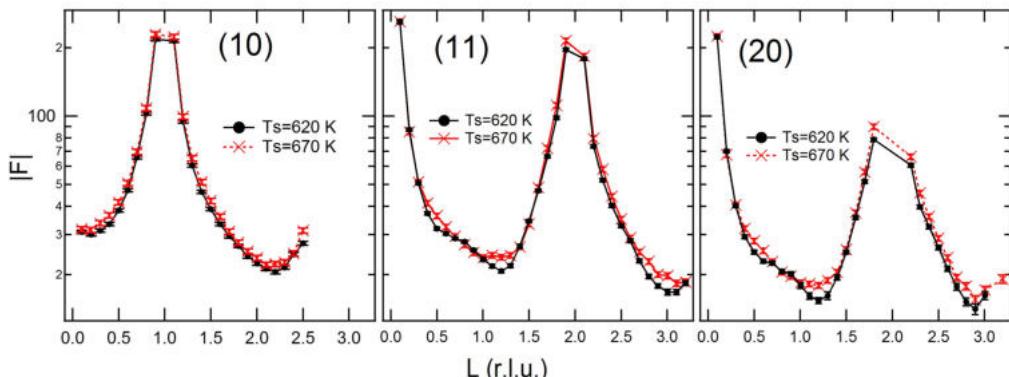

Figure 3.1 Experimental MgO/Ag(001) CTRs with error bar for the samples grown at $T_s = 620$K (filled circles, black online) and at 670K (crosses, red online). The continuous lines are plotted for eyes guide.

This is confirmed by quantitative analysis. The structural model consisting of a monoatomic thick MgO layer on top of the silver surface results in a quite bad fit giving a χ^2 of 22. The agreement improves drastically considering a bilayer growth mode (χ^2 of 3.5). In both models the interlayer spacings $d_{Ag1-Ag2}$ and $d_{Ag2-Ag3}$ and the Debye parameters B_{Ag1} and B_{Ag2} of the two Ag atomic planes closest to the interface are optimized, together with the interface spacing $d_{MgO-Ag1}$, a unique Debye parameter for MgO B_{MgO}, a roughness parameter [104] β and the MgO covered surface fraction $S_{MgO-1,2}$.

A further parameter refined in the structural analysis is the chemisorption site. The calculation was performed with oxygen on top of silver atoms and Mg on hollow sites. The refinement of a MgO bilayer with oxygen on hollow sites results in a visually relatively good agreement, but in a definitively worst quantitative one with a χ^2 of 7.2 (fig. 3.2). Other interface geometries are completely ruled out by the data. One of these configurations obtained placing both oxygen and magnesium atoms on bridge sites was previously calculated by DFT giving an intermediate energy in-between the former two [108]. This geometry was examined and results in a χ^2 of 24.

The best fit bilayer model gives an interface distance of about 280pm, quite large compared with the calculated DFT values published in literature. However, in the bilayer model less than half of the Ag surface is MgO covered. It is well known that for the clean Ag(001) surface the top-to-second-layer distance is contracted with respect to its bulk value [109]. This is, in principle, here not true for the MgO covered region. A better model resulting in a better agreement with a χ^2 of 2.3 is obtained by calculating the diffraction pattern as the sum of the contribution of a MgO island covered region and of clean Ag taking a different top Ag interlayer distance for the two regions. The top Ag interlayer distance is reduced by more than 1% in MgO-free surface regions, while it is bulk-like in covered ones. The interface Ag-O distance is then 273(4)pm. The surface fraction $S_{MgO-1,2}$ covered by the MgO bilayer is 0.38(8), in good agreement with the nominal deposition of $0.8Mg$ ML. The best fit roughness $\beta = 0.06(1)$ corresponds to a R.M.S. value of 53pm. This moderate roughness of the Ag substrate is likely to arise during the epitaxial growth of MgO as discussed in the literature [109] [110].
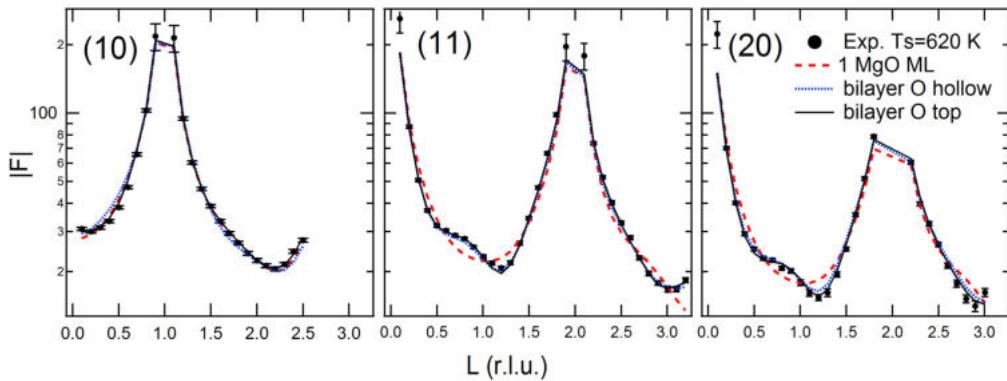

Figure 3.2 Experimental MgO/Ag(001) CTRs with error bar for the sample grown at $T_s = 620K$ (filled circles, black online) together with the fitted curves obtained with a model of 1ML MgO (dotted red), a bilayer with oxygen at hollow site (dotted blue) and a bilayer with O at top site (black line).

The interface spacing value found here is in excellent agreement but more precise than recent EXAFS measurements, that deduce a value of 270(15)pm for the Ag-O distance and it is in agreement with the related VdW-DFT estimation of 271pm obtained by the same authors for a two-layer-thick MgO/Ag(001) interface [111]. It is somewhat higher than values of 239(6)pm and 251pm found previously by other groups [52] [112]. DFT results indicate also a rumpling of a few pm of the interface with Mg ions closer to the surface Ag layer than O ones. SXRD data illustrated here are not sensitive to this rumpling, which do not improve the structure factors agreement. The best fitting parameter values are reported in table 3.2.

	MgO-covered		uncovered	bulk	Clean Ag(100) [112]
	$T_S = 620K$	$T_S = 670K$			
$S_{MgO-1,2}$	0.38(8)	0.43(8)			
S_{MgO-3}	-	0.17(4)			
$d_{Ag2-Ag3}$ (pm)	205.6(4)			204.2(5)	206(2)
$d_{Ag1-Ag2}$ (pm)	204(1)		201(1)	204.2(5)	203(2)
$d_{MgO-Ag1}$ (pm)	273(4)	271(4)	-		
$d_{MgO-MgO}$ (pm)	213(4)	212(4)	-	210.6(5)	
$B_{Ag2}(\times 10^4 \text{pm}^2)$	1.1(2)			0.66	0.95
$B_{Ag1}(\times 10^4 \text{pm}^2)$	1.5(3)			0.66	0.95
$B_{MgO}(\times 10^4 \text{pm}^2)$	0.9(6)	0.7(3)	-		
β	0.06(1)				
χ^2	1.7	2.3			

Table 3.2 Best fitting results obtained for the substrate temperatures $T_S = 620K$ and $T_S = 670K$ considering the interlayer spacings $d_{Ag1-Ag2}$, $d_{Ag2-Ag3}$ and $d_{MgO-MgO}$ and the Debye parameter B_{Ag1}, B_{Ag2}, of the two Ag atomic plane closest to the interface, the interface spacing $d_{MgO-Ag1}$, the Debye parameter B of Ag_1, Ag_2 and MgO, the roughness parameter β, and the MgO covered surface fraction $S_{MgO-1,2}$, S_{MgO-3} with the best reliability factors χ^2.

Experimental CTRs measured on the film grown at 670K suggest a different morphology. Data were fitted within the same model used for the sample grown at 620K, but with an MgO film of one monolayer thickness. The agreement is in this case quite bad, with a χ^2 of 10 or more. The agreement improves using the same bilayer model as before ($\chi^2 \sim 5$). However, it is still unsatisfactory and the simulations show a bump as for the data collected at 620K, which is not observed at 670K. Instead, the experiment agrees well with a 3D film growth model. Data were fitted considering the presence of three-monolayer-thick islands in addition to the two-monolayer thick ones, which cover almost 20% of the surface (S_{MgO-3}), obtaining a χ^2 of 1.7 (fig. 3.3). To reduce the free variables number, the Ag interlayer distances of both MgO covered and uncovered regions were kept fixed to the value found for the bilayer structure and only the interface and a unique MgO-MgO interlayer spacing ($d_{MgO-MgO}$) were optimized giving, within the error bar, identical results as for the previous sample. The only difference at 670K is the presence of a third MgO layer.
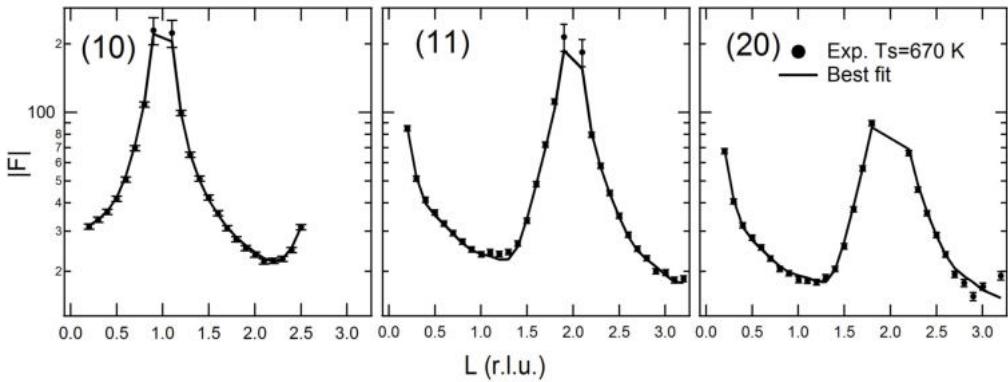
Figure 3.3 Experimental MgO/Ag(001) CTRs with error bar for the sample grown at $T_s = 670$K (filled circles) together with the best fit obtained with the parameters displayed in table 3.2 and a third MgO layer starting to grow on top of the bilayer.

From this GIXRD study we can finally conclude that for the same deposition rate of 0.2ML/min both substrate temperatures of 620K and 670K yield flat bilayer thick islands. Increasing the temperature from 620K to 670K favours $3D$ growth, since a third layer starts to appear in this case. The sticking coefficient of MgO at 720K is almost zero. The interlayer spacing between the first two layers of silver in contact with MgO is slightly expanded compared with clean silver, while the interlayer spacing of the layer 2 and 3 of silver is slightly compressed.

3.2 Results of STM study

The study of MgO growth was completed by a LT-STM study in order to check the influence of the deposition rate on the islands quality in terms of thickness, shape and electronic structure. A post annealing procedure with and without oxygen partial pressure was also studied in order to check its effect on island roughness.

The Mg was deposited from a home-made evaporator with an alumina crucible. A thermocouple type K was placed directly inside the crucible in order to monitor the temperature of the cell as a function of the heating power. The detailed procedure is described in § 2.3.1.6 sample preparation. It has to be mentioned here that the apparent thickness of the island drastically changes with the applied bias used to record the STM images. Our first study was performed at constant deposition rate calibrated at 0.3ML/min (power 3.4W) with different oxygen partial pressures and different sample temperatures.

Fig. 3.4 displays the growth conditions and the resulting STM images of the surface. For the samples A and B the surface of the islands appear to be very rough and highly defective. The islands present irregular shapes like flakes and multilayer for most of them. For sample C the oxygen partial pressure has been reduced and the islands have the expected square shape, they are rather small in size of about 15nm in average and most of them are bilayer islands with in a few cases the emergence of a third layer. Nevertheless, monolayer islands are also present (darker island in fig. 3.4(C)).

Sample	A	B	C
T_Ag(001)	620 K	670 K	670 K
Power_Mg (W)	3.4	3.4	3.4
P_O$_2$ (mbar)	$3*10^{-6}$	$3*10^{-6}$	$1.2*10^{-6}$
Deposition time	2'	2'	1'30''
T_annealing	620 K, 5'	670 K, 5'	no
O$_2$ during anneal.	yes	yes	
Result			
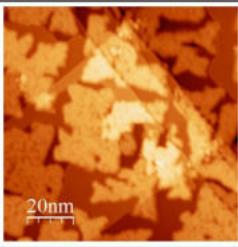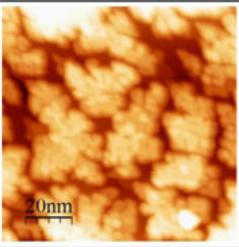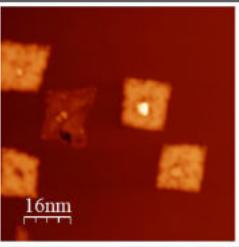
Figure 3.4 STM images of 3 MgO ultrathin film preparations with their respective growth conditions. Imaging conditions: A: 3V, 1pA; B: 3V, 1pA; C: 2V, 1pA.

From this first study we can conclude that oxygen in excess yields rough islands, whose roughness does not improve with post-annealing. The size of the islands is smaller in the case of sample C where no annealing was performed. We can conclude that a possible effect of post annealing is to render the islands larger as already reported [53]. The flake shape of the islands was attributed to fast cooling after.

A second study was then conducted as a function of the deposition rate at constant substrate temperature. This is worth to note that the power of the source is the reference and not the calibration obtained by the quartz microbalance. Indeed, the quartz crystal is water-cooled down during measurement to ensure a sticking coefficient close to 1, while the Ag(100) single crystal is maintained at 670K during deposition with a sticking coefficient which is lowered with respect to the value obtained on quartz by calibration. The results are presented in fig. 3.5. Sample D, which was grown at a power of 3.8W corresponding to ~ 0.44ML/min under 1×10^-6mbar of oxygen, presents thick flakes of MgO of more than one monolayer. Increasing the power of the source to 4.4W corresponding to 0.66ML/min (sample E) results in islands with square shape, mainly monolayer, but still rather small in size of about 20nm. Finally, the last preparation shown in fig. 3.5 F, where MgO was deposited at a power source of 5.3W corresponding to 1ML/min at a slightly smaller oxygen partial pressure of 5×10^-7mbar and annealing for 5' at 670K without oxygen, results in large flat islands at least 50nm wide. The MgO islands grown under these conditions are one monolayer thick, which was the goal to achieve of the growth study. Interestingly, the monolayer island appears at low bias as embedded into the Ag(100) substrate, which can be seen as a decisive advantage for nanowires manipulation. The MgO islands are surrounded by atomic silver atoms, which are much more reactive than silver terraces and step edges. A bias dependent study of the MgO islands grown as sample F is presented in fig. 3.6.

Sample	D	E	F
T_Ag(001)	670 K	670 K	670 K
Power_Mg (W)	3.8	4.4	5.3
P_O$_2$ (mbar)	$1*10^{-6}$	$1*10^{-6}$	$5*10^{-7}$
Deposition time	4'	6'	3'
T_annealing	no	no	670 K, 5'
O$_2$ during anneal.			no
Result			
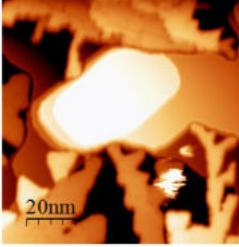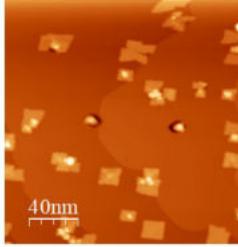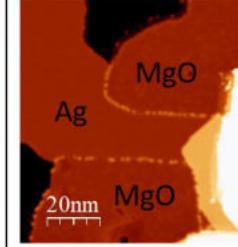
Figure 3.5 STM images and growth conditions of 3 MgO ultrathin film preparations with their respective growth conditions. Imaging conditions: D: 3V, 1pA; E: 3V, 1pA; F: −800mV, 1pA.

The apparent height of the MgO islands changes drastically as function of the applied bias used to acquire the STM images. Indeed, at low bias the islands appear as embedded into the silver substrate and the apparent height is 0Å (fig. 3.6 (a)). At a bias of 1V closer to the surface state the apparent height starts to increase to reach 0.6Å (fig. 3.6 (b)), while for scanning in the conduction band at 3V the apparent island height is about 4.45Å (fig. 3.6 (c)).
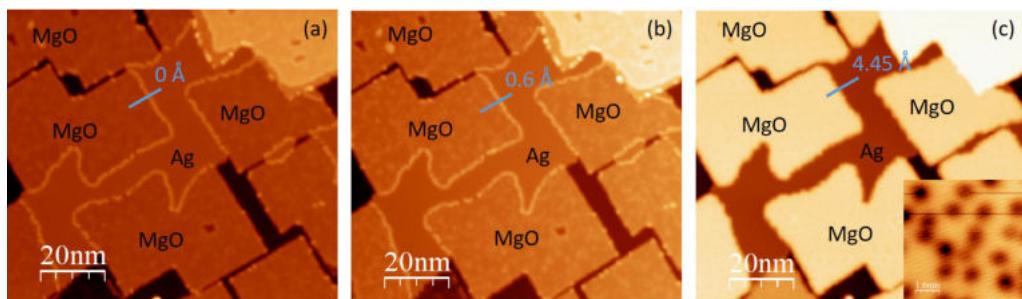
Figure 3.6 STM images of a MgO monolayer grown on Ag(100) imaged at 3 different bias (a) 0.5V, 5pA; (b) 1V, 5pA; (c) 3V, 5pA. The inset in (c) displaying MgO atomic resolution was imaged at −30mV, 90nA.

Previous studies already mentioned that some MgO islands were embedded into silver due to Ag adatom diffusion at elevated temperature [40] [58]. Valeri et al. proposed a mechanism in which in the initial deposition stage Ag atoms are partially removed from the substrate forming extended monoatomic islands atop the substrate itself [58]. From our results we can conclude, that a 100% coverage of the silver substrate cannot be reached. Ag atoms, thanks to their high mobility at 670K, always float above the MgO and the maxi-

mum monolayer coverage which can be reached is about 80% as displayed in fig. 3.6 giving rise to 82% coverage. This result is in good agreement with the reported value of largest Ag(100) fractional coverage by monoatomic MgO islands of 70% obtained by Valeri et al., but different with growth conditions (1ML/min, silver substrate temperature: 470K)[58]. A schematic representation of 2 MgO islands, one embedded into the silver substrate on the lower terrace with silver atomic species standing like a barrier between the metal and the oxide, the other island on the upper terrace, the step height corresponding to one spacing Ag layer and ML MgO, is depicted in fig. 3.7 (b). The model reproduces the $3D$ view of the experimental STM image in fig. 3.7 (a), where the flat left side is silver and the slightly corrugated right side is MgO. The corrugation of the MgO island is very small of about 30pm and the defects, namely oxygen vacant sites and impurities originating from the Ag substrate often called coloured defects, are located at the metal-oxide interface as revealed by atomic resolution STM images (see inset fig. 3.6 (c)).
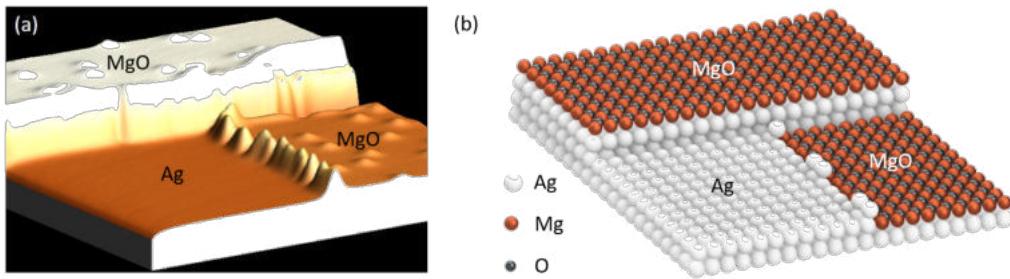
Figure 3.7 (a) $3D$ view of an STM image of an MgO monolayer island grown on Ag(100) imaged at 0.3V, 2pA. The MgO islands are always surrounded by atomic silver species; (b) schematic representation of a monolayer embedded into the silver terrace, bilayer and monolayer islands anchored at step edges.

The electronic properties of the ultrathin MgO film grown as described in fig. 3.5 F were investigated by STS. The results are displayed in fig. 3.8. The dI/dV curve recorded on the bare silver substrate (fig. 3.8 (a) - red trace) displays the expected unoccupied surface state at 1.5V, that has been previously measured by k-resolved inverse photoemission spectroscopy (KRIPES)[113]. The blue curve corresponding to the spectrum recorded on MgO monolayer (blue dot in fig. 3.8 (d)) displays a strong feature at 2.65V related to MgO state and a hardly visible interface state at ~ 1.7V, while no occupied state was measured until at least -3V giving rise to a band gap of at least 4.7eV. These results are in agreement with previous dI/dV measurements reported by Schintke et al.[40], where a value of the band gap was deduced from UPS, EELS and STS measurements to be 6eV for a 3ML thick film. In order to complete the information on the electronic structure, field emission resonances were also recorded on bare silver and on MgO monolayers (fig. 3.8 (b) and (c)). The locations of the spectroscopies are displayed in fig. 3.8 (d). The black dot was located on the upper terrace while blue and red dots location were on the same terrace. The spectroscopy of Field Emission Resonances (FER) is a sensitive technique to access to local surface potential changes. This method has been previously used to extract local work function changes in various studies on metallic surfaces partially covered by ultrathin insulating layers such as NaCl on Ag(100)[114] or FeO film on Pt(111) [114] and
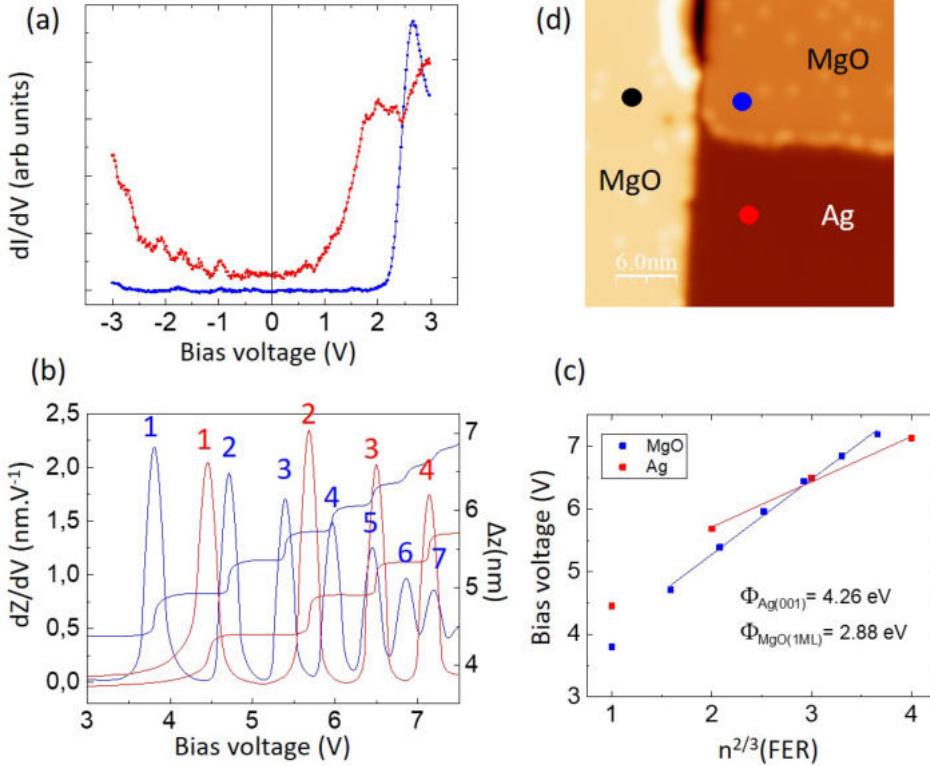
Figure 3.8 (a) Constant height dI/dV spectra recorded on bare silver substrate (red curve) and on MgO monolayer (blue curve), setpoint before opening of the feedback loop: 3V, 10pA; (b) Field Emission Resonances (FER) recorded at constant current on the bare silver substrate (red curve) and on the single MgO layer (blue curve) and the corresponding Δz displacements of the tip (right scale) (c) Plot of the FER as a function of the bias voltage (red on Ag(001) and blue (black) on MgO(001) monolayer and fitted curves in dotted lines. (d) STM image displaying the location of the STS. The black dot is located on a single MgO layer grown on an upper Ag terrace while red and blue locations are on the same lower terrace.

even on diamond single crystal [115]. It has been established in O. Yu. Kolesnychenko et al.[116] that the energy dependence of the FERs could be written as function of the local work function, the electric field F (assumed to be constant in the range of the large bias voltages) and a positive integer n representing the index of the FER for $n \gg 1$ as eq. 3.1

$$eV_n = \Phi_{LOC} + \left(\frac{3\pi\hbar e}{2\sqrt{2m}}\right)^{2/3} F^{2/3} n^{2/3} \tag{3.1}$$

Therefore, by plotting the resonance energy as a function of the n index and by fitting the resulting curve with a function of the type $y = A + b \times n^{2/3}$ the local work function value can be extracted. In our case it gives rise to a local work function of $\Phi_{MgO} = 2.88$eV and $\Phi_{Ag} = 4.26$eV. It is clear that this latest value is underestimated when comparing with the measured value on Ag(001) of 4.64eV [117]. Both values of Φ yield a lowering of the local work function of $\Delta\Phi = -1.38$eV, which is slightly higher than expected by DFT calculations and would rather correspond to a 2ML thick film[118]. Nevertheless,

looking through the literature, a number of experimental values of the local work function reduction due to MgO adsorption were reported starting from −0.4eV for a MgO single layer obtained by UPS [40] (Ultraviolet Photoemission Spectroscopy) up to −0.86eV, to −1.1eV for a single layer and −1.4eV for a double layer thick measured by KPFM (Kelvin Probe Force Microscopy)[119]. Here again, our value would rather correspond to a 2ML thick film, which could be discarded by the STM images recorded at 0.5eV. First of all, eq. 3.1 is obtained by a number of assumptions i.e the effective electrical field strength F is constant at large voltages and for $n \gg 1$ and the results strongly depend on the tip shape described as "blunt" and "sharp" in reference [116]. In addition, the results obtained by T. Jaouen et al.[120] by Auger electron diffraction and DFT values of MgO/Ag(001) work function report values from 3.3eV to 2.2eV depending on the Mg atom concentration at the Ag interface plane for one monolayer thick film. Therefore, the experimentally value obtained here is within the expected range and the contrast on the STM images recorded at 0.5eV definitively points out towards single layer thick islands. Other measurements of the work function of MgO ultrathin films carried out by nc-AFM and Kelvin Probe Force Microscopy (KPFM) give rise to work function differences between silver and MgO covered silver surface of −1.1eV and −1.4eV for an oxide single layer and a bilayer, respectively [119].

Finally, the local surface potential variation was explained as arising from 3 different mechanisms: the first one comes from charge transfer between the oxide film and the metal, a second one due to the intrinsic dipole moment that is created at the interface, and finally the third one which is due to the compression of the metal electronic density upon oxide deposition. This last one is the dominating mechanism governing the work function reduction in case of wide band gap oxide deposition as MgO[121].

3.3 Decoupling efficiency of MgO ultrathin films

From the different studies which were carried out on the MgO ultrathin film, a number of relevant electronic characteristics of the films were determined such as the persistence of a wide band gap even for monolayer thick films [94],[97],[40],[108],[122],[123], the lowering of the local work function [40],[118],[119], [120], [121] and the increased reactivity of the films with respect to MgO bulk [65], [124], [125], [66]. Nevertheless, one can wonder about the decoupling efficiency of the insulating film, since electron tunneling remains possible and charge transfer towards metallic Au and Pd islands deposited on top of ultrathin MgO films was reported through tunneling channel [103],[126], [127], [128], [129], [130]. Considering the decoupling efficiency of MgO with respect to molecules, at least two studies were reported. A comparative study was conducted on the charge transfer towards pentacenes deposited on MgO ultrathin film and directly on the metallic Ag(100) surface[131]. While fractional charge transfer occurs on the metal, this study has demonstrated that the MgO film favours integer charge transfer towards the LUMO giving rise to a Singly Occupied and a Singly Unoccupied Molecular state (SOMO and SUMO) separated by a large band gap. Remarkably, the spatial extension of the molecular states is in this case directly

accessible by STM imaging. The authors have pointed out the tunneling channel as mechanism of the charge transfer and energy levels alignment occurring when the molecules lie on this surface. The second study was carried out on single molecular magnets[132]. The integration of an ultrathin non-magnetic MgO film between $TbPc_2$ molecules and the metallic substrate has been shown to enhance the magnetic remanence and hysteresis that outperform the ones of any other surface adsorbed single molecular magnets as well as those obtained on bulk samples of $TbPc_2$. A similar effect was reported on single holmium atoms adsorbed on an ultrathin MgO film which exhibit magnetic remanence up to a temperature of 30K, a relaxation time of 1500 seconds at 10K [133],[134]. This extraordinary stability was achieved by decoupling the Ho spin by the MgO tunnel barrier. These studies tend to prove the remarkable efficiency of MgO ultrathin films as dielectric layer barrier that are not merely passive decoupling layers, but can actively influence orbital energy level alignment and charge transfer at interfaces.

3.4 Conclusion

In this study we have determined the parameters to grow large and almost defect free islands of MgO on Ag(001). From the study carried out by GIXRD, bilayer growth mode was obtained for two different substrate temperatures giving rise to islands of 50nm lateral extension with a very small roughness of $\beta = 0.06(1)$ corresponding to a R.M.S. value of 53pm. Our STM study points out the overriding role of the deposition rate to switch from the bilayer regime to the monolayer regime. The lateral extension of the islands is at least 50nm and they were found to be surrounded by silver adatoms. At low bias, the monolayer islands appear as embedded into the substrate and STS confirms their insulating character with a band gap larger than 5.5eV. Finally, the work function of the monolayer was extracted from spectroscopic data of the FERs giving rise to a work function decrease of the silver due to the presence of the MgO ultrathin film of $-1.38eV$.

This first step is of fundamental importance to get well controlled insulating films, especially since it was pointed out that the use of MgO films rather than bulk MgO presents a significant advantage as substrate in chemical reactions[102].

4 UV-light effect on poly-para-phenylene synthesis - Study versus temperature deposition

In order to obtain 1D wires, two different precursors were chosen. The first molecules are among the simplest precursors that could be found consisting of three phenyl rings functionalized with two halogens in *para* position, namely dibromo-p-terphenyl (DBTP) and diiodo-p-terphenyl (DITP), see fig. 2.8 (a). They have been used in this work as model precursors to understand the different steps of the reaction and to determine the influence of the controllable parameters such as substrate temperature during deposition, deposition rate, annealing temperature, etc. The objective of this first study on these model precursors is to determine the influence of light exposition on the Ullmann reaction, since the final objective is to synthesize these 1D wires on MgO insulating layers.

4.1 Single molecules study

This first study was carried out by depositing the precursors directly onto the Ag(100) substrate maintained at 5K in the microscope from a homemade mini transferable evaporator [90] in order to achieve information on single molecules. LT-STM images allow to identify them without ambiguity (fig. 4.1 (a)).
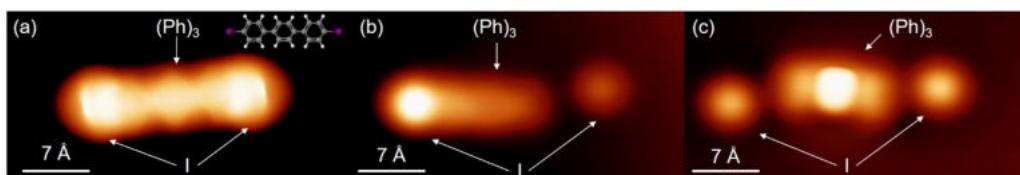
Figure 4.1 Constant height STM images (a) single DITP molecule as deposited on Ag(100); inset: schematic representation of the molecule with carbon atoms in grey, iodine atoms in pink and hydrogen atoms in white; (b) Same molecule after controlled STM tip bond cleavage of the 1st iodine; (c) Constant height image of the cleaved precursor with a Xe-functionalized tip. Imaging conditions: (a, b, c) setpoint 10pA, $100mV - \Delta Z = -7$Å, Bias= 5mV.

The intact molecule (i.e. with iodine atoms still attached) imaged at low bias (100mV) has an apparent length of about 2.13nm $\pm$ 0.01nm and an apparent height of about 0.135nm $\pm$ 0.02nm at the center, where the terphenyl group $(Ph)_3$ is located, while the iodine atoms appear as bulky feature at each extremity of the molecule with an apparent height of about 0.17nm $\pm$ 0.02nm. dI/dV bias spectroscopy recorded at the center of the molecule displays a resonant empty state at 1.9V and an occupied state around -1.8V. Constant current STM imaging at a bias of 1.9V produced a blown-up molecule keeping about the same length but displaying a much larger apparent height of about

0.2nm ± 0.02nm, in which the iodine atoms appear now lower than the organic part. This resonant state at 1.9V will be used from now on as fingerprint of the $(Ph)_3$ group to properly localize it in the organometallic phase.

Locating the STM tip above one of the iodine and applying a bias pulse at 2.3V during 300ms results in controlled bond cleavage with spatial fidelity. Indeed, only the bond onto which the bias was applied is cleaved letting the other one intact as could be seen in fig. 4.1 (b). After second bond cleavage, the constant height image recorded with a Xe-functionalized STM tip revealed the organic skeleton of the DITP precursor with bulky iodine detached at each end and the internal structure reflecting the 3 phenyl rings in between. This value of 2.3V is to put in perspective with the dissociation bond energy reported for C-I bond of 209kJ/mol (2.16eV). Attempts of iodine and phenyl rings manipulation after on surface bond cleavage were done at 5K to induce Ullmann coupling by approaching two cleaved educts without success, which tends to demonstrate the expected strong bonding of the terphenyl group with the metal surface after bond cleavage.
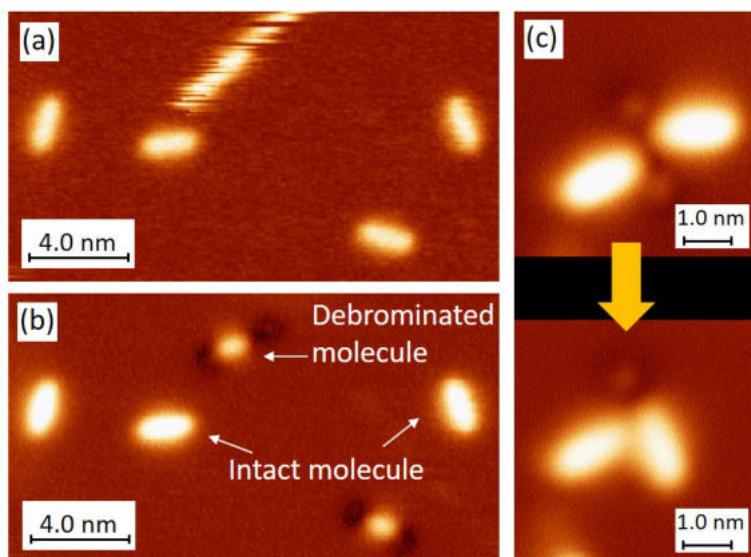
Figure 4.2 Constant current STM images of (a) 5 DBTP molecules on Ag(100) where one molecule was dragged by scanning across the surface; imaging conditions: 500mV, 1pA (b) Same molecules after controlled STM tip bond cleavage of the bromines; Imaging conditions: 1V, 1pA; (c) Intent of debrominated molecules manipulation to form a dimer. Imaging conditions 100mV, 1pA.

The same experiment was conducted with the DBTP precursors. The brominated precursors appear to be less strongly bonded to the silver substrate since the intact molecule could be dragged over the surface by scanning at 500mV, 1pA (fig. 4.2 (a)). This is worth to note that C-Br bond cleavage could be achieved in a controlled manner by STM tip pulses of 2.9V to compare with the reported dissociation bond energy of 280kJ/mol (2.9eV) presented in fig. 4.2 (b). Even if the cleavage process seems to be related with the energy of tip pulses at 3V or more, far away from the tip is also produced debromination of numerous molecules and therefore it could be related to an electric field effect. Intents of debrominated species manipulation were performed, but even if the molecules were very closely one to another, they did not react to form dimers, which might point out that a

bond together with metal atoms from the substrate was already present preventing further bonding.

In conclusion, from this study at low temperature we have learnt that the molecules are deposited in their intact architecture and therefore dehalogenation inside the crucible could be discarded. Controlled dehalogenation by tip pulses could be performed for both precursors with spatial fidelity. Further manipulations of dehalogenated species to form dimers were unsuccessful tending to prove that the reactive species react with the substrate to saturate their dangling bonds. Finally, dehalogenation of DITP was also observed by imaging single molecules at 2.3V.

4.2 Halogen bond driven molecular self-assembly

4.2.1 Nature of halogen bonds

Halogen bonds are known to be relatively strong and highly directional [135]. When a halogen atom is covalently bound to one or more atoms, its electron density is anisotropically distributed. A region of higher electron density with negative electrostatic potential forms a belt orthogonally to the covalent bond. At the extremity, a region of lower electron density and positive electrostatic potential is created. The depleted electron region is known as "σ-hole". Therefore, two regions have to be considered: the first one with an acceptor character (nucleophilic) and a second one with a donor character (electrophilic) in the same molecular species [135]. An official definition from the International Union of Pure and Applied Chemistry (IUPAC) in 2009 was given as "A halogen bond occurs when there is evidence of a net attractive interaction between an electrophilic region associated with a halogen atom in a molecular entity and a nucleophilic region in another, or the same, molecular entity." This definition attempts to unify the differently used terms "halogen bond", but other terms are also used in literature. Halogen bonds can be formed with $X = I, Br, Cl$ or F as bond donor site. The electron donor site can be one of the electronegative atoms $Y = N, O, S, Se$ and negative charged atoms I^-, Br^-, Cl^- or F^-. There are other interactions such as $R - X \cdots X - R$ between the negative charged region of one halogen $X = I, Br, Cl$ or F and the positive charged σ-hole of another one as depicted in fig. 4.3.
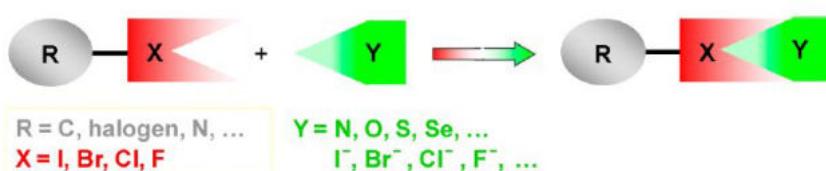

Figure 4.3   Schematic representation of halogen bond [135].

The term "halogen bond" involves a certain analogy with "hydrogen bond", where hydrogen atoms act as electrophilic regions in the interaction, whose origin is related to the charge transfer occurring between R and X atoms (fig. 4.3) due to the polarization

of the covalently bonded halogen atom. The halogen bond strength scales with the positive character of the corresponding σ-hole and increases with the polarizability of the halogen atom as bond donor atom and with its decreasing electronegativity in the order $F < Cl < Br < I$. The halogen bond donor ability of a given compound can thus be easily tuned by choosing the most convenient halogen atom and the donor site. A quite large range of interaction energies can be reached, namely by replacing an iodine atom by a bromine atom, or a chlorine atom. Fig. 4.4 shows an example of differently pronounced σ-holes, dependent on the halogen type. The less polarizable fluorine can act as bond donor only when attached to particularly strong electron-withdrawing groups. Their presence strengthens the σ-hole, leading to strong halogen bonds and the closer they are to the halogen atom, the greater the effect [135].
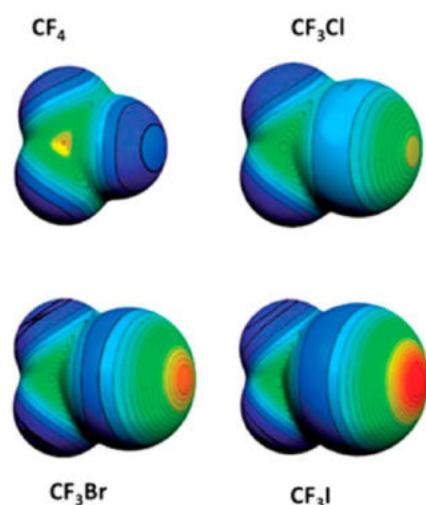
Figure 4.4 Molecular electrostatic potential at isodensity surface with 0.001au for CF_4, CF_3Cl, CF_3Br and CF_3I. Color ranges: red > 27kcal/mol, 20 > yellow > 14kcal/mol, 12 > green > 6kcal/mol and blue, negative. Extracted from [135].

The strong directionality of halogen bonds compared with hydrogen bonds is a consequence of the localization of the σ-hole exactly at covalent bond. The effective halogen atomic radius is smaller in the direction of the $R-X$ bond axis than perpendicular to it. This smaller effective radius corresponds to the σ-hole, which is well confined on the elongation of the $R-X$ bond axis and which confines the angle in which the nucleophile enters into the interaction. Short and strong halogen bonds are more directional than the long and weak ones. $R-X\cdots X-R$ contacts (X= halogen atom) occur preferentially according to two different geometries, which can be classified as type I and type II, defined by the angles θ_1 and θ_2 between the directions of the halogen bond $X\cdots X$ and the covalent bond $R-X$ to the molecular moiety. Type I interactions are symmetrical, $\theta_1 = \theta_2$, geometry-based contacts, that arise from close-packing requirements, though, according to the IUPAC definition, they are no halogen bonds. Type II interactions have a bent geometry, $\theta_1 = 90°$, $\theta_2 = 180°$ and arise from the pairing between the electrophilic area on one halogen atom and the nucleophilic area on the other one. Fig. 4.5 shows both geometry types. Type II contacts are more favoured in iodinated than in brominated derivatives [135].
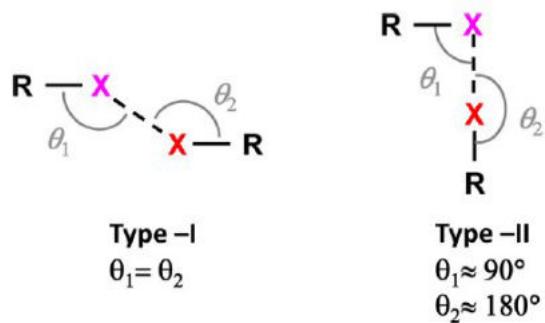
Figure 4.5 Structural scheme of type I and type II halogen contacts. Extracted from [135]

On surfaces, despite of their high directionality, halogen-bond directions can be determined by the interactions of the molecules with the substrate, in particular its crystallographic axes and symmetry. In addition, the bond length and energy strength compete with the electronic molecule-substrate interactions.

4.2.2 Halogen bond driven self-assembly of DBTP and DITP precursors

When deposited onto Ag(100) maintained at $T = 78$K, DITP form self-assembled islands stabilized by halogen bonds, which indicates that at this temperature molecular diffusion is high enough to allow rearrangement on the surface. Self-assembly does not take place spontaneously, but is induced by the bias voltage while scanning with a threshold bias at 300mV. Fig 4.6 (a) displays an STM image of a $[100 \times 100]$nm^2 area, where a square molecular reconstruction is extended over the whole terrace with some disordered area along the step edges. Noisy areas corresponding to locations where the molecules are still not ordered and are still diffusing during the scan are also visible in the top right corner of the image. The transition between ordered and noisy areas is fuzzy and the structural ordering was found to appear during scanning. The ordering process was improved over scanning and self-healing defects evolving with time and scanning were found. In fig. 4.6 (b), such a defective zone is shown, where molecules are dispersed and disordered. Other defects present an alternative structure with parallel aligned molecules as shown in fig. 4.6 (c). When keeping scanning with $V_{bias} > 300$mV, the square molecular reconstruction ordering was recovered. Once created the molecular structural arrangement is characterized by a certain stability, since it remains the same, even when the scanning bias is lowered under the threshold. In fig. 4.6 (d) and fig. 4.6 (e), the same scan area is shown for a scanning bias of 1.2V and of 30mV, respectively. On the terrace located in the middle and at the bottom part the square arrangement was lost at low bias, while it remains on the other terraces.

In order to elucidate the phenomenon at the origin of this induced molecular arrangement, a series of scans were conducted on non-ordered areas (diffusing molecules) at various tip-sample distances by changing approaching the tip by $\Delta Z = -1$nm from
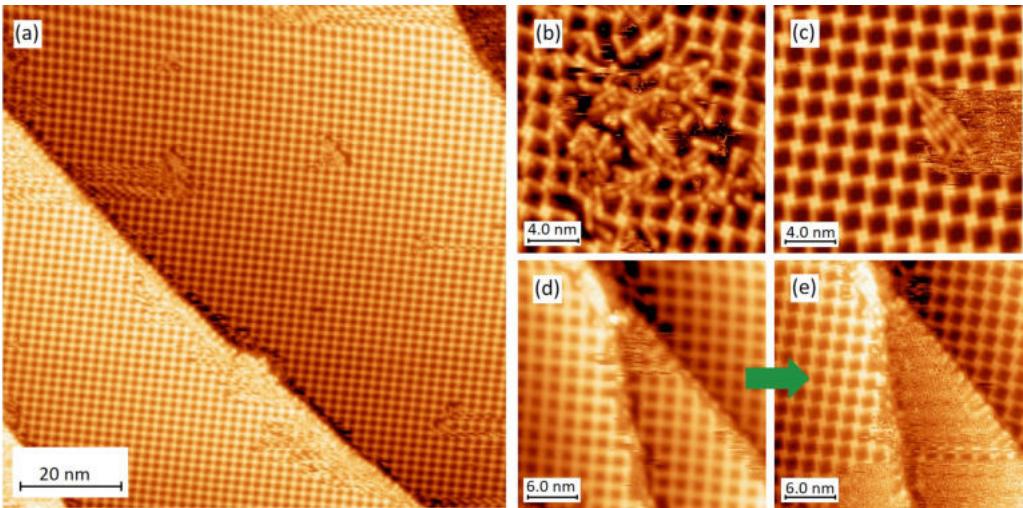
Figure 4.6 Constant current STM images of DITP precursors deposited at $T = 78$K on Ag(100): (a) Square molecular arrangement induced by scanning at 300mV; imaging conditions: 300mV, 3pA; (b) defective area, self-healing is obtained by keeping scanning the same area at a bias > 300mV; imaging conditions: 30mV, 10pA; (c) square and brick-wall arrangements; imaging conditions: 30mV, 5pA; (d and e): Differences in molecular arrangement by changing the scanning bias voltage from 1.2V to 30V, respectively. Imaging setpoint: 1pA (d) and 5pA (e).

a setpoint settled at 10pA, 300mV in order to check for electric field effects. No any order was induced by proceeding in such a way, excluding readily electric field effect of the molecular ordering. In contrast, another study on terarylene molecules on Cu(111) reports on tip-induced formation of a supramolecular network, where the $2D$ assembly stabilized by π-π stacking and van der Waals interactions was observed [136]. The main difference between the two systems DIPT/Ag(100) and terarylene/Cu(111) is that the dipole of the latter was found to be aligned with the vertical electric field induced by tip pulses while in our case, the dipole would be lying rather parallel to the surface. Therefore, for our system, the ordering is induced by a threshold bias at 300mV which might be related to a resonance of an electronic state located at the bromine atoms.

This molecular self-assembly was further examined by recording high resolution STM images as shown in fig. 4.7. The $2D$ assembly could be described as a windmill pattern with 4 molecules having their iodine atoms facing each other with an angle close to 90° (fig. 4.7 (a)). The 4 iodine atoms at the windmill center are found always in a clockwise manner offering for all nodes the same chirality on a same terrace, but this clockwise windmill was found to be anticlockwise on other terraces. As depicted in the schematic representation in fig. 4.7 (c), the 4 halogen bonds between neighbouring molecules (marked with red line) present a type II halogen contact. Therefore, a positive charge depletion zone at the end of one molecule is pointing towards the negative charged region of the other iodine atom. In addition, the molecular assembly is further stabilized by 4 H-I bonds between the iodine atom of one molecule and the hydrogen atom of the neighbour (marked with blue line). The bonding distance was found to be 0.45nm for I-I bonds and 0.36nm for I-H bonds, which is rather long compared with DFT calculations expected length [137] and also with reported experimental values of halogen bonds on different surfaces [138], [139].
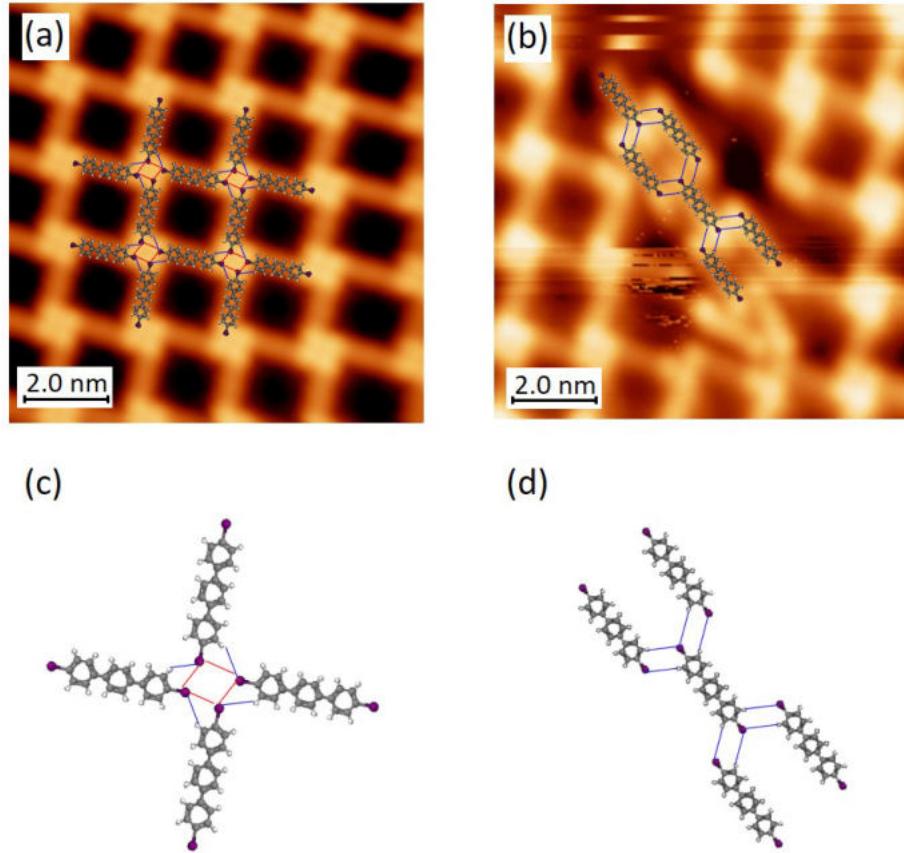
Figure 4.7 Constant current high resolution STM images of DITP precursors deposited at $T = 78K$ on Ag(100): (a) windmill square ordering; imaging conditions: 500mV, 15pA; (b) brick-wall ordering; imaging conditions: 300mV, 3pA; (c) schematic representation of the windmill arrangement and (d) schematic representation of the brick-wall arrangement.

The underlying substrate might have an influence and could weaken the halogen bonds due to either geometrical strains or by changing the electronic charge distribution within the molecules and could therefore be the origin of the deviation between measured and calculated values depending also on the substrate type. Further, the optimal I-I and H-I distance and bond angle with respect to the molecular axis might be the result of competition between I-I and I-H bonds. Chung *et al.* reported a similar phenomenon for Br-Br and Br-H bonds, where Br-H bond angle was shown to increase from the molecular axis while Br-Br bonds are more stable when in parallel [138]. A closer analysis of the high resolution STM images indeed reveals that the halogen bond is not exactly in the prolongation of the molecular axis, but their angle deviates slightly from 90°. The second (minority) arrangement observed was a brick-wall structure with higher packing density than the square arrangement (fig.4.7 (b) and (d)), also reported for 4,4"-dibromo-p-quaterphenyl (DBQP) on Au(111) at higher coverage [140].

For the sake of comparison, the same experiment was conducted on Ag(111) maintained at $T = 78K$. In this case, a threshold bias of 1.2V was required to induce a similar windmill ordering with alternating left and right handedness of the windmill centers leading to rectangular cells, but it was found to disappear by lowering the scanning bias.

Therefore, we might conclude that the substrate plays an important role in the stabilization of the self-assembly driven by halogen bonds. In the case of DBTP on Ag(100), the same results were found, but a mixture of left and right handedness of the windmill centers on the same area was observed on DBTP self-assembly leading to square, rectangular and trapezoidal cells as presented in fig. 4.8.
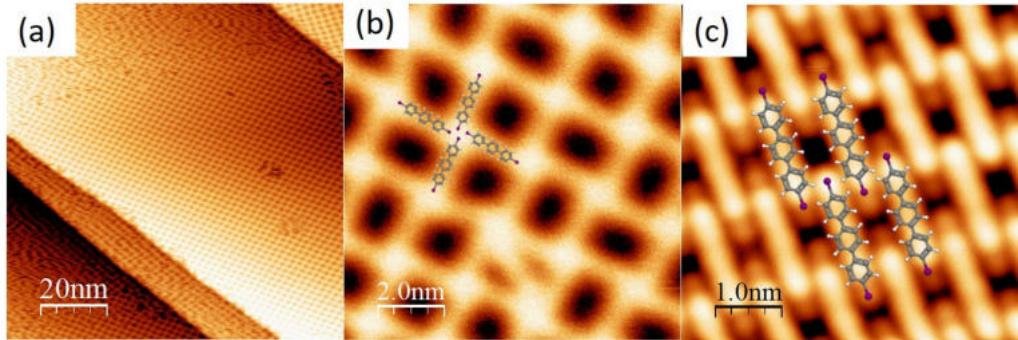

Figure 4.8 Constant current STM images of DBTP precursors deposited on Ag(100) maintained at $T = 77$K (a) tip-induced self-assembly monolayer of DBTP on Ag(100) (imaging conditions: 1pA, 300mV); (b) Zoom in the same area revealing halogen bonding with windmill of different chirality (imaging conditions: 1pA, 300mV); (c) brick-wall arrangement obtained by increasing the surface coverage. (imaging conditions: 10pA, 100mV).

The three coexisting cells found in the windmill ordering are depicted in fig. 4.9. The stability of the molecular layer arrangement with respect to the tip bias was found to be much stronger for DITP compared to DBTP allowing scanning at lower bias without losing the structural order. These results are in good agreement with previous halogen bonding studies that have proven that the strength of the interaction is related with the increasing polarizability of the halogen (I>Br) and with decreasing electronegativity [135]. By increasing the surface coverage, the brick-wall ordering was found to become more favorable.
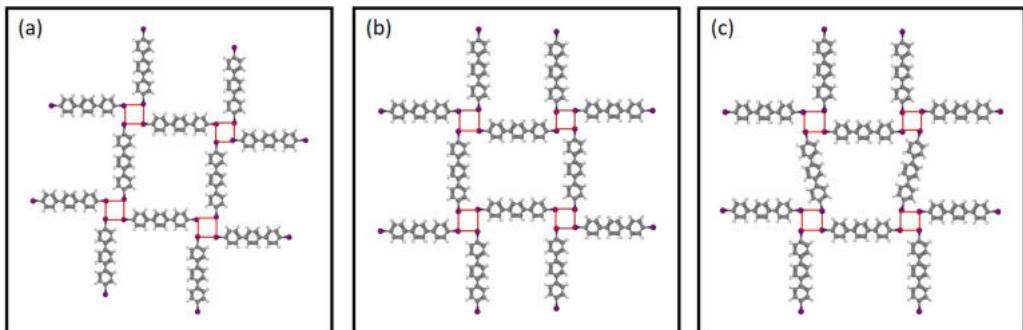
Figure 4.9 Schematic representation of (a) the square, (b) rectangular and (c) trapezoidal windmill arrangement found for DBTP/Ag(100). (color code for molecules as used in § 2.2.2: in grey C, in white H and dark red Br, halogen bonds are depicted in red)

The molecules were then exposed to UV light from a Xe arc discharge lamp though a fused silica UHV window offering a high transmittance to UV. In order to maintain the substrate at $T = 77$K, the sample was kept in the microscope. No changes were ob-

served after serval hours of UV exposition. By comparison with the study carried out on 4-bromo-4'-hydroxybiphenyl on Ag(111), where large scale $2D$ molecular arrays of surface biradicals were found after 266nm UV laser irradiation at $T = 80$K for 10min [141], we concluded that, in the configuration, only a small fraction of the UV light (or even no UV light) was reaching the sample in the microscope rending the process inefficient.

4.3 From organometallic intermediate to polymer

One of the simplest polymers that could be obtained through surface mediated synthesis is the poly-*para*-phenylene (PPP), which could be considered as the narrowest graphene nanoribbon (GNR). It has been considered for long as an organic semiconductor prototype of conjugated polymers. Numerous approaches in wet chemistry were reported to synthesize this polymer. The chemical route to access the long-desired polymer in its pristine form was established only in 2016 [142]. In neutral form PPP is insulator, that can be doped to increase its conductivity. Its mechanical properties, low density and high stability regarding temperature, oxygen exposure and moisture make PPP a promising candidate for organic electronics [143].
Using Ullmann coupling in UHV directly on metallic surfaces, PPP has been achieved starting from various different precursors such as 1,4-diiodobenzene [144], diiodo-biphenyl and dibromo-diphenyl [39], 4,4"-dibromo-p-terphenyl [145] [140] [146] and 4,4'-dibromo-p-quaterphenyl [140]. In addition, wider nanoribbons were also on-surface synthesized from PPP by dehydrogenation and C-C coupling [147]. Belonging to the same family class, hyperbenzene and zigzag poly-m-phenylene were also successfully achieved with halogen functionalized *m*-terphenyl precursors [148] [149] [150].

The results presented here were obtained for both DITP and DBTP precursors. They were deposited on the Ag(100) surface maintained at 300K. The main differences will be discussed in section 4.3.2.

4.3.1 Ullmann reaction using DBTP and DITP as precursors

Fig. 4.10 illustrates the different stages of Ullmann coupling taking place on the Ag(100) surface. At room temperature (300K) the C-Br bonds remain intact yielding the same windmill ordering induced by tip bias as observed for the $T = 78$K deposition. UV light exposition at 300K or annealing at 340K provokes debromination and radicals with unsaturated C-bonds are created, which form an organometallic intermediate (OGM) by picking up adatoms from the substrate as shown in the STM overview presented in fig. 4.10 (a). The Ag atoms involved in these OGM wires are either adatoms diffusing from low coordinated step edge sites, or atoms from the substrate lattice. The chains thus formed by alternating terphenyl groups $(PH)_3$ and Ag are aligned along the [100] and [010] main crystallographic directions of the substrate, but some misalignments along the chains are observed provoking fluctuations along the main direction as could be seen in fig. 4.10 (b). When integrated in the OGM structure, the bridging Ag atoms are positively charged, in contrast with the halogen atoms which are negatively charged from charge transfer with

the substrate. Therefore, along the OGM wires, the Ag atoms are very often surrounded by these negatively charged halogen atoms, which can be nevertheless found also at other locations along the chains. The next stage of the on-surface Ullmann reaction consists in eliminating the bridging silvers giving rise to short oligomers. This stage is illustrated in the high resolution STM image displayed in fig. 4.10 (c), where some $(PH)_6$ oligomers resulting from the elimination of 1 silver atom are clearly identified. In the last stage the Ullmann coupling is complete, PPP wires separated by halogen atoms are achieved.
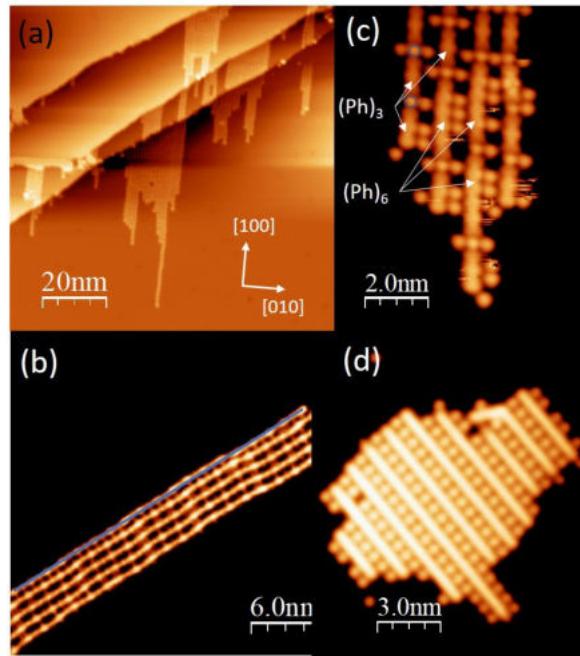
Figure 4.10   Constant current STM images of Ullmann coupling stages on Ag(100) (a) UV light activated precursors yielding the formation of OGM intermediate phase obtained at 300K (imaging conditions: 1pA, 500mV). (b) OGM wires along the [100] direction of the silver substrate presenting misalignment with a jump of half unit cell. (imaging conditions: 20pA, 100mV). (c) After annealing at 423K under exposition to UV light, some short oligomers start to be formed along the OGM wires by elimination of one bridging silver atom. (imaging conditions: 5pA, 30mV). (d) Completed Ullmann coupling obtained by annealing at 470K together with UV exposure displaying PPP wires intercalated with halogen atom rows.

In order to understand which are the parameters that govern the reaction and the effect of UV light exposition on the different stages of PPP formation, a detailed study with respect to experimental conditions i.e. annealing temperature and UV exposition and duration was carried out. The main results are summarized in table 4.1 below.

After UV exposition and annealing at 373K for 3 hours the same OGM structure was observed on the surface without noticeable change. Short oligomers $(PH)_6$ were obtained by UV-assisted annealing at 423K under elimination of one intercalated Ag atom in the OGM wires as depicted in fig. 4.10 (c) . Finally, the complete Ullmann coupling yielding PPP formation (fig. 4.10 (d)) was reached by UV-assisted annealing at 473K. The PPP wires were surrounded by halogen rows and were now aligned along the <110> direction. Annealing duration between 15min and 5 hours did not change the results on the oligomers formation.

	T	RT	373K	423K	473K	523K
(100)	UV	OGM	OGM	Oligomers + PPP	PPP	
	No UV	WM	OGM	OGM	Oligomers + PPP	PPP
(111)	UV	OGM	PPP			
	No UV	OGM	Oligomers	PPP		

Table 4.1 Synthetic view of the results obtained on Ag(100) and Ag(111) at different annealing temperatures with and without UV light exposition. WM stands for WindMill (halogen bonding driven self-assembly), OGM for organometallic intermediate and PPP refers to poly-para-phenylene i.e. completed C-C coupling. As can be seen directly from this table, the different reaction steps occurred at a temperature lowered by $T = 50K$, when a combination of UV light and temperature was used.
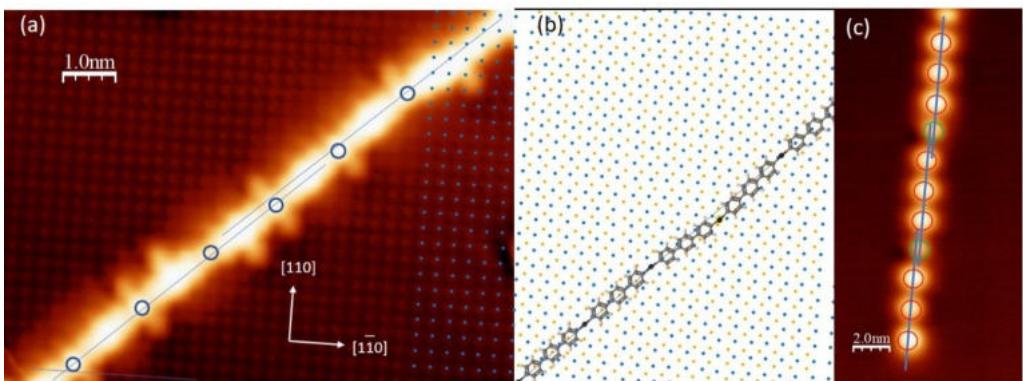
Figure 4.11 (a) Constant current STM image of an OGM chain on Ag(100) with atomic resolution on Ag(100) allowing to locate precisely the Ag bridging atoms and the main crystallographic directions of the substrate. Br atoms are visible besides the bridging Ag atoms and the tilted $(PH)_3$ groups (imaging conditions: 10pA, 100mV). (b) Schematic representation of OGM wires along the [100] direction of the silver substrate presenting a tilted molecule explaining the misalignment of the chain with a jump of half unit cell. (c) Constant current STM images of OGM chain on Ag(100) recorded at 1.9V, where the tilted monomer appears with a different brightness revealing a change of the LUMO state associated with a different adsorption site and bonding. Imaging conditions: 1.9V, 3pA.

More details on the OGM chains could be extracted from fig. 4.11 (a) where atomic resolution was achieved on the silver substrate. The OGM is oriented along the <100> or along the perpendicular <010> direction. DFT calculations conducted at CEMES by H. Tang confirmed in these directions a higher stability of the chain than in the <110> direction with a gain of 0.228eV. In gas phase, the Ag-Ag distance for a relaxed molecule without considering the substrate was found to be d(Ag-Ag) = 1.564nm. Experimentally, a statistical analysis of Ag-Ag distances gave a distance d(Ag-Ag) = 1.596nm proving an adaptation of the monomer to fit with the substrate lattice through stretching the C-Ag bonds. On Cu(111) this distance was reported to be 1.62nm [145], which demonstrates the strong substrate influence on the adsorption geometry. The energetically most stable locations of the Ag bridging atoms are the 4-fold hollow sites at the center of the silver reduced unit cell. In the OGM chain they occupy approximately every forth position with a distance of $4 \times a = 4 \times 0.408$nm $= 1.632$nm. Every forth monomer is therefore tilted in order to compensate the remaining mismatch of 0.036nm between the stretched molec-

ular length and the lattice parameters of the substrate (fig. 4.11 (b)). In long chains it might necessarily result in dislocations or chain disruptions to reduce strain and to allow relocation of Ag atoms and $(PH)_3$. The distance between the blue lines drawn in fig. 4.11 (a) corresponds to half cell parameter $a/2 = 0.144$nm. The electronic environment of the tilted monomer is obviously different and affects directly its electronic state. Scanned at 1.9V bias voltage it appears darker than the well aligned one (fig. 4.11 (c)). On various other STM scans this tilt occurs every 3 or 4 chain segments with a step size corresponding mostly to $a/2$, but multiples of $a/2$ are also found. Other studies conducted on similar precursors report a bending of the outer phenyl rings towards the Ag surface caused by the C-Ag-C bonds [151] [152].

Various annealing steps at 423K, 473K and 523K were then realized in order to turn the OGM into PPP. By using the combination of UV light and temperature the first PPP islands were observed after annealing at 423K together with oligomers as presented in fig. 4.12. Without UV light assistance PPP islands start to appear after annealing at 473K.
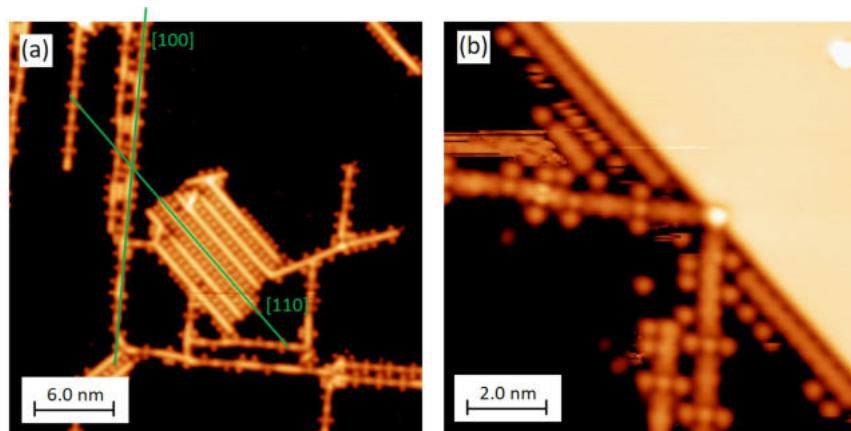
Figure 4.12   Constant current STM images of (a) OGM chains on Ag(100) with the appearance of a PPP island rotated by 45° with respect to the OGM chains after annealing at 473K without UV exposition, (b) partial polymerized OGM chain with PPP chains on the step edge after UV exposition and annealing at 423K; imaging conditions: (a) 10pA, 300mV, (b) 5pA, 30mV.

To find only PPP islands, the temperature of annealing has to rise up to 473K with UV light and up to 523K without light. We can conclude that the use of UV in our case allows to lower the reaction temperature by 50K. While the duration of annealing does not influence the result, we noticed that light induced processes were rather slow and long exposition times were needed to achieve PPP about 5 hours, which is partly due to the experimental setup since at the exit of the optical fiber (see chapter 2.3.1.4 Experimental Setup), the intensity drops at least by a factor 10.

In order to gain a better understanding on this model system, the same studies were carried out using DITP as precursors as well as on Ag(111) surface.

4.3.2 Main Differences between DBTP and DITP as precursors

While the C-Br bonds remain intact, the C-I bonds dissociate at a temperature between 78K and RT. Upon deposition on Ag(100) maintained at 300K, spontaneous creation of an OGM intermediate was observed with the same orientation as the OGM arising from DBTP precursors (fig. 4.13).
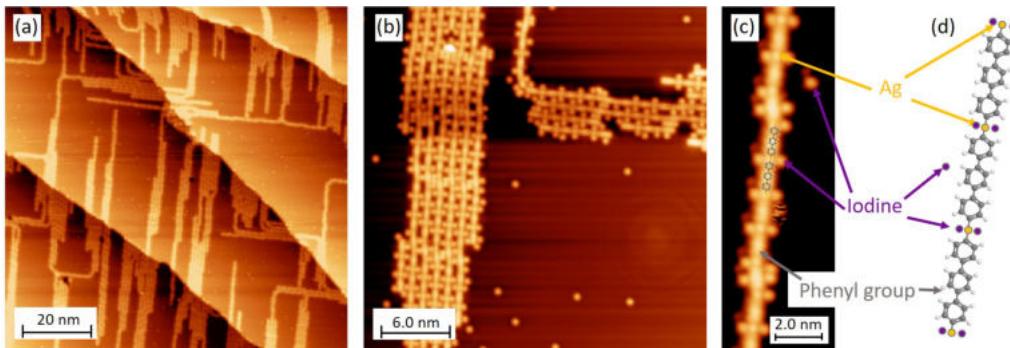

Figure 4.13 Constant current STM images of (a) an overview of the Ag(100) surface after deposition of the DITP at 300K; imaging conditions: 2pA, 500mV (b) Closest view of bunches of OGM wires; imaging conditions: 10pA, 30mV, (c) High resolution STM image of an OGM wire presenting tilted monomers along the wire; imaging conditions: 10pA, 30mV. (d) schematic representation of the OGM, color code: Ag bridging atoms are in yellow, iodine in violet, carbon in grey and hydrogen in white.

In summary, the same stages i.e. OGM, oligomers and PPP formation were observed for the Ullmann coupling starting with DITP precursors, unless the spontaneous dissociation of the C-I bonds at room temperature. Nevertheless, we pointed out a surprising result on the Ag-Ag distances in the OGM wires obtained with DITP. The statistical analysis provides a distance between two Ag bridging atoms of 1.63nm $\pm$ 0.06nm, which is larger than the mean distance obtained on the OGM wires from DBTP. We did not find any reasonable explanation to address this point, unless the nature of the halogen in the process might play a specific role in the reaction. Giovannantonio et al. in their study with diiodo-benzene (DIB) and dibromobenzene (DBB) on a Cu(110) surface [153] have pointed out that the choice of the halogen substituent influenced the ordering process leading to small islands when using DIB, while the OGM phase was found to cover the entire surface using DBB. The unit cells of the resulting structures were also found different depending on the choice of halogen. Other groups have reported a stabilizing effect of Br atoms on the OGM structure on Cu(111) [149] and on Cu(110) [154] [103]. It might be interesting for further studies to investigate, if the presence of Br does have an influence on the molecule-substrate interactions by reducing or making stronger the C-Ag bonds compared with iodine. Another interesting point we would like to mention here, is that the distribution of Ag-Ag distances is narrower for the OGM wires obtained after UV light exposition than with simple temperature treatment. This point will be discussed in the conclusion.

4.3.3 Comparative study using Ag(111) as substrate

The Ag(111) is known to be more reactive than Ag(100). Therefore, as displayed in table 4.1, the reaction temperature stages were found to be lower than the ones on Ag(100) as expected. The interaction with the metal seems to be rather low, since the same square windmill arrangements of the intact molecules were found on this 3-fold symmetry substrate. As on Ag(100), the molecular self-ordering was induced by the tip bias and was not stable at low bias. The windmill centers present alternate right and left handedness as could be observed in fig. 4.14 (a). As mentioned previously, the stability of WM structures is ensured by the intermolecular halogen bonds as demonstrated by Chung *et al.* [138]. In contrast with the OGM wires obtained on Ag(100), the OGM are not any more aligned with the main crystallographic axes of the substrate, but rather form loops starting and ending at step edges (fig. 4.14 (b)). Another difference regards the location of the halogen atoms, which are not any more found around the Ag bridging atoms but besides the $(Ph)_3$ as could be seen in fig. 4.14 (c). The PPP were achieved at 373K using UV light assistance and at 423K without light (fig. 4.14 (d)).
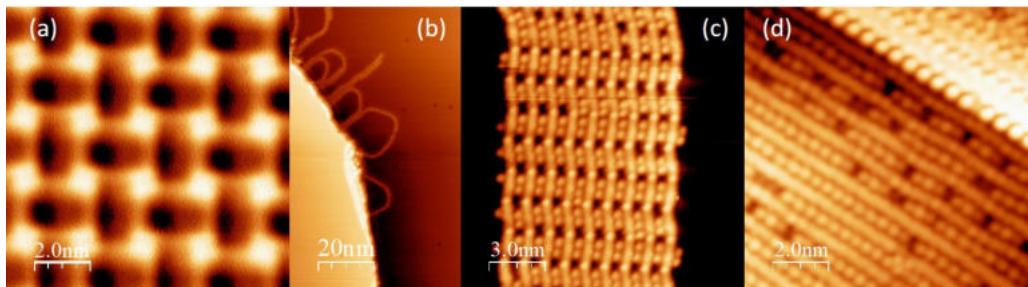
Figure 4.14 Constant current STM images of (a) alternating left and right handedness of the windmill structure after deposition of DITP on Ag(111) at 78K; imaging conditions: 2pA, 1.2V; (b) Close loop and straight OGM wires; imaging conditions: 1pA, 1.2V, (c) High resolution STM image of a bunch of OGM wires with tilted monomers, in this case the iodine are located besides the $(Ph)^3$ and not close to the Ag bridging atoms ; imaging conditions: 5pA, 300mV. (d) long PPP wires separated by halogen rows; imaging conditions: 5pA, 30mV

Here, the remarkable elements that could be pointed out are the drastic changes observed on the OGM wires as spontaneously formed by DITP deposition at 300K (fig. 4.14 (b)) after 3 hours UV irradiation at 300K, where parallel wires are observed. The location of the iodine ions seems to indicate that unlike on Ag(100) a charge redistribution over the $(Ph)_3$ has taken place letting the Ag bridging atoms rather neutral. The Ag-Ag distances were measured and the length distribution presents a maximum at $d(Ag - Ag) = 1.61 \pm 0.04$nm, similar to the value found on the Ag(001) surface with the same precursors indicating a stretched C-Ag bond and a strong interaction with the substrate. Finally, we would like to underline that the structureless PPP wires observed on Ag(100) in fig. 4.10 (d) present now some modulation along the polymer axis.

4.3.4 DFT calculations

In order to better understand the energy barriers at play in this process, DFT calculations were carried out at CEMES by Hao Tang [1] (see footnote).

The diffusion barrier calculated by using the CI-NEB method shows a relatively small value of 0.172eV and 0.171eV for DITP and DBTP molecules respectively. These values explain the free diffusion of these molecules even at the relatively low temperature of 77K. The spontaneous deiodination of DITP when the substrate was kept at RT could be explained by the low activation barrier in two steps (0.21eV to detach a first I atom and 0.39eV to detach the second I atom). The debromination follows also a two-step process. The energy to overcome the barrier to detach the first bromine atom from the DBTP molecule adsorbed along the <100> direction was estimated to 0.59eV. The detachment of the second Br atom requires a higher energy of 0.73eV (fig. 4.15). To provide enough energy to overcome these debromination barriers an annealing of the substrate at 373K was necessary. The detached bromine atoms diffuse easily as their diffusion barrier was estimated to 0.1eV.

Remaining at this temperature the thus formed para-terphenyl diradical prefers to coordinate spontaneously with diffusive Ag adatoms by forming OGM Ag-(Ph)$_3$-Ag, thanks to the low coordination barriers of 0.36eV to attach the first Ag atom and 0.39eV to attach the second Ag atom. In addition, the diffusion barrier of Ag adatoms is estimated to be about 0.3eV, which favours the approach of these atoms to the reactive terphenyl diradicals. The formation of OGM is an exothermic reaction releasing 1.05eV. The thus formed OGM complex adsorbed along the <100> direction has a length of 1.5961nm, which is 4% shorter than the distance between surface cells (1.6648nm). This length mismatch is at the origin of the misalignment detailed in fig. 4.11. Furthermore, the adsorption energy of OGM is −6.311eV along the <100>, while it is −6.083eV along the <110> direction. This difference in adsorption energy could be the reason why only OGM along <100> (or <010>) are observed.

---

[1] The density functional theory (DFT) calculations were performed by using the Vienna Ab-initio Simulation Package (VASP). The projector augmented wave (PAW) potentials in a plane wave basis were used to describe the valence electron ion core interaction of each element. The exchange-correlation energy corresponds to that given by the Perdew-Beck-Eneker (PBE) functional within the generalized gradient approximation (GGA). The van der Waals (vdW) was corrected by a modified version of the semi-empirical DFT-D2 method proposed by Grimme [155]. In this version the correction was not considered for metal-metal interactions within surface slab. The kinetic energy cut-off was fixed to 440eV, which gives a lattice parameter of 4.162Å for the optimized fcc bulk silver (with a reciprocal lattice mesh of $15 \times 15 \times 15$ to sample the $3D$ Brillouin zone). The self-consistent electronic convergence criterion was set to 10^{-6}eV and the geometrical relaxation was considered to be converged, when the forces on each unfixed atom was lower than 0.02eV/Å. The slab which represent the surface of Ag(001) was constructed by a 4 atomic plans with each plan contains of 48 Ag atoms (with a lateral dimension of 16.65×24.97Å^2), with x axis along the (100) direction and y axis along the (010) direction. The Brillouin zone was sampled with only the gamma point in the reciprocal space for preliminary calculations and a $3 \times 3 \times 3$ k-point sampling for the electronic structure analysis. The vacuum space was set to 18.32Å (about 12Å from the Ag surface). The dipole correction was considered in the z direction to compensate the interface dipole effect during the energy minimization. The activation barriers to detach iodine or bromine atom from the DITP and DBTP precursors, and that to detach Ag atoms from the organometallic complexes were estimated with the transition stats obtained by using the Climbing Image Nudged Elastic Band (CI-NEB) method as implemented by the Henkelman group [156] (at UT Austin). With this method the minimum energy reaction path was identified by optimizing the forces perpendicular to this path to be lower than 0.5eV/Å on each of equally separated intermediate images.
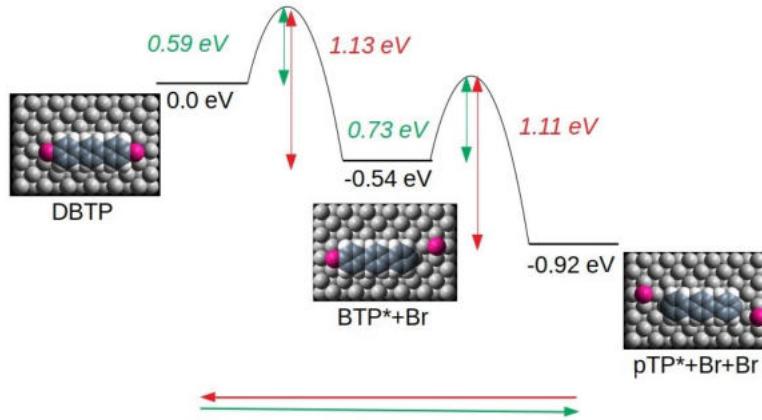
Figure 4.15 Energy barriers to overcome in order to detach (green arrow) and to attach (red arrow) the first and the second bromine atoms from/to the DBTP precursors calculated by CI-NEB.

Starting from already formed OGM structure, the C-C coupling also requires the formation of para-terphenyl diradicals. Fig. 4.16 shows the CI-NEB calculations of the activation barrier to cleave the Ag-C coordination bond, which is much higher (respectively 0.97eV and 0.83eV to detach the first and second Ag atom) than the energy necessary to attach Ag adatoms to this diradical (0.39eV and 0.36eV).
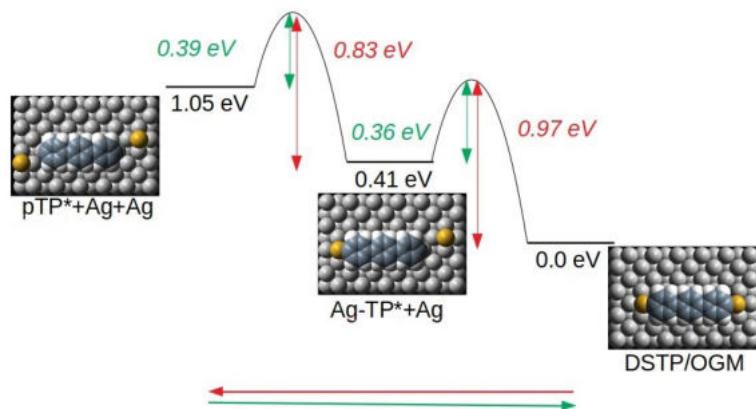
Figure 4.16 Energy barriers to overcome in order to detach (red arrow) and to attach (green arrow) the first and the second Ag bridging atoms from/to the OGM calculated by CI-NEB.

This higher activation energy could be the reason why an annealing temperature as high as 473K was reported for the last reaction step. However, a question could be raised here, which is why there is no direct formation of PPP through C-C coupling immediately after the p-terphenyl diradical formation. To answer this, we have calculated the diffusion barrier of the terphenyl diradical to be about 1.98eV. Thus, the direct C-C coupling when diradicals are lying parallel along the <100> direction is strongly diffusion limited. This conclusion is in contradiction to the case of benzene radicals coupling on Ag(111) and Au(111), which was calculated by Borjk *et al.*[157]

Finally, the co-existence of OGM and PPP could be explained by the competition between C-C covalent bond formation and C-Ag bond formation among the remaining pTP diradical, which might form either PPP or OGM complexes. That is why it was necessary to keep the substrate at a temperature as high as 473K, to ensure 100% of the pTP diradicals to form pure C-C bonds.

4.3.5 Decoupling MgO ultrathin films

The objective of this work was to synthesize these $1D$ wires onto MgO insulating layers. Therefore, the same experiment was realized on MgO islands grown on a Ag(100) surface. Large and flat MgO islands covering at least 50% of the metal (fig. 4.17 (a)) were deposited according to the growth parameters determined in § 3. Afterwards, DBTP precursors were deposited on the substrate maintained at low temperature to avoid diffusion and subsequently annealing at 300K with UV-light was performed for 11 hours. OGM wires were observed only on the uncovered metallic part of the substrate while all bromine atoms were found on the MgO islands (fig. 4.17 (b)). Without the Br atoms along, the OGM still follow mainly the <100> and <010> directions of the Ag(100) surface but no as strictly as reported before highlighting the stabilizing role of the Br.
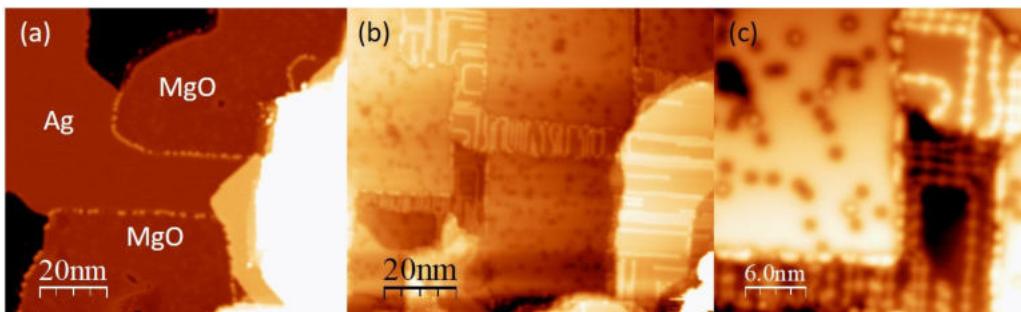
Figure 4.17 Constant current STM images of (a) the clean substrate with large and flat MgO islands and uncovered metallic parts; imaging conditions: −800mV, 1pA. (b) OGM wires almost saturate the metallic silver avoiding MgO island, onto which all bromine atoms are located; imaging conditions: 500mV, 1pA. (c) Zoom-in showing the OGM wires with fluctuating directions and Br adsorbed on an MgO island; imaging conditions: 1.2V, 3pA.

A second DBTP deposition was then realized at low temperature in order to saturate the metallic part to force the precursors to deposit onto the insulating islands. Direct observation was intended and some molecules were found on the MgO but images were hardly recorded due to their high diffusion coefficient even at 5K. Subsequent annealing at 300K with UV light was then performed for 12 hours. The first striking result which was found is that even by doubling the deposition time, the density of OGM did not increase (fig. 4.18 (a)). Nevertheless, a closer look into the MgO islands reveals that some other species a bit larger than Br were found among the Br atoms (fig. 4.18 (b)). In fact, they were already present after the first deposition as white dots surrounded by a characteristic ring denoting charged species. They could be assigned to p-TP unreacted diradicals trapped on the MgO surface, but no PPP was directly formed onto the insulating surface.

Attempts to manipulate the OGM and PPP formed on the metal surface to drag them through a "door" in between the surrounding atoms of the MgO islands were realized without success, which confirmed the high adsorption energy of OGM and PPP on Ag(100). PPP could be picked up by the tip, but further re-deposition onto MgO was unsuccessful.
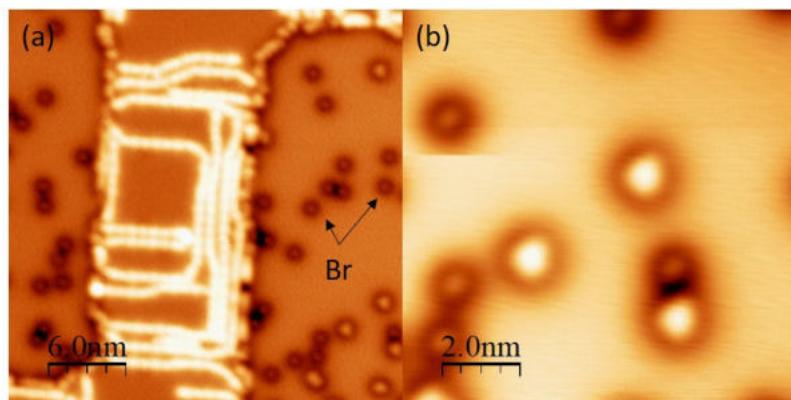

Figure 4.18 Constant current STM images recorded after the second DBTP deposition and subsequent annealing of (a) OGM onto metallic part and MgO islands; imaging conditions: 500mV, 1pA. (b) Br atoms and other species appearing as white dots surrounded by a ring, tentatively assigned to pTP diradicals; imaging conditions: 500mV, 15pA.

4.4 UV light effect on Ullmann reaction

From these studies, a number of conclusions can be drawn. Using UV light in combination with annealing temperature permits cleavage of the C-Br bond at 300K. Furthermore, the catalytic activity of the Ag(100) substrate is enhanced and becomes similar to that of Cu(111). A comparative table of Ullmann coupling reaction of the brominated precursors onto various substrates is shown in table 4.2.

Precursors	Substrate	OGM	Oligomers	PPP
DBBP[39]	$Au111$	No	500K	No
DBT[158]	$Au111$	410K		
DBTP^a	$Ag100$	RT+UV	423K+UV	473K+UV
DBBP[39]	$Ag111$	RT	373K	473K
BHydroxyBP[141]	$Ag111$	-	-	80K ($\lambda = 266$nm)
DBTP[145]	$Cu111$	RT	393K	473K
DBBP[39]	$Cu111$	<RT	-	450K

Table 4.2 Comparative table of on-surface Ullmann reaction temperatures on different substrates. (^{a}) refers to this work. For the same DBTP precursors, the use of UV light enhances the catalytic activity of the Ag(100) to Cu(111) level.

The reaction temperature to achieve OGM, oligomers and PPP was lowered by 50K, which might be applied to other systems with larger or more fragile molecules that might not stand annealing at high temperatures. In addition, ordering was improved in the case of DBTP on Ag(111) due to UV light. In order to limit molecular desorption and fragmentation during the C-Br bond dissociation, previous studies have demonstrated that

this first activation step could be done by UV light exposition, for example in Basagni *et al.* [158] on 5,11-di-bromotetracene on Au(111). The comparison between thermal and light dissociation has shown that at 410K thermal process yields disordered area with rare zones where OGM dimers were observed, while a significant increase of surface order was obtained by using milder conditions (RT) together with 405nm light irradiation. Moreover, X-ray Photoemission Spectroscopy (XPS) analysis has revealed coverage decrease due to thermal treatment, while the disorder was assigned to molecular fragmentation. Another study carried out on 4-bromo-4' hydroxybiphenyl on Ag(111) has shown that upon radiation using a 266nm UV laser at 80K, debromination and dihydroxylation were achieved giving rise to covalently bonded polyphenylene polymer chains [141]. Other photoinduced reactions involving $C - X$ (X=Br, Cl) bond breaking have been also used as a direct route to form single or molecular bilayers on the $Si(111) - (7 \times 7)$ surface [159]. In all these studies, UV light effect was studied only on the first step of the Ullmann reaction regarding C-X bond cleavage. Here, we have used UV light combined with temperature at each stage of the reaction benefiting from milder conditions. This strategy allows as well to decouple the diffusion step (activated by temperature) from the bond cleavage.

The underlying mechanisms of photoinduced processes were presented in § 2.2.4 "Photochemistry on surfaces". From this step, a direct excitation of the adsorbate can be readily excluded and therefore, the effect of UV exposition is due to substrate mediated excitation. In particular, plasmon induced hot carrier generation and hot electron transfer in the adsorbates might be at play, since the catalytic activity of the substrate is clearly improved. On Ag(100), surface plasmon energy was reported at 3.69eV (corresponding to 336nm wavelength), which is indeed provided by the Xe lamp used in this study.

About the attempts to achieve direct Ullmann coupling on MgO by UV-light excitation, several limiting factors were identified, such as the very high diffusion coefficient of the DBTP and DITP precursors favoring their transfer towards the metallic uncovered part of the Ag(100) and the strong adsorption energy of the OGM and PPP on the metal preventing their manipulation towards the insulting islands.

5 On insulating-surface synthesis

In this chapter, I will present the resulting products obtained from two halogenated coordination complexes as precursors on Ag(100), Ag(111) and MgO surfaces. These complexes, synthesized at CEMES by Andrej Jancarik, are shown in fig. 5.1 (c). They were specially designed for on-surface synthesis from both salen (fig.5.1 (a)) and salophen (fig. 5.1 (b)) ligands in order to get a more rigid skeleton. Two brominated complexes were studied: one with Cu as central ion and the second one with Ni. The metallic species are linked by coordination bonds to 2 N and 2 O. They will be named in the following as Cu-salen type and Ni-salen type.
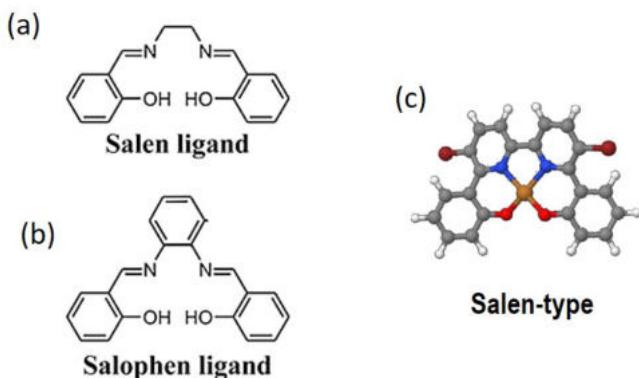
Figure 5.1   Schematic representation of (a) salen and (b) salophen ligands. (c) Structure of the brominated complexes studied in this work. Color code: dark red= Br, brown metal ion= Cu or Ni, blue= N, red= O, grey= C and white= H.

5.1 Salen and Salophen

Thanks to their high flexibility and versatility, salen (N,N-bis(salicylidene) ethylenediamine) and salophen (N,N-bis(salicylidene)phenylenediamine) ligands are extensively used in coordination chemistry to form complexes with metallic atoms giving rise to a wide range of magnetic and electronic properties [160]. A number of studies report on the catalytic activity of Co-salen complexes [161], [162], [163], such as films deposited by electrodeposition and measured by cyclic voltammetry and bulk electrolysis, demonstrating catalytic current regarding water oxidation to achieve water splitting [161]. Their potential to behave as building blocks for molecular self-assembly and supramolecular architectures has been oftentimes reported. Salen derived precursors have therefore been subject of numerous studies because a huge variety of substituents can be placed on their phenol rings and diamine bridge. They allow to adjust intermolecular distances and packaging geometry as also the stability and electronic properties in the self-assembled structures, ranging from

porous networks to close-packed nanoarchitectures. Carboxylic groups are used for the formation of stabilizing hydrogen bonds. The interplay between these structuring bonds, Van der Waals forces and dipole interactions governs the self-assembly. Substituent groups can be directly linked to the phenol, or be spaced using benzyl rings, thus tuning the length of the complex and the resulting chains. Generally, an advantage of metal–salen based complexes is their rather good molecule-surface coupling through their quasi plane structure, also found in porphyrins and phthalocyanines. Electrostatic interactions with the substrate cause the central ion to adsorb on specific adsorption sites and define the orientation of the adsorbed complexes versus the crystallographic directions. This selectivity can be further enhanced by introducing secondary binding sites or side groups, which cause steric hindering [164], [165].

STM images recorded at the solid–liquid interface on HOPG substrate (highly oriented pyrolytic graphite) of Ni^{II}–salen derivative complexes have shown that porous networks and close-packed nanoarchitectures can be engineered using these building blocks. These nanoarchitectures were found to be stabilized by hydrogen bonds, Van der Waals, and molecular dipolar interactions [165]. Up to date, only a few STM studies were reported on these complexes. One of the first carried out on chlorine functionalized Co-salen on Cu(111) has revealed the mechanism at play on the formation of self-assembly monolayer, stabilized by two competing effects, intermolecular attractive ionic forces, and repulsive forces along the hydrogen terminated sides [166]. Interestingly, Ni^{II}-salen complexes deposited on HOPG surface aggregate easily to single, segregated, homochiral polymeric chains. Weak intermolecular $Ni^{II}\cdots$OMe coordination bonds (d(MeO$-$Ni) = 0.35nm) were found to be responsible for the formation of these chiral, helical and $1D$ assemblies [167]. Salen ligands have attracted a special attention regarding single molecule magnets (SMM) since with d^8 metallic ions they form square planar low spin complexes. Wiesendanger's group at the Hamburg University has investigated the magnetic coupling between Co-salen complexes and various surfaces with different electronic and magnetic properties [168], [169].

Metallo salen and salophen complexes are potential compounds to be used in biochemistry. Their biological activity and rich photophysical properties transform them into interesting candidates for bioinorganic model compounds and enzymes mimics applied as therapeutics and biosensors (ref. 9 in [160]). It has been reported that several salen and salophen-based transition metal complexes may interact with or modify DNA. The ability to bind to DNA and DNA modifications can be controlled by the charge on the salen unit and by the selection of the central metal ion (ref. 38 in [160]) providing in this way new insight into the field of DNA nanotechnology [160].

5.2 Cu-salen type precursors

5.2.1 Single molecules

The Cu-salen type complexes were deposited on a Ag(100) surface at 5K in order to get insight into single molecules integrity, apparent size and electronic properties. Fig. 5.2 displays STM images of the complexes where different species were identified as intact brominated complex (fig. 5.2 (a)) presenting a C shape, and rotated ligand without metal ion (fig. 5.2 (b)) with a S shape. By bias pulses with STM tip it was possible to cleave the bromine at a bias voltage of 2.7V giving unambiguous prove for the C-shaped feature being an intact molecule. The debrominated molecule with the detached bromines lying nearby is shown in fig. 5.2 (c). In the following temperature dependent study another type of molecule appeared with a V shape. It could be assigned to a non-rotated ligand without the central metal ion. The corresponding model is shown in fig. 5.2 (d)). These first results are quite surprising since the not very high catalytic activity of the Ag(100) substrate is further reduced at 5K. The coordination bonds with Cu are known to be very labile. The fact to find intact molecules together with ligands and debrominated complexes might suggest that the fragmentation was not occurring in the crucible but rather when reaching the surface, or that the initial powder was contaminated with some unreacted ligands. From now on, we will refer to these species as C and S. In order to check the ratio between S and C species, the molecular coverage was increased by a second longer deposition at 5K.

5.2.2 Self-assembly

In order to evaluate the ratio of S and C molecules on the Ag(100) surface, a series of STM images were recorded at different annealing temperatures to promote self-assembly. The results are presented in fig. 5.3. After annealing at 300K for 15min coexisting disordered and ordered regions are visible. The disordered regions correspond to a mixture of S and C as well as V-shape. Long range ordered regions with more or less structural defects consisting in only S-shape molecules were found (fig. 5.3 (a-c)). Further annealing at 373K improves the ordering in the self-assembly, islands with residual disordered regions with only S and V molecules are present (no more the C-shape). Detailed analysis of the STM images reveals the presence of atoms between the S which might be bromines atoms (fig. 5.3 (d-f)). Upon annealing at 473K, the same oblique unit cell of S shapes with rotated domains over large regions and only S species were found (fig. 5.3 (g-i)). A final attempt to create organic chains by dehydrogenation was realized by annealing the sample at 523K. A more closely packed structure was then found consisting of S pairs, the bromine atoms are now found on the Ag(100) surface outside the self-assembly molecular islands, no long chains or dimers were formed.
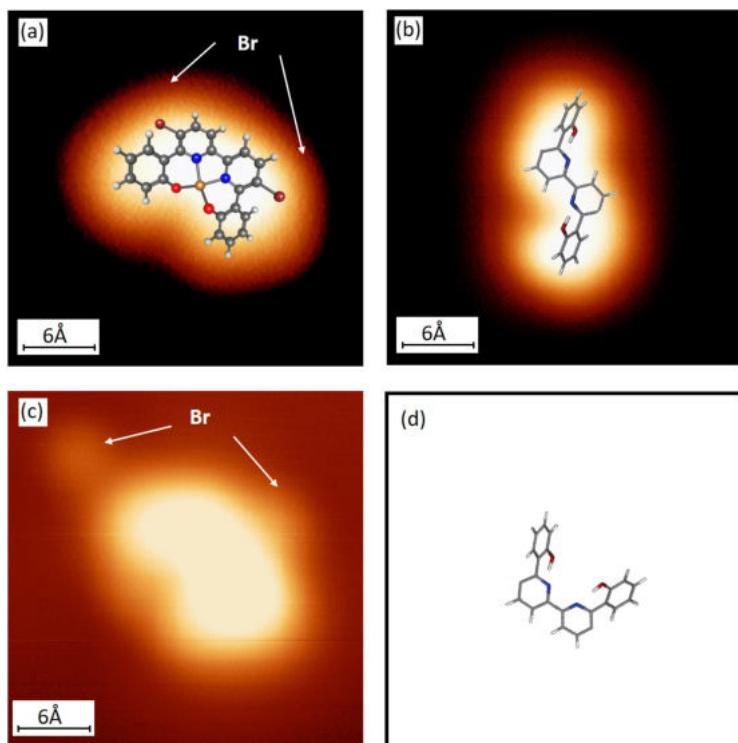
Figure 5.2 STM images recorded after deposition of the Cu-salen type complexes on Ag(100) maintained at 5K of (a) intact precursor; (b) rotated ligand; (c) debrominated precursor and (d) model of not rotated ligand. Imaging conditions: (a) −300mV, 1pA, (b) and (c) −300mV, 5pA.

The same study versus annealing temperature was conducted on Ag(111). Deposited on the Ag(111) surface the same mixture of the 3 species was found as on the Ag(100) surface. After deposition or annealing at RT they agglomerate. In zones where the 3 species are mixed they are disordered and no periodic structure is visible (fig. 5.4 (a) and (b)). However, the separated species were found to assemble into a regular pattern. Fig. 5.4 (c) shows the assembly of intact molecules with the molecular model superposed. The symmetry axes of the resulting lattice defined by the central Cu-atoms of the molecules enclose an angle of 50°, building an oblique unit cell with the dimensions $a = 1.56$nm in one and alternating $b_1 = 1.02$nm and $b_2 = 0.51$nm in the other direction. In the knowledge of the underlying hexagonal substrate lattice, this regular pattern motivated us to search for 50° angles in the hexagonal lattice. Fig. 5.4 (d) shows a correspondent model. There is an almost 50°-angle between the $[2, 1, 0]$ and the $[2, -1, 0]$ direction with the lattice parameters 0.25nm and 0.76nm respectively. The measured distances of 0.51nm and 1.02nm in the first and 1.56nm in the second direction would match these values very well ($2 \times /4\times$ and $2\times$). This registry with the substrate indicates its determining role in the assembly with molecules sitting on specific substrate sites. However, an essential result was that no Ullmann coupling reaction has taken place so far. Further, there were no bromine atoms seen on the substrate, normally well identifiable though their specific, bias voltage dependent appearance in the STM scan. They could be still attached to the molecule. In this case the activation energy of Ullmann coupling, the C-Br bond cleavage, would lie above the Cu-coordination bond energy making a coupling reaction between intact molecules impossible since Cu-coordination bonds would always break before activation of the coupling reaction.
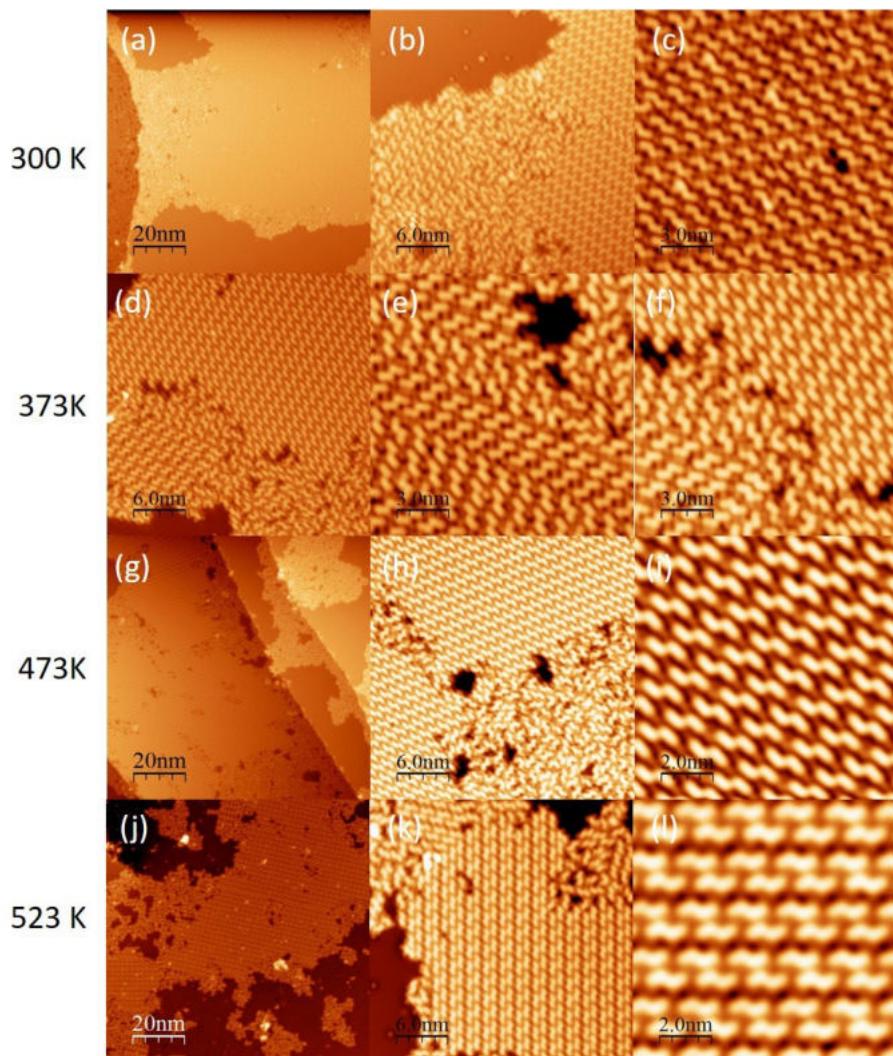
Figure 5.3 Constant current STM images recorded after each annealing temperature step. (a-c) After annealing at 300K, disordered regions coexisting with large self-assembled islands of S can be observed on the overview image (a). (d-f) After annealing at 373K, some V-shape molecule corresponding to the ligand without central metal atom are found in the disordered regions. Ordering is improved in the S-self-assembly islands, and the molecules are separated by atoms that could be assigned to bromines. (g-i) Upon annealing at 473K, only S species are found and square unit cell with 1 S and 1 Br per unit cell forms large ordered domains with disordered regions between rotated domains. (j-l) After the final annealing step at 523K, close-packed domains consisting of S-pairs were observed, in this latter arrangement, the bromines moved out to the Ag(100) surface. No dehydrogenated dimer neither polymer were formed even after annealing at 523K.
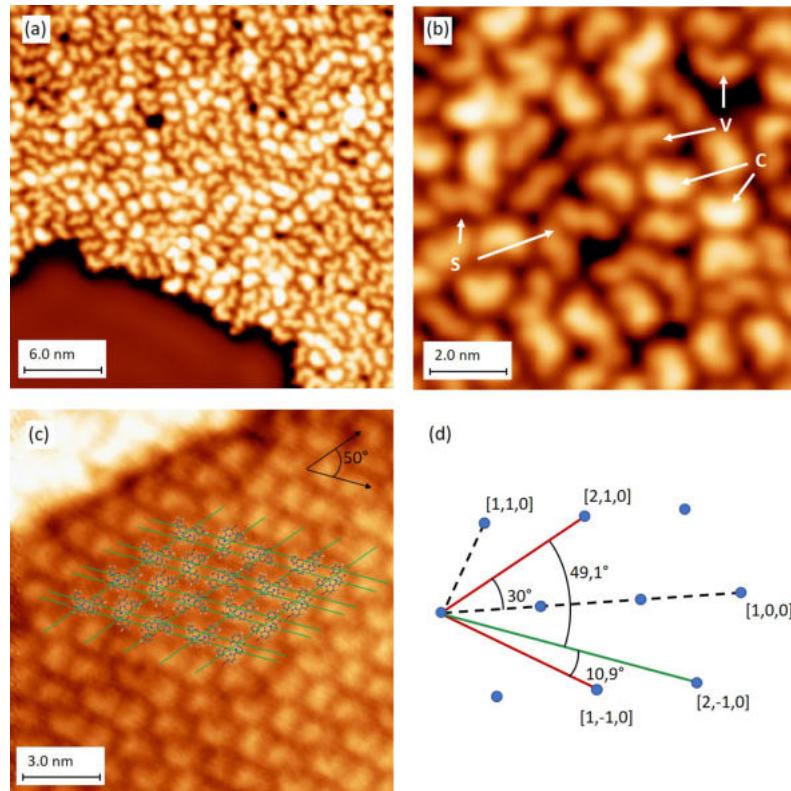
Figure 5.4 (a), (b) Cu-salentype deposited on Ag(111) at RT, mixture of C-shape features (intact molecules) and S and V shape (rotated and not rotated ligands without central Cu-atom), (c) regular assembly of intact molecules with superposed molecular model and symmetry axes,(d) schematic of hexagonal lattice,the $[2,1,0]$ and $[2,-1,0]$ directions enclosing the same angle as measured in reconstruction of (c), imaging conditions: (a) -300mV, 5pA, (b) 200mV, 5pA, (c) -600mV, 1pA

After annealing at 370K all molecules were broken. Mostly S-shape, but also V-shape species could be found on the surface organized in large sized self-assembled reconstructions. The cleaved bromine atoms are clearly seen in the STM scan, occupying specific positions in the self-assembled network. Here the different reconstructions are shortly described: fig. 5.5 (a), S-shaped molecules are ordered parallel. Bromine atoms are placed at each end of the S, indicated in the image as blue dots., fig. 5.5 (b), molecules are organised in groups of 3 S, the middle S is mirrored on the S long axis against the outer S. Groups are alternating oriented in two vertical directions. Bromine atoms are placed around each group, fig. 5.5 (c), similar groups of three S, but each group oriented in the same direction. There are several domain boundaries, therefore also groups of 2 S were found. Bromine atoms are placed between the groups, fig. 5.5 (d), reconstruction containing V-shape molecules, groups of two V turned back to back and spaced from each other by two atoms. The total number of additional atoms placed around the V was counted 3 per molecule. Besides the two bromine per molecule there might be an other additional atom like Ag or Cu.
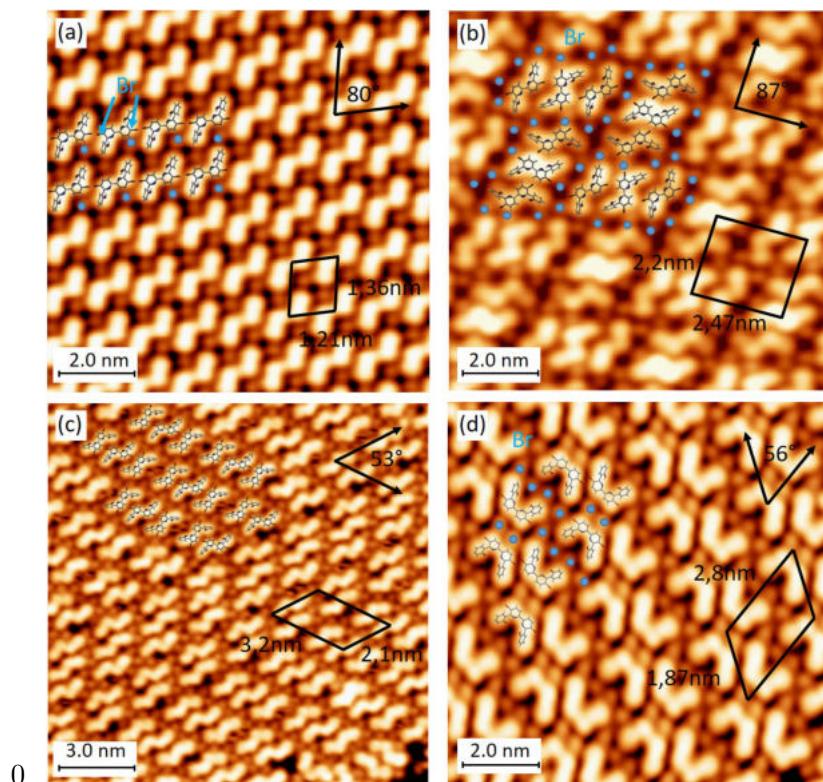
Figure 5.5 Cu-salentype molecules after annealing at 370K on Ag(111), (a)1st reconstruction: S parallel, (b)2nd reconsruction: groups of 3 S, alternating turned by 90°, (c) 3rd reconstruction: groups of 3 S, aligned parallel, (d)4th reconstruciton: groups of 2 V, spaced by 2 bromines from each other, superposed molecular model, bromine atoms represented as blue dots, unit cell size and angle as indicated, imaging conditions: (a) 70mV, 100pA, (b)−100mV, 30pA, (c) −300mV, 3pA, zoom, (d)−300mV, 3pA

In these very regular reconstructions we could not find any hexagonal symmetry, neither corresponding lattice parameters indicating that geometry of reconstructions is rather governed by intermolecular interactions than by substrate influences, though a substrate

effect is seen in the difference between the geometry of reconstructions on Ag(111) and Ag(001) (angles and distances). Even though bromine atoms apparently have been cleaved during annealing, no Ullmann coupling reaction has taken place. Unit cell size and angles of reconstructions are summarized in table 5.1.

	Nb of reconstr.	Type of molecule	Unit cell	dimensions	Angle between axes	Nb of molecules per unit cell	Space per molecule	Nb of addition. atoms/mol.
RT Ag(111)	1	intact	oblique	$a_1 = 0.51$nm $a_2 = 1.02$nm $b = 1.56$nm	50°	1	1nm^2	0
370K Ag(111)	2	S	oblique	$a = 1.21$nm $b = 1.36$nm	80°	1	1.6nm^2	2
	3	S	oblique	$a = 2.2$nm $b = 2.47$nm	87°	3	1.8nm^2	2
	4	S	oblique	$a = 3.2$nm $b = 2.1$nm	53°	3	1.8nm^2	2
	5	V	oblique	$a = 2.8$nm $b = 1.87$nm	56°	2	2.2nm^2	3
223K Ag(111)	$6 \simeq 3$	S	oblique	$a = 1.9$nm $b = 3.0$nm	66°	3	1.7nm^2	0
	7	C-dimer	oblique	$a = 2.4$nm $b = 1.6$nm	70°	1	3.6nm^2	0
470K Ag(111)	$8 \simeq 3$	S	oblique	$a = 1.9$nm $b = 3.0$nm	67°	3	1.7nm^2	0
530K Ag(111)	$9 \simeq 3$	S	oblique	$a = 2.0$nm $b = 3.2$nm	57°	3	2.1nm^2	0
	10	2S	Mix hexagonal + square	square: $a = 2.7$nm $b = 2.7$nm	square: 83°	square: 2	3.6nm^2	0
RT Ag(001)	11	S	oblique	$a = 2.1$nm $b = 1.35$nm	42°	1	1.9nm^2	0

Table 5.1 Listing of molecular reconstructions of Cu-Salentype on Ag(111).

Reconstructions present on the surface alter with annealing temperature. After annealing at 420K and higher there is mainly one of the reconstructions left, presented above in fig. 5.5 (c) (parallel aligned groups of three molecules). Another reconstruction type appeared, shown in fig. 5.6. It is surprising in several aspects. The molecular shape resembles more the C-shape than the V-shape, indicating the presence of a central atom. Further, in superposition of the molecular model over the image, findings let suggest the formation of dimers. This is at this stage of the reaction not apparent, since there were already found wide reconstructions with broken and debrominated molecules after annealing at 370K.

It could be possible that substrate Ag-atoms replaced the lost Cu-atoms, leading to C-shape species. This would need energy and therefore, in comparison with the other reconstructions found before, explain the higher annealing temperature needed to form this reconstruction. Fig. 5.7 (a) and (b) shows the molecule with front and side-view respectively (calculated model in gas form). It is not planar, but the arms are oriented in a deviating direction from the molecular plane. This $3D$ structure avoids steric hindering when molecules are approaching each other making it possible to perform the Ullmann coupling as illustrated in fig. 5.7 (c) and (d). The ligands without central Cu-atom have adapted another geometry illustrated in the models 5.7 (e) and (f) respectively. They are rather plane, but the outer phenyl ring with the unsaturated coordination bonds turned out
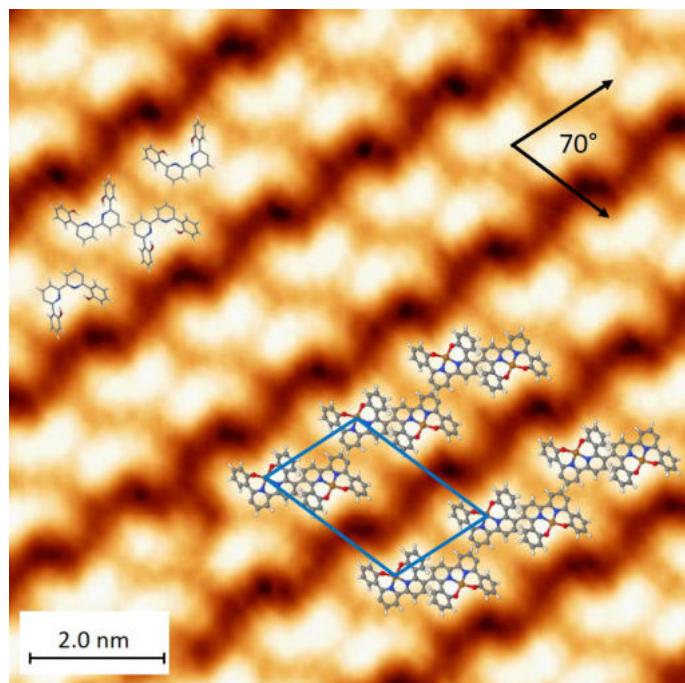
Figure 5.6 Cu-salen type after annealing at 420K*C*. Eventually reconstruction with dimers, molecular model and unit-cell are superposed. In the left upper corner is placed the model of V-shape molecule for comparison; imaging conditions: −200mV, 2pA, zoom

of plane. Adsorbed on the substrate they might interact with the surface atoms. Probably though steric hindering a further coupling reaction between several molecules might not be possible any more, the reason why after annealing at 370K no polymerized structures were observed . The situation changes, if the 3*D* structure is recovered by new coordination with a substrate Ag atom. This could be an explanation, why after an annealing at 420K finally dimers are created, but further examination would be necessary to confirm this assumption.
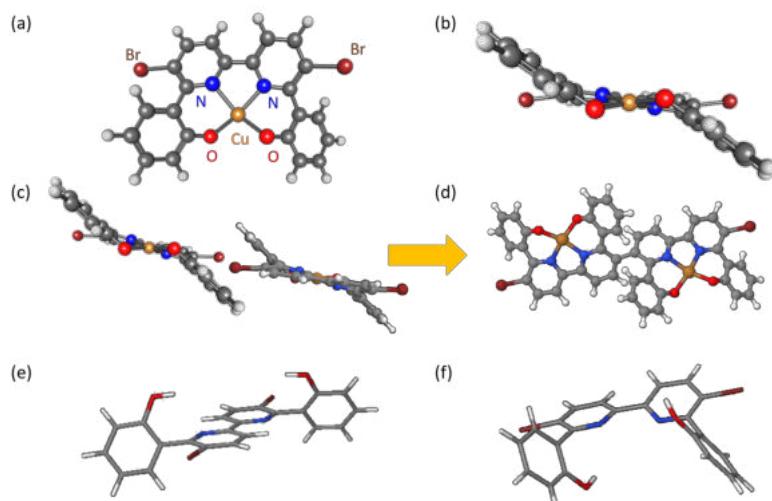
Figure 5.7 DFT calculated models (a)and (b) top view and side-view of intact Cu-salentype molecule, (c) side-view of two approached molecules, (d) dimer,(e) side-view of S, (f) side-view of V

Equally surprising was another reconstruction type, which appeared after annealing at 530K. It was built out of groups of two molecules, turned in 4 different orientations, resulting in both alternating square and hexagonal lattice ordered areas. The reconstruction is shown in fig. 5.8. In respect with the relatively high annealing temperature it could be possible that these "tandem" groups are related with through dehydrogenation polymerized species.
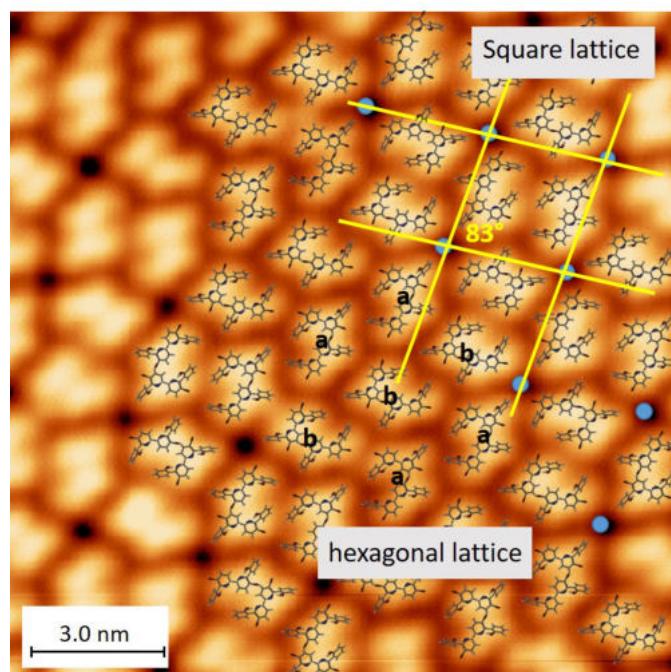
Figure 5.8 Cu-salentype molecules on Ag(111) after annealing at 530K, molecular models are superposed, groups of two molecules are forming either a hexagonal (abab stacking) or a square lattice

To conclude, in the presented study about Cu-salentype precursors the first activation process, meanly the dissociation of bromine atoms, was completed. Molecules had enough thermal mobility to diffuse over the surface, necessary requirement for mutual approaching and coupling. Unfortunately molecules have broken before the Ullmann reaction could take place. Upon annealing at 420K possibly dimers have been created with the help of new coordinated central atoms originating from the substrate. By restoring the $3D$-structure of molecules this might reduce the steric hindering enabling the Ullmann coupling. After annealing at 530K another species was found, which we assigned to the through dehydrogenation polymerized species. Certainly further investigations are necessary to confirm these assumptions. To overcome the difficulties encountered in this study, different strategies could be followed:

(1) A stronger bound central ion, as Co, Ni or Zn could be used, with the aim that decomposition takes place at higher temperature as the coupling reaction.

(2) With the same aim precursors with other halogen substituents, e.g. iodine, could be used, decreasing the activation temperature.

(3) At insulating surface decomposition might be prevented due tu lower substrate activity;

the problem that there is also less catalytic activity to excite the coupling reaction, could be solved using UV-light.

(4) Using UV-light would lower the reaction temperature and allow catalytic activity on insulating thin films.

(5) Finally, an inverse strategy could be followed, using molecules without central ion and metallizing them on the substrate, once the Ullmann coupling reaction has taken place. Therefore separate deposition on the substrate of molecular backbone and metal atoms would be necessary.

5.3 Ni-salen type precursors

In order to avoid the same fragmentation that was suffered by the Cu-salen type precursors on Ag(100) and Ag(111), a second precursor based on Ni metal core, synthesized at CEMES by Andrej Jancarik, was deposited onto MgO islands grown on Ag(100) offering an intermediate surface reactivity between metals and bulk insulators. During deposition the substrate was hold at 300K with subsequent annealing at 373K for 16 hours under UV-light exposition. As could be seen in fig. 5.9 (a), the MgO islands cover about 70% of the surface which increases the probability to find the precursors on top of it. As expected, they mainly decorate the most reactive species present on the surface i.e. on the atomic silver atoms surrounding the MgO island. Surprisingly, once these special adsorption sites were saturated, the rest of the Ni-precursors preferentially adsorb onto MgO rather than on the uncovered parts of the metal (fig. 5.9 (b)). High resolution STM image displayed in fig. 5.9 (c) shows a couple of precursors on the MgO surface.
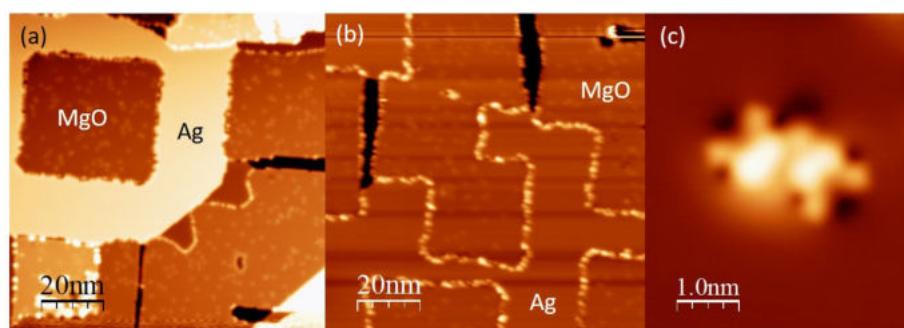
Figure 5.9 Constant current STM of (a) the MgO islands grown onto Ag(100) covering about 70% of the total surface. Imaging conditions 1V, 2pA. (b) Upon Ni-salen type deposition, a preferential adsorption site was found on the silver atoms surrounding the islands with some precursors adsorb on the MgO. Imaging conditions 300mV, 10pA. (c) Pair of Ni-salen type resting on MgO. Imaging conditions 100mV, 10pA.

I would like to emphasize 3 elements that are worth to be mentioned. First of all, unlike on NaCl on which molecules are so weakly adsorbed that the scanning tunneling current has to be set at values of 1pA or lower, here on MgO, it was possible to scan at relatively high tunneling current until 30pA without destroying the tip or the surface or both. Secondly, the shape of the molecule observed in fig. 5.9 (c) suggests that fragmentation did not occur confirming the stronger coordination bond for Ni than for Cu

and therefore the precursor presents the expected crescent shape. The preferential adsorption on MgO rather than on Ag(100), even after annealing at 373K, could be due to the formation of an extra bond between one O of the underlying MgO and the Ni ion at the center of the molecule. In solution, Ni^{II} (d^8 electronic shell configuration) rather adopt an octahedral environment occupying the center of a double pyramid attached by their basis and forming 6 bonds with the ligands. Here, the square planar configuration is imposed by the coordination bonds, but the compound might be stabilized on the surface by its apical bond. This hypothesis is further supported by the fact that the ligand without metal ion, i.e. only organic, would preferentially adsorb on the metallic areas. Attempts to interpret the images were conducted by superimposition of the schematic models on STM images as depicted in fig. 5.10.
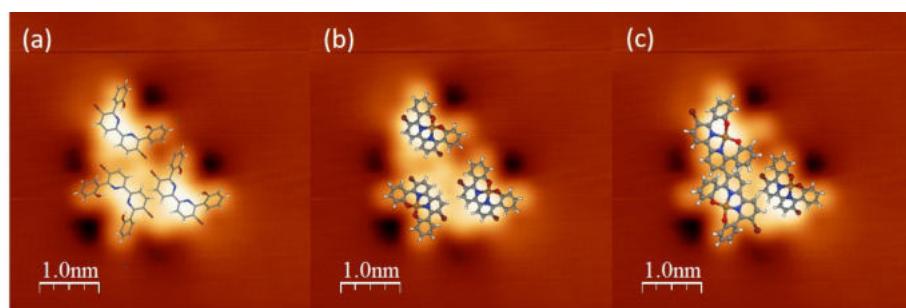
Figure 5.10 Constant current STM images of 3 molecular units adsorbed on MgO superimposed with (a) the salen type ligand without Ni central ion, (b) the gas-phase model of the Ni-salen type, (c) a covalently bonded dimer and a single precursor. Imaging conditions 100mV, 10pA.

From the superimposition of the models onto the same STM image, we can readily exclude the formation of a dimer, even if debromination has occurred, since the size and the shape do not match at all with the experimental data (fig. 5.10 (c)). Between fig. 5.10 (a) and fig. 5.10 (b) models, a better match is found for the model (a) regarding the shape of the phenyl rings looking like ears and the uniform intensity of the two phenyls at the center. Nevertheless, we suggest that the Ni precursor is intact (Ni still present since adsorption occurs only on the oxide surface) but strongly distorted on the surface with the Ni atom pointing towards an oxygen of the substrate and the halogen substituted bonds pointing upwards. The occurrence of an apical bond towards the substrate is further supported by the black hole clearly visible between the phenyl rings suggesting an electron depleted zone. In order to reinforce this conclusion, the distances between the molecular centers were carefully measured. For that, the MgO islands orientation was deduced from the island border by considering the epitaxial pseudomorphic growth on Ag(100) with the $< 100 >$ direction of the MgO lying parallel to the $< 100 >$ crystallographic direction of the silver. The analysis was done on different chains of various units long. The chains of molecules were found to be aligned along the $< 110 >$ or $< 1-10 >$ direction of the MgO and the distances between the units correspond to an integer number of times the Ag reduced lattice parameter supporting the hypothesis that the Ni ion adsorbs in registry with the MgO surface (fig. 5.11). The self-assembly seems to be governed by the interaction with the substrate (manifested in the registry with the MgO network) and intermolecular

interaction seems to be ensured by Van der Waals forces. Further investigations were carried out by DFT calculations conducted at CEMES by H. Tang.
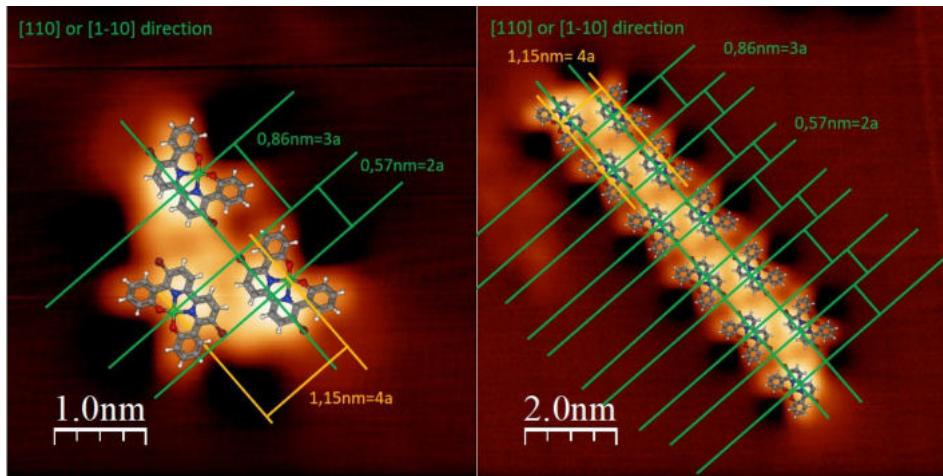

Figure 5.11 Constant current STM images of Ni salen-type ligand displaying that the molecular units are separated by 4 times the Ag lattice parameter along the <110> direction and alternatively 3 times and twice along the <1 − 10> direction. Imaging conditions: 100mV, 10pA.

In first approximation, only a single MgO slab was considered without considering the silver substrate. The results are presented in fig. 5.12. If the Ni ion is located on top of a Mg site, the molecule is lying parallel to the surface and is slightly bended downwards (fig. 5.12 (a) and (b)). On top of an oxygen site, the molecule appears to be strongly distorted with the halogen substituted bond pointing upwards and a stronger bending of the organic skeleton towards the MgO surface. Although an energy gain of −0.105eV was estimated for the configuration with the Ni on top of the Mg site, this latter better describes the experimental system. On top of both O and Mg sites, the main contribution to the adsorption energy is given by Van der Waals contribution with a charge transfer of −0.22 electron towards the Ni on the O site and −0.18 electron towards the Ni on the Mg site. Since in a first approximation the silver substrate was not included, charge transfer and lattice constraint of the MgO were not considered therefore. We would assume a charge tranfer much more important than the calculated one, the energy gain might therefore not be very reliable at this stage. Nevertheless, regarding the adsorption geometry the experimental images seem to be closer to the geometry of the one obtained for Ni on top of O, also expected for electrostatic reasons since the O in MgO is supposed to be charged negative due to its higher electronegativity compared with Mg, the Ni in contrast might be charged positive.

After UV-light exposition and annealing at 373K, debromination might have taken place, but no dimer neither oligomer was found. Though the halogen substituted bond is pointing upwards, any covalent coupling between two adjacent educts is excluded. On the lower panel of fig. 5.12 (a) and (b), a Ni-dimer was considered. Due to the covalent C-C coupling, the Ni ions cannot anymore be both on the top of their energetically more favourable adsorption site introducing an extra cost for the reaction to take place. These two latter arguments point out that with this system Ullmann coupling cannot be achieved.
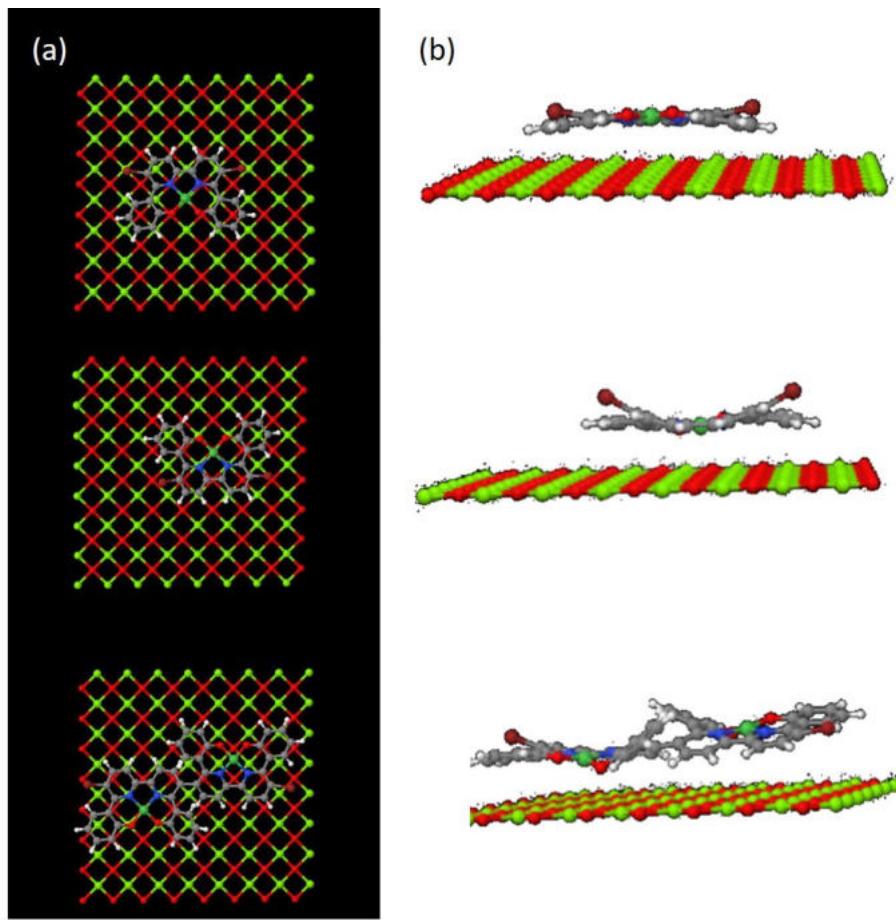
Figure 5.12 DFT calculations on the adsorption of a Ni-Salen type precursor a single MgO slab (a) top and (b) side view of top panel Ni ion adsorbed on Mg site, middle panel: Ni ion adsorbed on O site and lower panel: Ni-salen type dimer. Color code: Mg= light green, O=red, Ni= green, N=blue, C=grey, Br=dark red, H=white.

Since MgO was proven to have a high decoupling efficiency (see § 3.3 "Decoupling efficiency of MgO ultrathin films"), constant current STM images were recorded at different biases corresponding to a resonance with the electronic states of the molecule and then compared with the orbitals calculated by DFT for a Ni-salen type precursor in gas phase. Fig. 5.13 presents a dI/dV spectroscopy together with the calculated LUMOs and the corresponding constant current STM of the Ni-salen precursors. As molecules mainly adsorb self-assembled as double row as shown in fig. 5.11, the direct comparison is difficulted by the presence of more than one molecule. Nevertheless, from this comparison, we can deduce that debromination did not take place since intensity on the Br location is clearly visible. We might assume that the distortion of the molecule and with this related the long distance between Br and Ag-surface might be responsible for that.

A view single molecule were found, but all of them adsorbed nearby a defect appearing as a large black crescent hole and only one STM image at 1.7V was recorded (fig. 5.14). This is worth to note that, depending on charge transfer, LUMO might be populated and become a HOMO state, or, if the charge transfer occurs in the other direction i.e. from the molecule to the substrate, the HOMO state might be depopulated and therefore to
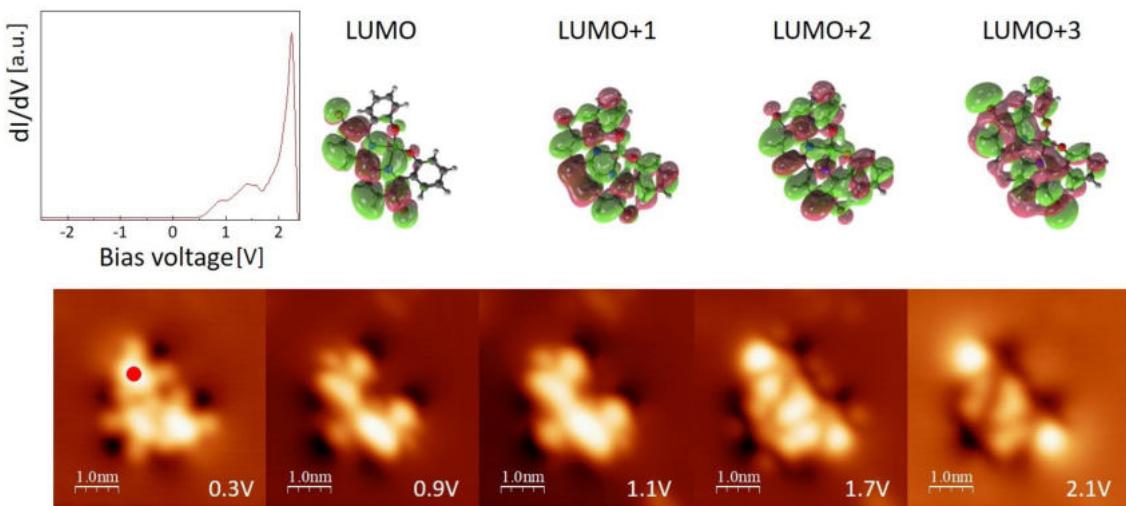
Figure 5.13 Top panel. *dI/dV* spectroscopy recorded at the location marked with a red dot, DFT calculated orbitals of the Ni salen type in gas phase. Bottom panel: Constant current STM images of the Ni-salen type adsorbed on MgO decoupling layer. The bias voltages are indicated in the images. Tunneling current: 10pA.
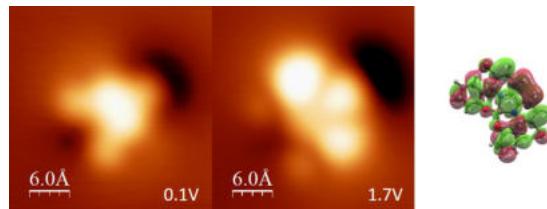
Figure 5.14 STM images of a single Ni-salen molecule adsorbed nearby a defect. The resonant state at 1.7V presents some similarities with the DFT calculated LUMO+1. Tunneling current: 10pA.

appear as LUMO. On pentacene adsorbed on MgO ultrathin film, a charge transfer of an entire electron was reported and explained as a tunneling charge transfer with therefore only entire charge being transferred through the MgO [128]. The DFT calculations were done for a neutral molecule.

Since, Ullmann coupling seems to be prevented by the adsorption geometry of the precursors and registry with the MgO lattice, another strategy has been employed in order to attempt to polymerize the precursors through dehydrogenation. The sample was therefore annealed at a temperature as high as 573K for 15 minutes. Different dimers were found as well as a number of other "strange" species that we could not identify. Fig. 5.15 presents the expected planar Ni-salen type dimer after dehydrogenation. The electronic structure has been completely modified as well as the gap. HOMO states are now present, while no occupied state was detected on the monomer. The second type of dimer was obtained by dehydrogenation of two precursors attached "back to back" giving rise to a rectangular shape dimer as displayed in fig. 5.16. For both dimers, a schematic representation is superimposed on the first STM image in order to identify them.
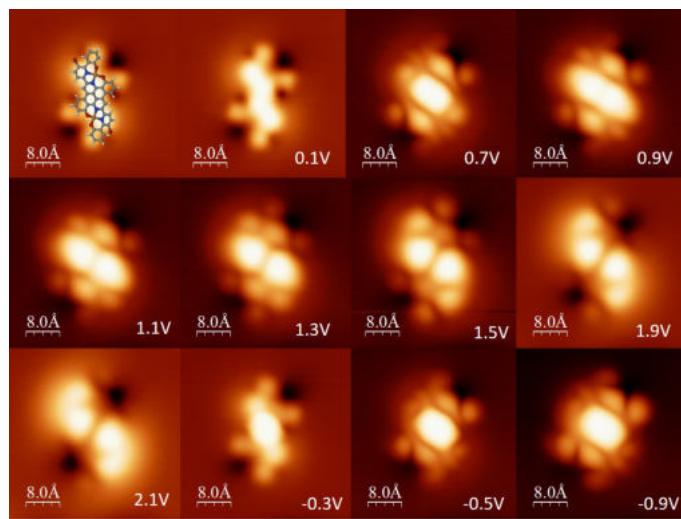
Figure 5.15 Constant current STM images recorded at various biases of a Ni-salen dimer after dehydrogenation. Tunneling current: 10pA.
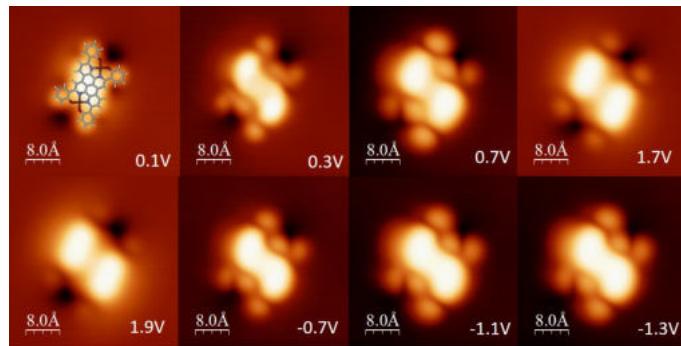
Figure 5.16 Constant current STM images recorded at various biases of a second type of Ni-salen dimer after dehydrogenation. Tunneling current: 10pA.

5.4 Conclusion

Two types of precursors derived from salen were studied on various substrates. The coordination bonds of the Cu-salen type were too labile and only the organic skeleton was left upon deposition on the metal surfaces giving rise to a large number of self-assemblies on both (100) and (111) silver substrates with a predominance of the rotated S-shape ligand. The second precursor based on Ni was demonstrated to be more robust and was found to adsorb preferentially on MgO islands grown on Ag(100). The adsorption geometry and the registry with the surface have played an important role in preventing Ullmann coupling. Self-assembly was observed with double row of precursors "back to back". Finally, dimerization was successfully achieved by dehydrogenation. The decoupling efficiency of the MgO ultrathin film was demonstrated allowing to access directly by STM imaging to the electronic state spatial extension of the adsorbate. Despite the fact that Ullmann coupling was not achieved in this case, this study could be used as a proof of concept for direct chemical reactions on top of MgO ultrathin films, which has, to our knowledge, never been reported before. By designing carefully specific precursors other chemical reactions could be imagined on this surface.

6 Conclusion and perspectives

Surface structuring by on-surface synthesis has gained increasing interest in the research of the last two decades. The bottom-up technique of creating covalent bonded networks directly on the surface by using molecular precursors as building blocks has been greatly developed and numerous reactions have been successfully realized. The presence of strong interactions between single molecules through covalent or coordination bonds improves electron transfer, that is strongly hindered in self-assembly films. It is specially required for the development of numerous applications. These span wide fields ranging from biological and ecological devices e.g. as bio-sensors or CO_2 capturing, over optics such as single molecule luminescence, to magnetic compounds such as spintronics e.g. data storage and quantum computers, and electronics such as field effect transistors.

Between various types of precursors that have been used, organometallic coordination complexes were specially in the focus of research and development because of their unique magnetic and electronic properties. Among them Porphyrins, salen and salophen are the best known. The big variety of structural, electronic and magnetic properties tunable by the choice of ligands attached to the central unit makes them to popular candidates. Of striking importance for the successful development of devices is the structural control over long range order realized by using chemically well defined building blocks and templating substrates. Equally crucial is the electronic decoupling from the metallic substrate to preserve the intrinsic electronic and magnetic properties of the created structures. This is realized e.g. by ultra thin oxide layers epitaxially grown on the substrate as intermediate layer keeping the advantage of metallic substrate to be used for surface sensitive analysing techniques.

The aim of this thesis was to establish a successful strategy to achieve chemical reactions on insulating surfaces using halogen functionalized molecules as building blocks. The coupling reaction we chose among a big variety of available candidates was the Ullmann reaction consisting of three steps: first, C-halogen bonds are cleaved to activate the process under creation of radical species, they diffuse over the surface and create an organometallic intermediate state where they are bound to Ag adatoms from the substrate, finally, C-C coupling occurs under elimination of the intercalated Ag atoms. The substrate as mechanical support is also used to catalyse the process. The activation energy necessary to initiate the chemical reaction by bond cleavage and to allow diffusion could be given by thermal heating where cleavage and diffusion occur both together, or by UV-light, which introduces an additional parameter to control the reaction separating cleavage and diffusion. It serves to lower the reaction temperature, which is often a limiting factor in view of rather weak bonds in metal coordination networks.

The strategy we followed was to grow an ultra thin MgO layer on the Ag(001) substrate $(1 - 2$ monolayers thick), which presents the advantages of keeping a wide band gap (about 6eV) to avoid efficiently molecule-metal hybridization, but still enabling STM measurements and also being transparent in the UV range. Moreover, it can be well epitaxially grown on the Ag(001) substrate because of the small mismatch between both lattice constants. Therefore, the growth conditions were studied in order to control thickness, domain size and electronic properties to obtain large, flat and defect-free MgO ultrathin films (§ 3). In the following we studied simple precursors - model molecules - in order to characterize the different stages of chemical reaction activated by temperature and UV light at metal surface and to attempt direct chemical reaction between model molecules by UV light exposition at oxide surface (§ 4). Last but not least we studied the chemical reaction stages using UV light of more complex precursors (Cu- and Ni-salen type) on top of an ultrathin oxide layer and the properties of the resulting product. (§ 5).

We determined the parameters to grow large and almost defect free islands of MgO on Ag(001). From the study carried out by GIXRD, bilayer growth mode was obtained for two different substrate temperatures giving rise to islands of wide lateral extension with a very small roughness of $\beta = 0.06(1)$ corresponding to a R.M.S. value of 53pm. Growth-mode and purity of MgO islands were shown to depend sensitively on different parameters during and after deposition such as substrate temperature, O_2 partial pressure, cooling conditions and surface coverage. Our STM study points out the overriding role of the deposition rate to switch from the bilayer regime to the monolayer regime. The obtained lateral extension of the islands was at least 50nm and they were found to be surrounded by silver adatoms. At low bias, the monolayer islands appear as embedded into the substrate and STS confirms their insulating character with a band gap larger than 5.5eV. Finally, the work function of the monolayer was extracted from spectroscopic data of Field Emission Resonances (FERs) giving rise to a work function decrease of the silver substrate of 0.6eV due to the presence of the MgO ultrathin film.
This first step was of fundamental importance to get well controlled insulating films, especially, since it was pointed out that the use of MgO films rather than bulk MgO presents a significant advantage as substrate in chemical reactions[102].

Diiodo-p-terphenyl and dibromo-p-terphenyl were studied on two different metallic substrates, namely Ag(111) and Ag(001) surface. First, single molecules were characterized and in the following a temperature dependent study was conducted. Energetic and structural properties of different reaction stages, specially in the context of substrate influence were examined. Results obtained with and without UV-light were compared in order to determine UV-light irradiation effect on the on-surface chemical reaction. We can conclude that (I) the reaction temperature to achieve poly-para-phenylene wires was lowered by 50K and (II) surface reactivity was enhanced to become similar to much more reactive substrates such as Cu(111). A direct excitation of the adsorbate can be readily excluded and therefore, the effect of UV exposition might be due to substrate mediated

excitation. In particular, plasmon induced hot carrier generation and hot electron transfer in the adsorbate might be at play, since the catalytic activity of the substrate is clearly improved. On Ag(100), surface plasmon energy was reported at 3.69eV corresponding to 336nm wavelength, which is indeed provided by the Xe lamp used in this study.

It has to be mentioned that this study brings a novel aspect compared with former reported works, as UV-light irradiation was carried out on organometallic species to excite C-C-coupling as last reaction step. As the lowered reaction temperature allows the polymerization to occur at milder conditions, this is specially interesting for applications to other systems with larger or more fragile molecules that might not stand annealing at high temperatures. Due to technical limitations of our experimental setup, i.e. the impossibility to shine UV light on the sample maintained at low temperature, organometallic wires were found to be created on uncovered metallic surfaces. The high diffusion coefficient of the dehalogenated species and the high bonding energy of the poly-para-phenylene wires on Ag(100) surface prevent any further STM tip manipulation to transfer them onto MgO islands. For future experiments it could therefore be interesting to attempt light irradiation at low temperature.

In the last part of this work coordination complex precursors were used taking advantage of their lower diffusion rate and possible higher interaction with the oxide surface. The brominated precursors were synthesized at CEMES and derived from salen and salophen ligands. A Cu-salen type was first studied on Ag(001) and on Ag(111) substrate, but the bonds were found to be too labile to keep intact their molecular architecture. The organic skeleton was left upon deposition giving rise to a large number of self-assemblies on both (100) and (111) silver substrates with a predominance of the rotated S-shape ligand. The second precursor based on Ni was demonstrated to be more robust. Deposited on a partly MgO covered Ag(100) substrate, it was found to adsorb preferentially on MgO islands. Ullmann coupling was not achieved due to the adsorption geometry of molecules and the registry with the surface, instead, self-assembly double rows were found. Thanks to the decoupling efficiency of the MgO ultrathin film the spatial extension of the electronic state of the adsorbate could be imaged directly by STM. Finally, dimers could be successfully created by cyclodehydrogenation on the MgO surface.

We can report on the advancement of several points of interest in recent research: the preparation of ultrathin and nearly defect free MgO layers on Ag(100) substrate is the basis for decoupling of on-surface polymerized molecular structures, necessary to access to their intrinsic electronic and magnetic properties and therefore fundamental for the development of devices. The successful reduction of the reaction temperature of Ullmann coupling allows the use of more fragile precursors and avoids defragmentation and desorption of molecules. Furthermore, light induced on-surface polymerization also opens the way to use insulating thin oxide films as substrate, where the adsorption energy of molecules is often decreased and the catalytic activity of the underlying metal is suppressed. Finally, the polymerization by dehydrogenation of salen type precursors serves as a proof of concept for direct chemical reactions on top of MgO ultrathin films, which has,

to our knowledge, never been reported before. By designing carefully specific precursors other chemical reactions could be imagined on this surface.

We are looking forward to numerous promising developments in the field of on-surface synthesis, where actually graphene nanoribbons (GNs) are specially in the center of interest. Just to name some examples, zigzag-edged graphene nanoribbons (ZGNs) with precisely-tunable π-magnetism hold great potential for applications in spintronics and quantum devices. In conventional wet chemistry substitutional groups are often introduced to protect their reactive edges to improve their stability and processability. This renders difficult to study their intrinsic structural and spin-polarized properties. In contrast, by on-surface bottom-up synthesis the fabrication with atomic precision of both unsubstituted ZGNs and functionalized ZGNs could be realized [170].

In order to use a material to construct electronic switches, it must not only be an outstanding conductor, it should also be switchable between "on" and "off" states. This requires the presence of a bandgap, which enables semiconductors to be in an insulating state. On-surface synthesis opens the way to the polymerization of ultra-narrow graphene nanoribbons with larger bandgaps than conventionally processessed GNs [171].

Further, doping with "foreign atoms" in precisely defined positions can create so-called heterojunctions between the individual segments of GNs. Researchers have shown that these display similar properties to those of a classic p-n-junction, i.e. a junction featuring both positive and negative charges across different regions of the semiconductor crystal. Thereby the basic structure is created for the design of many components used in the semiconductor industry e.g. the development of solar cells.

7 Resumé en français

L'objectif principal de ce travail était de réaliser des fils moléculaires covalents, étendus directement sur des surfaces métalliques et des surfaces d'oxyde par synthèse sur la surface sous ultravide (UHV) et d'étudier leurs propriétés électroniques. Après d'une brève introduction (§ 1), § 2 présente l'état de l'art des expériences en synthèse sur des surfaces métalliques et isolantes, ainsi que la stratégie suivie dans ce travail et les méthodes expérimentales utilisées. Les détails les plus importants sont ici resumés en français.

7.1 L'état de l'art, l'objective et la stratégie de ce projet

Les molécules sur des surfaces ont suscité un grand intérêt scientifique et technologique au cours des 40 dernières années. L'énorme quantité d'études, qui ont été réalisées, traite de l'auto-assemblage de monocouches moléculaires. Il permet de créer des réseaux 2D de molécules organiques et organométalliques, ou de complexes de coordination, hautement ordonnés et étendus sur des grandes surfaces. Les interactions intermoléculaires en jeu sont plutôt faibles. Il s'agit des interactions de Van der Waals, électrostatiques, métal-ligand, dipôle-dipôle et des liaisons hydrogène ou halogène.

L'apparition d'un certain type d'arrangement moléculaire est déterminée par la compétition entre des différentes valeurs d'énergie telles que l'énergie d'adsorption E_{ads} et la barrière de diffusion E_{dif} des molécules sur la surface, leur énergie cinétique E_{kin} et l'énergie d'interaction intermoléculaire E_{int}. Le contrôle de la température fournit donc des informations précieuses concernant la diffusion, et aussi la vitesse et l'énergie d'activation de la réaction, ainsi que des paramètres thermodynamiques tels que l'entropie et l'enthalpie de divers processus. Ne pas seulement la température de recuit, mais aussi l'historique de la croissance, c'est-à-dire la séquence détaillée des températures appliquées pendant et après le dépôt des molécules, est donc critique pour le processus de structuration.

L'énergie d'adsorption des molécules E_{ads}, leur énergie de diffusion E_{dif}, ainsi que les interactions intermoléculaires sont directement liées aux interactions molécule-substrat. Si les forces d'attraction entre les molécules et le substrat sont plus fortes que celles entre les molécules, l'arrangement moléculaire de la couche auto-assemblée est alignée le long des axes principaux cristallographiques du substrat. Par conséquent, la position et l'orientation des molécules relative au substrat et par conséquent la longueur des liaisons intermoléculaires dans le réseau 2D dépendent de la symétrie du substrat, qui défini ainsi l'énergie de liaison. En revanche, si l'interaction avec le substrat est plutôt faible, les structures moléculaires suivent leur propre symétrie et ne sont même pas perturbées, quand elles traversent les bords de marches du substrat sous-jacent.

Non seulement pour l'auto-assemblage moléculaire, mais aussi pour toute interface métal-organique, il est d'intérêt fondamental de comprendre les règles qui régissent les propriétés électroniques. En particulier, pour les applications dans les dispositifs électroniques il est cruciale de connaître l'alignement des niveaux d'énergie directement en jeu et le transport de charges. Il a été démontré que les niveaux de vide de l'organique et du métal $E_{vac}(O)$ et $E_{vac}(M)$ ne sont pas alignés, mais lors du dépôt de la première couche moléculaire sur le métal, une chute abrupte d'E_{vac} entre le métal et l'organique a lieu, créant une barrière dipolaire d'interface Δ [3]. Elle peut être orientée dans des directions différentes et est la somme de divers composants dépendants du choix du substrat métallique avec sa fonction de travail spécifique Φ_M et des niveaux d'énergie moléculaire de l'adsorbat. Comprendre les détails permet de déterminer et de contrôler la structure électronique à l'interface.

Dans les films moléculaires auto-assemblés, l'absence d'interaction forte entre les molécules limite fortement leurs applications, en particulier en termes de transfert d'électrons (hopping) à travers ces structures et de leur stabilité. Ainsi, la création d'interactions fortes entre les molécules telles que les liaisons covalentes ou coordonnées est d'un grand intérêt et une forte motivation pour la recherche. Une synthèse aurant lieux directement sur la surface, est très avantageuse dans l'optique de que les molécules multifonctionnelles deviennent grandes et fragiles et leur incorporation dans un environnement solide reste limitée aux méthodes de transfert disponibles. Un autre point intéressant à souligner est que la synthèse sur surface se déroule dans un environnement sans solvant, ultra-propre et dans une plage de température accessible qui est plus large qu'en solution. Il permet d'accéder à des mécanismes de réaction originaux dans des conditions douces, ce qui ne serait pas possible en chimie standard. Ces avantages sont combinés avec les techniques de characterisation des surfaces disponibles, qui permettent de visualiser chaque étape de la réaction avec une précision atomique [17], [18].

Cette approche s'appuie sur la chimie pour concevoir et synthétiser des molécules multifonctionnelles utilisées comme précurseurs, mais les structures des produits finaux sont aussi influencées par d'autres conditions, telles que la nature chimique et la symétrie du substrat sous-jacent. Il a été prouvé que, dans la plupart des cas, les surfaces métalliques ne sont pas seulement utilisées pour soutenir les réactions, mais peuvent également servir de catalyseurs de réaction ou participer directement aux réactions via des états organométalliques. Les propriétés électroniques des adsorbats sont largement atténuées sur un métal, alors qu'elles sont préservées sur un substrat isolant. Afin d'atteindre les propriétés intrinsèques des fils 1D ou des réseaux 2D synthétisés sur la surface, ces structures doivent donc être transférées sur des isolants. Jusqu'à présent, la grande majorité des études publiées ont été réalisées sur des surfaces métalliques, beaucoup moins sur des surfaces isolantes (par exemple [24], [25], [26] [27], [28]). Soit les réactions chimiques étaient faites directement sur l'isolant ou les fils moléculaires étaient transférées sur l'isolant après la synthèse sur métal. La grande bande interdite de ces substrats empêche l'utilisation du STM, les mesures dans ces études étaient donc effectuées par AFM. De contrôler la synthèse de ces matériaux uniques directement sur des surfaces isolantes et de réaliser des structures 2D bien

définies liées de manière covalente reste des défis principaux émergents dans ce domaine. Un des inconvénients les plus importants de la synthèse sur des substrats non métalliques est la faible énergie d'adsorption des molécules sur la surface, qui est généralement surmontée en utilisant des basses températures d'échantillon, incompatible avec l'activation thermique des précurseurs. De plus, des matériaux isolants avec une large bande interdite sont relativement inertes en raison de l'absence d'électrons au niveau de Fermi, donc l'induction d'une réaction chimique directe sur ces substrats pourrait difficilement se produire. Une alternative intéressante pour des substrats isolants bulk, à laquelle il faut donc prêter attention, est l'utilisation d'un film de découplage ultrafin, où l'imagerie STM et la spectroscopie sont encore possibles. L'activation de la réaction sur ces surfaces se fait en utilisant la lumière UV en lieux d'une activation thermique, tout en gardant la température au plus bas possible. Des matériaux appropriés comme film de découplage en raison de leur inertie chimique, excellente stabilité en température, leur haute résistivité électrique avec une large bande interdite et de leur dureté mécanique sont des oxydes, notamment des films d'oxydes ultrafins, qui de plus présentent une croissance épitaxiale sur des surfaces métalliques.

L'une des réactions à la surface les plus souvent utilisées est le couplage d'Ullmann, qui est extrêmement efficace et robuste et qui a été largement utilisée avec succès pour la synthèse de GNR à partir de différents précurseurs avec des résultats impressionnants. La synthèse sur surface de nanostructures 1D par réaction d'Ullmann est également très importante en termes d'effort de recherche. Parmi les fils, le poly-para-phénylène (PPP) est une cible classique et reste un modèle approprié pour étudier le mécanisme de réaction. Comme il n'y a pas des produits de réaction secondaire, les produits résultants du couplage d'Ullmann peuvent être identifiés sans ambiguïté en mesurant la distance entre les monomères dans les images STM.

La réaction de couplage d'Ullmann repose sur l'utilisation de précurseurs halogénés et peut être décrite par deux étapes réactionnelles de base : (i) l'activation du précurseur par clivage de la liaison C-halogène afin d'obtenir des espèces réactives et (ii) l'activation de la diffusion sur la surface afin de coupler les monomères déshalogénés via des liaisons $C - C$ covalentes. Néanmoins, un état intermédiaire résultant en la formation d'une espèce organométallique est souvent observé en fonction du métal en jeu [38]. Les propriétés électroniques et catalytiques de ce dernier et le nombre d'halogènes dans le precurseur, sa taille et l'emplacement des substituants sont donc les paramètres clés qui déterminent le produit final de la réaction.

L'objectif de ce travail était donc de synthétiser des fils 1D sur des surfaces métalliques et, plus difficile, aussi sur des surfaces isolantes afin d'étudier leurs propriétés électroniques intrinsèques.

La stratégie complète pour obtenir les produits souhaités doit prendre en compte la conception des précurseurs (symétrie, taille, fonctionnalisation, couplage séquentiel, encombrement stérique), la méthode d'activation (impulsions de la pointe STM, exposition à la lumière ou chaleur), les paramètres de croissance (température du substrat, vitesse de dépôt, stœchiométrie, couverture), le substrat (nature chimique, orientation, gabarit, croissance épitaxiale) et la structure supramoléculaire (matrice supramoléculaire et coordination métallique). Dans ce travail nous avons utilisé un film d'oxyde ultra-mince comme couche de découplage du substrat métallique, ce qui permet l'utilisation du STM et d'activer la reaction Ullmann entre les précurseurs halogénés par la lumière UV et/ou la température. Les différentes étapes que nous avons suivies étaient les suivantes:

- Étudier la croissance d'une couche d'oxyde ultra-mince sur un substrat métallique afin de contrôler l'épaisseur, la taille du domaine et les propriétés électroniques (§ 3).

- Étudier des précurseurs simples - des molécules modèles - afin de caractériser les différentes étapes de la réaction chimique, activée par la température et la lumière UV sur la surface metallique et tenter une réaction chimique entre ces molécules directement sur la surface de l'oxyde par exposition aux UV (§ 4).

- Étudier les étapes de la réaction chimique de précurseurs plus complexes activée par la lumière UV et les propriétés électroniques de la structure obtenue sur une couche d'oxyde ultrafine. (§ 5).

7.1.1 Choix des précurseurs et du film ultrafin isolant

Afin d'obtenir des fils 1D, deux précurseurs différents ont été choisis. Le premier est l'un des précurseurs les plus simples que l'on puisse trouver, consistant en trois cycles phényles fonctionnalisés par deux halogènes, le dibromo-p-terphényle (DBTP) et le diiodo-p-terphényle (DITP). Ils sont utilisés dans ce travail comme précurseurs modèles pour comprendre les différentes étapes de la réaction et de déterminer l'influence des paramètres contrôlables tels que la température du substrat pendant et la vitesse du dépôt, la température de recuit, etc. L'objectif de cette première étude (détaillée dans § 4) sur ces précurseurs modèles est également de déterminer l'influence de l'exposition à la lumière sur la réaction d'Ullmann, puisque l'objectif final est de synthétiser des fils 1D sur des couches isolantes.

Le deuxième précurseur que nous avons choisi est un type salen fonctionnalisé par des halogènes, nommé type Cu-salen et type Ni-salen. Le choix est basé sur plusieurs raisons,

la première est que la présence d'un ion métallique dans l'architecture du précurseur (complexe de coordination) est censée modifier l'interaction entre la molécule et la surface, avec une plus grande affinité vers l'oxygène d'un oxyde que sur le métal. La deuxième raison est que ce type de précurseur de complexe de coordination pourrait présenter des nouvelles caractéristiques électroniques et magnétiques due à une liaison covalente lors de la réaction. La troisième raison est que cette voie est à ce jour totalement inexplorée (détaillée dans § 5).

Nous avons utilisé un film ultrafin de MgO comme couche de découplage. En consultant la littérature, les films ultrafins de MgO répondent aux exigences de cette étude avec une bande interdite supérieure à 6eV, même à très faible couverture [40], [41]. De plus, la croissance épitaxiale de films ultrafins de MgO a été réalisée avec succès sur de nombreuses surfaces. En outre, les films ultraminces de MgO présentent d'autres avantages décisifs, le premier étant sa stabilité en température jusqu'à 1300K [62], le second, crucial pour atteindre notre objectif, est sa réactivité relative. Il s'est présenté comme un catalyseur efficace à basse température [63], [65], [66] et la formation de radicaux O_2^- a été démontrée [64]. Enfin, le troisième argument fort en faveur des films ultraminces de MgO réside dans le fait que le substrat métallique n'est jamais entièrement recouvert par l'oxyde, laissant place à la réaction chimique sur le métal et aux procédures d'affûtage de la pointe.

7.1.2 Photochimie sur la surface

D'utiliser la lumière pour activer des surfaces est utilisé depuis 40 ans, notamment dans le domaine de la catalyse pour améliorer l'activité ou la sélectivité des métaux ou des oxydes. Des processus photoinduits sur les adsorbats sur des surfaces solides provoquent un certain nombre de phénomènes qui peuvent être classés comme (I) désorption, (II) dissociation et (III) réaction. Dans un certain nombre de réactions chimiques photoinduites, la dissociation a lieu avant la réaction. L'avantage principal de l'utilisation de la lumière au lieu de la chaleur est d'amener le processus de polymérisation dans des conditions douces et d'améliorer la sélectivité en ne favorisant que certaines réactions chimiques et pas d'autres.

La lumière peut exciter spécifiquement les transitions vibratoires d'un adsorbat, qui peuvent être transférées dans des modes molécule-surface de basse fréquence et entraîner la désorption de l'adsorbat. Le complexe adsorbat-substrat peut également être excité électroniquement. Le système subit une transition d'un état de liaison à un état d'anti-liaison avec la conséquence de la désorption de l'adsorbat. Le processus a été décrit en détail par Menzel et Gomer [73] et par Redhead [74] (modèle MGR). Malheureusement, en raison d'une couplage électronique direct entre l'adsorbat et le substrat, le rendement de ces processus est plutôt faible. L'excitation se détend dans le bain de chaleur fourni par le solide, plutôt qu'un transfert d'énergie dans le mode de surface peut avoir lieu, ce qui est appelé "chauffage résonnant". Surtout dans des substrats métalliques un nombre prèsque infini d'états de paires électron-trou est fourni, qui en couplage avec les états excités de l'adsorbat diminue leur durées de vie (< 10-14s), de sorte que seule une petite fraction des molécules excitées gagne suffisamment d'énergie pour permettre le clivage des liaisons. En

conséquence la dissociation des liaisons moléculaires par excitation directe se produit très rarement sur des surfaces métalliques. Néanmoins, le taux d'extinction dépend du type du substrat. Sur les oxydes, en raison de l'existence d'une bande interdite, ce taux est moins prononcé. En effet, les surfaces utiles des processus photoinduits peuvent s'étendre sur 5 ordres de grandeur et diminuer dans l'ordre oxydes > semi-conducteurs > métaux nobles [67],[68]. Ces conclusions confirment que l'utilisation de la lumière pour promouvoir les réactions chimiques sur les surfaces d'oxyde pourrait être une stratégie efficace pour la polymérisation directe.

A part d'une excitation directe de l'adsorbat ou du complexe adsorbat-substrat, les processus photochimiques peuvent également être excités de manière indirecte à travers le substrat. Le mécanisme le plus probable de se produire est la création des électrons libres dans le substrat, appelés "électrons chauds". L'absorption de la lumière par le métal crée des paires électrons-trou, qui avec suffisamment d'énergie sont séparées et des "porteurs chauds" sont créés. Grâce aux nombreux événements de diffusion qui se produisent, la distribution d'énergie des électrons chauds s'étend sur une large gamme d'énergie. Dans l'espace, l'absorption des photons s'étend sur la profondeur de pénétration de la lumière entrante. Si le parcours libre moyen des électrons est du même ordre, les électrons chauds initiaux, créés par l'absorption de photons, atteindront la surface avec une probabilité élevée. Ils peuvent alors pénétrer par effet tunnel dans l'état LUMO des molécules, formant ainsi un anion transitoire par "Hot Electron attachment" (HEA), qui conduit à la dissociation de la liaison intramoléculaire par "Dissociative Electron Attachment" (DEA). En outre, dans les métaux nobles comme l'Ag des fortes résonances plasmoniques améliorent l'efficacité de l'HEA [76],[77],[78]. Une autre caractéristique intéressante à mentionner concernant l'irradiation lumineuse est que les films ultraminces d'oxyde sont transparents à la lumière visible et UV et que leur effet pour l'absorption peut être négligé [79].

Quel que soit le processus d'excitation en jeu, directe ou indirecte, les molécules adsorbées transiteront par des espèces excitées, négativement chargées ou neutres, qui finalement se relaxent par l'excitation des états vibrationnels de Frank Condon, provoquant la rupture des liaisons, ce qui est l'objectif ici pour la synthèse sur la surface.

7.2 Études sur la croissance des films ultraminces de MgO

L'oxyde de magnésium cristallise avec une structure du type sel gemme avec une constante de réseau (421.1pm) similaire à celle de la surface (100) de l'Ag [94]. La petite différence des paramètres de maille des deux réseaux (3.1%) rend possible la croissance épitaxiale des films minces de MgO sur Ag(100) avec MgO[100] parallèle à Ag[100] [95]. Les films d'oxyde adoptent une croissance couche par couche et sont pseudomorphes, c'est-à-dire que la couche épitaxiale est latéralement déformée (comprimée) afin de conserver le réseau cristallin. Au-dessus de l'épaisseur critique, la contrainte est libérée par l'intermédiaire de dislocations avec des plans de glissement {110} [49] et la constante de réseau augmente progressivement de l'Ag(100) bulk à celui du MgO(100) bulk. Ceci mérite

d'être mentionné que tout mélange significatif avec le substrat Ag a été exclu [62]. Concernant la structure électronique du MgO, une large bande interdite dans le bulk et des couches épaisses entre 6 et 7.8eV a été mesurée [94], [41]. Les calculs électroniques de la monocouche de MgO montrent une diminution de la bande interdite de 7.8eV à 3.1eV par rapport à celui de sa phase massive [97].

En section § 3, l'étude de la croissance des films minces de MgO est présentée plus en détail. Les conditions (température du substrat, traitements, vitesse de dépôt, pression partielle d'oxygène, épaisseur), qui ont été testées et les résultats principaux des études de croissance rapportées dans la littérature (taille des îlots, forme, couverture lorsqu'elle est indiquée) sont résumés. D'après l'analyse de la littérature, un dépôt de Mg suivi d'une post-oxydation peut être facilement exclu. Les meilleurs résultats ont été obtenus pour une température du substrat relativement élevée, mais il apparaît que le paramètre critique est la vitesse de dépôt. Nous avons réalisé une première étude par Grazing Incidence X-ray Diffraction (GIXRD), afin de déterminer l'influence de la température du substrat entre 620K et 670K (voir § 3.1) et une seconde étude par LT-STM pour étudier l'influence de la vitesse de dépôt (voir § 3.2).

7.2.1 Résultats de l'étude GIXRD

L'une des difficultés principales des études de croissance est de surveiller les caractéristiques du film pendant le dépôt, ce qui peut être réalisé par la diffraction des rayons X à incidence rasante (Grazing Incidence X-ray Diffraction, GIXRD). Elle permet d'analyser la structure non seulement une fois que la couche est déposée, mais aussi pendant la croissance. L'analyse des résultats permet d'extraire avec précision les paramètres du réseau, la taille des domaines et les propriétés des interfaces. Cette étude a été réalisée avec Maurizio de Santis de l'Institut Néel et Dr. Xavier Torrelles de l'Institut des Sciences des Matériaux de Barcelone (ICMAB). Les résultats expérimentaux présentés ont été obtenus au "European Synchrotron Radiation Facility" (ESRF), Grenoble, France.

Plusieurs échantillons d'une épaisseur nominale de 0.8ML ont été développés avec une vitesse de dépôt de 0.2ML/min à une température de substrat T_s de 620K, 670K et 720K respectivement. Les conditions de croissance étaient orientées à des préparations référées dans la littérature, qui donnaient des grandes terrasses plates avec une faible densité de défauts [40] [51], uniquement la température dans notre préparation était un peu plus élevée. La composition était vérifiée par AES en mesurant les pics Auger de Ag, O et Mg à $356eV$, $513eV$ et $1200eV$. Les échantillons élaborés à $T = 620K$ et $T = 670K$ donnaient des amplitudes du signal MgO similaires, alors que pour celui élaboré à $T = 720K$ le signal était très faible, ce qui montrait que le Mg est désorbé de la surface avant qu'une couche stable de MgO n'a pu se former. Ensuite sur les deux premiers échantillons, des mesures de diffraction des rayons X en surface (SXRD) ont été effectuées à température ambiante, afin de résoudre leur structure.

La SXRD est une technique puissante pour résoudre la structure des surfaces cristallines. L'intensité de diffraction par un cristal tronqué présente une distribution nette en scannant la transmission des impulsions parallèle à la surface et une distribution continue en direction hors plan. Cette distribution de l'intensité hors plan aux indices entiers (HK) de la maille de surface est connue comme (HK) crystal truncation rod (CTR) [104]. Lorsqu'un film croît en registre avec le substrat, il apporte une contribution de diffraction qui interfère avec le CTR du substrat. La structure du film peut alors être résolue par une analyse détaillée des intensités CTR [105]. Les amplitudes du facteur de structure obtenues pour les échantillons élaborés à $T = 620K$ et $T = 670K$ montrent des caractéristiques de bicouche et de la croissance d'une troisième couche respectivement. Ceci etait confirmé par une analyse quantitative en comparaison avec les modèles structurels considérant des différents épaisseurs de MgO sur la surface de l'argent. L'espacement entre les deux premières couches d'argent en contact avec le MgO était trouvé légèrement élargi par rapport à l'argent propre, tandis que l'espacement entre les couches 2 et 3 d'argent était légèrement comprimé. En outre, le site d'adsorption du MgO était déterminé avec l'oxygène adsorbé sur les atomes d'argent et le Mg sur les sites creux.

7.2.2 Résultats de l'étude STM

L'étude de la croissance du MgO a été complétée par une étude LT-STM afin de vérifier l'influence de la vitesse de dépôt sur la qualité des îlots en termes d'épaisseur, de forme et de structure électronique. Une procédure de post-recuit avec et sans pression partielle d'oxygène a également été étudiée afin de vérifier son effet sur la rugosité des îlots. La méthodologie appliquée, le principe de fonctionnement du STM et la préparation des échantillons est détaillée dans § 2.3 Methodology.

Deux études comparatives ont été réalisées. La première à un taux de dépôt constant de 0.3ML/min (puissance 3.4W) avec des différentes pressions partielles d'oxygène et différentes températures de l'échantillon et la seconde a été réalisée en fonction de la vitesse de dépôt à température constante du substrat. Les résultats principaux étaient les suivants: L'oxygène en excès donne des îlots rugueux, dont la rugosité ne s'améliore pas avec le post-recuit. Un effet possible du post-recuit est de rendre les îlots plus grands, comme déjà rapporté par Pal et al. [53]. Selon eux, les îlots en forme de flocon, comme nous les avons trouvé aussi, pourraient être dus au refroidissement rapide après le dépôt. De la deuxième étude, nous pouvons déduire que l'augmentation du taux de dépôt favorise des îlots ML, alors que les taux de dépôt plus faibles entraînent une croissance 3D. Les meilleurs résultats ont été obtenus d'une préparation avec une source de puissance élevée de 5.3W correspondant à 1ML/min, à une pression partielle d'oxygène légèrement plus faible de 5×10^{-7}mbar et un post-recuit de $5'$ à 670K sans oxygène. Les îlots de MgO formés dans ces conditions avaient une épaisseur d'une monocouche et une largeur d'au moins 50nm. De plus, la rugosité des îlots de MgO était très faible, de l'ordre de 30pm, ce qui était l'objectif à atteindre. Les défauts étaient situés à l'interface métal/oxyde.

La hauteur apparente des îlots de MgO change radicalement en fonction de la polarisation appliquée pour acquérir les images STM. En effet, à faible polarisation, les îlots apparaissent comme encastrés dans le substrat d'argent et la hauteur apparente est de 0Å. Ceci peut être considéré comme un avantage décisif pour la manipulation des nanofils. Ils sont entourés d'atomes d'argent qui sont beaucoup plus réactifs que les terrasses d'argent et les bords des marches. À une polarisation de 1V plus proche de l'état de surface, la hauteur apparente augmente à $0,6$Å, tandis qu'en balayant dans la bande de conduction à 3V, la hauteur apparente de l'îlot est d'environ 4.45Å. Des études antérieures mentionnaient déjà que certains îlots de MgO étaient encastrés dans l'argent en raison de la diffusion des adatomes d'argent à température élevée [40], [58]. D'après nos résultats, nous pouvons conclure, qu'une couverture de 100% du substrat d'argent ne peut pas être atteinte. Les atomes d'Ag, grâce à leur haute mobilité à 670K, flottent toujours au-dessus du MgO et la couverture monocouche maximale est d'environ 80% .

Les propriétés électroniques du film MgO ultramince obtenu par la méthode décrite ci-dessus ont été étudiées par STS, ce qui a révélé un état de surface inoccupé à $1,5$eV, conformément à des valeurs récement publiées [113]. La monocouche de MgO présente une forte caractéristique à $2,65$eV liée à l'état du MgO et un état d'interface à peine visible à $1,7$eV, tandis qu'aucun état occupé n'a été mesuré avant au moins -3eV, ce qui donne lieu à une bande interdite d'au moins $4,7$eV. Ces résultats sont en accord avec des mesures dI/dV précédement rapportées: Une valeur de la bande interdite de 6eV pour un film d'épaisseur de 3ML [40]. De plus, les fonctions de travail locales ont été déterminées par les résonances d'émission de champ (FER) à $\Phi_{MgO} = 2,88$eV et à $\Phi_{Ag} = 4,26$eV, ce qui donne une baisse de $\Delta\Phi = -1,38$eV. Des différents mécanismes sont considérés comme responsables de ce phénomène, comme le transfert de charge entre le film d'oxyde et le métal, le moment dipolaire intrinsèque qui est créé à l'interface et en particulier la compression de la densité électronique du métal lors du dépôt de l'oxyde [121]. Enfin, en plus de ces caractéristiques électroniques pertinentes des films ultraminces de MgO mentionnées ici, telles que la persistance d'une large bande interdite même pour les films monocouches, l'abaissement de la fonction de travail locale en comparaison avec le substrat d'Ag et la réactivité accrue des films par rapport au MgO bulk, une autre propriété importante des films ultraminces de MgO a été signalée: Leur remarquable efficacité de découplage, permettant toujours le transfert de charge entre le substrat et les molécules adsorbées via un tunneling électronique. L'extension spatiale des états moléculaires était donc directement accessible par l'imagerie STM [131].

7.3 Effet de la lumière UV sur la synthèse du poly-para-phénylène - une étude en dépendance de la température

Afin d'obtenir des fils de 1D, deux précurseurs différents ont été choisis, en premier, les précurseurs les plus simples que l'on puisse trouver, consistant en trois cycles phényles fonctionnalisés par deux halogènes en position *para*. Selon le choix de l'halogene on peut

distinguer entre le dibromo-p-terphényle (DBTP) et le diiodo-p-terphényle (DITP). Ils ont été utilisés dans ce travail comme précurseurs modèles pour comprendre les différentes étapes de la réaction et pour déterminer l'influence des paramètres contrôlables, tels que la température du substrat pendant le dépôt, la vitesse de dépôt, la température de recuit, etc. L'intérêt de cette première étude sur ces précurseurs modèles était aussi de déterminer l'influence de l'exposition à la lumière sur la réaction d'Ullmann, puisque l'objectif final était de synthétiser des fils 1D sur des couches isolantes de MgO. Ici les résultats principaux sont resumés, qui sont présentés plus en détail dans § 4 ("UV-light effect on poly-para-phenylene synthesis").

7.3.1 Étude des molécules uniques

Déposées sur le substrat Ag(100) maintenu à 5K (voir le montage expérimental § 2.3.1.4), les molécules uniques ont pu être identifiées sans ambiguïté dans les images STM. Elles ont été déposées dans leur architecture intacte et la déshalogénation à l'intérieur du creuset a pu être écartée. Les atomes d'iode encore attachés apparaissent comme un élément volumineux à chaque extrémité de la molécule. La spectroscopie dI/dV enregistrée au centre de la molécule montre un état vide à $1,9$eV et un état occupé autour de $-1,8$eV. En conséquence, l'imagerie STM à courant constant à une polarisation de $1,9$V produit une molécule gonflée gardant à peu près la même longueur, mais affichant une hauteur apparente beaucoup plus grande que à une polarisation plus basse. Les atomes d'iode apparaissent maintenant plus bas que la partie organique. Cet état résonnant à $1,9$eV a été utilisé comme empreinte du groupe $(Ph)_3$ pour le localiser correctement dans la phase organométallique. En plaçant la pointe du STM au-dessus de l'un des iodes et en appliquant une impulsion de polarisation à $2,3$V pendant 300ms, on obtient un clivage contrôlé de la liaison avec fidélité spatiale. La valeur de $2,3$eV est comparable à l'énergie de dissociation de la liaison C-I rapportée de 209kJ/mol ($2,16$eV). Après le clivage de la liaison, le groupe terphénylène reste fortement lié à la surface du métal. La même expérience a été menée avec les précurseurs du DBTP, où les molécules intactes étaient moins fortement liées au substrat que le DITP. Le clivage de la liaison C-Br a pu être réalisé de manière contrôlée par des impulsions de polarisation de la pointe STM à $2,9$V, à comparer avec l'énergie de dissociation de la liaison C-Br rapportée de 280kJ/mol ($2,9$eV). Les manipulations des espèces déshalogénées pour former des dimères ont échoué, ce qui tend à prouver que les espèces réactives réagissent avec le substrat pour saturer leurs liaisons pendantes.

7.3.2 Auto-assemblage moléculaire piloté par des liaisons halogènes

Les liaisons halogènes sont connues pour être relativement fortes et hautement directionnelles [135]. Lorsqu'un atome d'halogène est lié de manière covalente à un ou plusieurs atomes, sa densité électronique est distribuée de manière anisotrope. Une région de densité électronique plus élevée avec un potentiel électrostatique négatif forme une ceinture orthogonale à la liaison covalente. À l'extrémité, une région de densité électronique plus faible et de potentiel électrostatique positif est créée. Cette région est connue sous le nom

"trou σ". En conséquence à cette redistribution de charge, une région avec un caractère accepteur (nucléophile) et une seconde avec un caractère donneur (électrophile) sont unies dans la même espèce moléculaire [135]. Les liaisons halogènes peuvent être formées avec $X = I, Br, Cl$ ou F comme donneur de liaison. Le donneur d'électrons peut être l'un des atomes électronégatifs $Y = N, O, S, Se$ et des atomes négativement chargés I^-, Br^-, Cl^- ou F^-. Également des interactions telles que $\text{R} - \text{X} \cdots \text{X} - \text{R}$ existent entre la région chargée négative d'un halogène $X = I, Br, Cl$ ou F et le trou σ chargé positive d'un autre. La définition officielle de l'Union internationale de chimie pure et appliquée (UICPA) en 2009 est la suivante: "Une liaison halogène se produit lorsqu'il existe une interaction attractive nette entre une région électrophile associée à un atome d'halogène dans une entité moléculaire et une région nucléophile dans une autre ou la même entité moléculaire".

L'origine de cette distribution de charge est la polarisation de l'atome d'halogène participant à la liaison covalente. Par conséquent, la force de la liaison halogène varie en fonction du caractère positif du trou σ et augmente avec la capacité de polarisation de l'atome d'halogène en tant qu'atome donneur de liaison. Cette dernière est liée à son électronégativité, qui descend dans l'ordre $F < Cl < Br < I$. La capacité d'un composé se portant comme donneur de liaison halogène peut donc être facilement ajustée en choisissant l'atome d'halogène le plus approprié. Une gamme des énergies d'interaction assez large peut ainsi être atteinte, notamment en remplaçant un atome d'iode par un atome de brome ou un atome de chlore.

Lors du dépôt sur Ag(100) maintenu à $T = 78$K, le DITP forme des îlots auto-assemblés stabilisés par des liaisons halogènes, ce qui indique qu'à cette température, la diffusion moléculaire est suffisamment élevée pour permettre le réarrangement sur la surface. L'auto-assemblage n'a pas lieu spontanément, mais il est induit par la tension appliqué sur la pointe lors du balayage avec un seuil de 300mV. La dépendance de l'application de cette tension minimale pour la formation de l'auto-assemblage pourrait être liée à une résonance d'un état électronique situé au niveau des atomes de brome. La structure ainsi formée a un ordre carré étendu sur l'ensemble des terrasses avec des défauts auto-réparables, qui s'évoluent avec le temps en scannant. Une structure alternative, avec des molécules alignées en parallèle était trouvé aussi. Une fois créé, l'arrangement moléculaire est caractérisé d'une certaine stabilité, puisqu'il reste le même, lorsque la tension de balayage est abaissée en dessous du seuil.

Nous avons trouvé que l'assemblage carré consiste des noeux de 4 molécules, dont les atomes d'iode se font face avec un angle proche de 90° entre les axes des molécules. Cette structure correspond à des liaisons halogènes décrites précédement, où une zone d'appauvrissement de charge dans l'atom de iode à l'extrémité d'une molécule est dirigée vers la région négativement chargée d'un atome d'iode d'une autre molécule. En outre, cette assemblage moléculaire est aussi stabilisé par des liaisons H-I entre un atome d'iode d'une molécule et un atome d'hydrogène de la molécule voisine. Les longueurs de liaison ont été mesurées à 0, 45nm pour les liaisons I-I et à 0, 36nm pour les liaisons I-H, ce qui est plutôt long par rapport à la longueur attendue par les calculs DFT [137] et également par rapport aux valeurs expérimentales rapportées sur des différentes surfaces [138], [139].

La cause de cette extension des liaisons pourrait être un affaiblissent de ces dernières par le substrat sous-jacent, soit en ajoutant des contraintes géométriques, soit en modifiant la distribution des charges électroniques au sein des molécules. En outre, la distance entre les molécules et l'angle entre ces axes sont le résultat d'une compétition entre les forces résultantes des liaisons I-I et H-I, qui s'influencent donc mutuellement, comme rapporté par Chung *et al.* concernant les liaisons Br-Br et Br-H [138]. Le deuxième arrangement (minoritaire) observé d'une structure en mure de briques a une densité d'emballage plus élevée que l'arrangement carré. Ce type d'arrangement était également rapporté pour le 4,4"-dibromo-p-quaterphényle (DBQP) sur Au(111) à une couverture plus élevée [140].

7.3.3 De l'intermédiaire organométallique au polymère

L'un des polymères les plus simples pouvant être obtenus par synthèse sur surface est le poly-*para*-phénylène (PPP), qui peut être considéré comme le nanoruban de graphène (GNR) le plus étroit. Il est considéré depuis longtemps comme un prototype de semi-conducteur organique parmi les polymères conjugués. Sous forme neutre, le PPP est un isolant, qui peut être dopé pour augmenter sa conductivité. Ses propriétés mécaniques, sa faible densité et sa grande stabilité vis-à-vis de la température, de l'exposition à l'oxygène et de l'humidité font du PPP un candidat prometteur pour l'électronique organique [143].

Les précurseurs DITP et DBTP ont été déposés sur la surface d'Ag(100) maintenue à $T = 300K$. Les barrières énergétiques à franchir pour les différentes étapes de la reaction ont été calculées par DFT par H. Tang au CEMES et pourraient bien expliquer les résultats expérimentaux, comme la diffusion des molécules sur la surface et la dépendance de la réaction de la température. À température ambiante ($T = 300K$), les liaisons C-Br restent intactes, ce qui donne le même ordre carré induit par la polarisation de la pointe que celui observé après le dépôt à $T = 78K$. L'exposition à la lumière UV à $T = 300K$ ou le recuit à $T = 340K$ sans lumière provoquent la débromination. Pour souligner une différence entre les précurseurs DITP et DBTP, les liaisons C-I se dissocient déjà spontanément à température ambiante sans irradiation par la lumière UV. Les radicaux ainsi créés avec des liaisons C insaturées forment un intermédiaire organométallique (OGM) en captant les adatomes du substrat, qui proviennet soit des sites de bord de marche faiblement coordonnés, soit aussi du réseau. Les chaînes ainsi formées par l'alternance de groupes terphényles $(PH)_3$ et des atomes d'Ag sont alignées le long des directions cristallographiques principales $< 100 >$ et $< 010 >$ du substrat, ce qui est également confirmé par les calculs DFT. En raison d'un effet de charge, les atomes d'Ag dans la structure OGM sont très souvent entourés d'atomes d'halogène. L'écart entre la longueur de la molécule et les paramètres du réseau du substrat créent des contraintes, car les atomes d'Ag de l'organometallique ont l'intention de s'adsorber à des positions spécifiques du réseau, favorisées sur le plan énergétique. Dans des longues chaînes moléculaires en résultent des dislocations ou des ruptures de chaîne, pour réduire cette contrainte et permettre la relocalisation des atomes d'Ag et de $(PH)_3$.

L'étape suivante de la réaction d'Ullmann consiste à éliminer les ponts d'argent en chauffant à $T = 473K$, ce qui donne lieu à des oligomères courts, toujours alternés par des atomes d'Ag. Enfin, dans la dernière étape, le couplage d'Ullmann est complet. Des fils de PPP séparés par des atomes d'halogène étaient obtenus en chauffant à $T = 523K$. Il est utile de mentionner que pour cette étape il est nécessaire de cliver la liaison de coordination Ag-C, ce qui a été montré par des calculs DFT d'être énergétiquement beaucoup plus cher que l'attachment des atomes d'Ag aux diradicaux et ce qui explique la température élevée nécessaire pour cette étape. Cependant, le couplage C-C directe après la formation du diradical p-terphényle, sans passer par l'état intermédiaire, est probablement empêché par sa barrière de diffusion assez élevée d'environ $1,98eV$.

Afin de comprendre, quels sont les paramètres qui régissent la réaction et l'effet de l'exposition aux UV sur les différentes étapes de la formation du PPP, nous avons réalisé une étude détaillée concernant les conditions expérimentales, c'est-à-dire la température et la durée de recuit et l'exposition aux UV. Les résultats principaux sont résumés dans le tableau ci-dessous (table 7.1). Nous avons remarqué que l'utilisation des UV dans notre cas permet d'abaisser la température de réaction de 50K, alors que la durée du recuit n'influence pas le résultat.

	T	RT	373K	423K	473K	523K
(100)	UV	OGM	OGM	Oligomers + PPP	PPP	
	No UV	WM	OGM	OGM	Oligomers + PPP	PPP
(111)	UV	OGM	PPP			
	No UV	OGM	Oligomers	PPP		

Table 7.1   Vue synthétique des résultats obtenus sur Ag(100) et Ag(111) à différentes températures de recuit avec et sans exposition à la lumière UV. WM signifie WindMill (auto-assemblage piloté par liaison halogène), OGM intermédiaire organométallique et PPP désigne le poly-para-phénylène, c'est-à-dire le couplage C-C achevé. Comme on peut le voir directement dans ce tableau, les différentes étapes de la réaction se sont produites à une température abaissée de $T = 50K$, lorsqu'une combinaison de lumière UV et de température a été utilisée.

L'Ag(111) est connu d'être plus réactif que l'Ag(100). Par conséquent, comme indiqué dans le tableau 7.1, les étapes de température de réaction se sont avérées plus basses que celles sur l'Ag(100). L'interaction avec le métal semble être assez faible, puisque contrairement aux fils d'OGM obtenus sur Ag(100), les OGM sur Ag(111) ne sont plus alignés avec les axes cristallographiques principaux du substrat mais ils forment plutôt des boucles commençant et se terminant aux bords des marches. Ici, le changement drastique observé sur les fils d'OGM tels que formés spontanément par le dépôt de DITP à $T = 300K$ et après 3 heures d'irradiation UV à $T = 300K$ est remarquable, où on les trouve alignés en parallèle. Les PPP ont été obtenus à $T = 373K$ en utilisant l'assistance de la lumière UV et à $T = 423K$ sans lumière.

L'objectif final de ce travail était de synthétiser ces fils $1D$ sur des couches isolantes de MgO. La même expérience a été donc réalisée sur des îlots de MgO cultivés sur une surface d'Ag(100). Des grands et plats îlots de MgO couvrants au moins 50% du métal ont été déposés selon les paramètres de croissance déterminés dans § 3. Ensuite, les précurseurs

de DBTP ont été déposés sur le substrat maintenu à basse température pour éviter la diffusion, puis le tout était recuit à 300K à l'assistance de lumière UV pendant 11 heures. Les fils d'OGM étaient observés uniquement sur la partie du substrat non couverte par le MgO, alors que tous les atomes de brome étaient trouvés sur les îlots de MgO. Un second dépôt du DBTP afin de saturer la surface d'Ag n'augmentait pas la densité du OGM. Quelques espèces un peu plus grandes que Br étaient trouvées parmi les atomes de Br, qui pourraient eventuellement être attribuées à des diradicaux non réagis de p-TP piégés sur la surface de MgO, mais aucun PPP n'était formé directement sur la surface isolante. Les tentatives de manipulation de l'OGM et des PPP formés sur la surface métallique pour les faire passer par une "porte" entre les atomes environnants des îlots de MgO étaient réalisées sans succès, ce qui confirme la haute énergie d'adsorption de l'OGM et du PPP sur Ag(100).

7.3.4 Effet de la lumière UV sur la réaction Ullmann

Un certain nombre de conclusions peut être tiré de ces études. L'utilisation de la lumière UV en combinaison avec la température de recuit permet le clivage de la liaison C-Br à $T = 300$K. De plus, l'activité catalytique du substrat Ag(100) est améliorée et devient similaire à celle du Cu(111). A l'aide des UV la température de réaction pour obtenir des OGM, des oligomères et des PPP a été abaissée de 50K, ce qui pourrait être appliqué à d'autres systèmes avec des molécules plus grandes ou plus fragiles, qui ne supporteraient pas un recuit à haute température. En outre, nous avons observé que, grâce à la lumière UV, l'ordre des OGM a été amélioré dans le cas du DBTP sur Ag(111). Des études précédentes ont démontré que la première étape d'activation concernant le clivage de la liaison C-X pouvait se faire par exposition à la lumière UV. Ici, nous avons utilisé la lumière UV combinée à la température à chaque étape de la réaction en bénéficiant des conditions plus douces. Cette stratégie permet également de découpler l'étape de diffusion (activée par la température) du clivage de la liaison.

Les mécanismes possibles sous-jacents des processus photoinduits ont été présentés dans § 2.2.4. À partir de nos résultats, une excitation directe de l'adsorbat peut être facilement exclue. L'effet de l'exposition aux UV devrait être dû plutôt à une excitation médiée par le substrat. En particulier, la génération de porteurs chauds induite par des plasmons et le transfert d'électrons chauds dans l'adsorbat devraient être en jeu, puisque l'activité catalytique du substrat est clairement améliorée. En ce qui concerne les tentatives de réaliser un couplage d'Ullmann direct sur MgO par excitation par lumière UV, plusieurs facteurs limitants ont été identifiés, tels que le coefficient de diffusion très élevé des précurseurs DBTP et DITP sur cette surface favorisant leur transfert vers la partie métallique non couverte de l'Ag(100) et la forte énergie d'adsorption de l'OGM et du PPP sur le métal empêchant leur manipulation vers les îlots isolants.

7.4 synthèse sur des surfaces isolantes

Dans § 5 la synthèse sur surface a été présentée en détail à partir de deux complexes de coordination halogénés, dérivés des ligands salen et salophen. Ils ont été utilisés comme précurseurs sur des surfaces d'Ag(100), Ag(111) et MgO. Ces complexes, synthétisés au CEMES par Andrej Jancarik de, ont été spécialement conçus, afin d'obtenir un squelette plus rigide. Deux complexes bromés ont été étudiés : un avec Cu comme ion central (type Cu-salen) et le second avec Ni (type Ni-salen). Les espèces métalliques sont reliées par des liaisons de coordination à 2 N et 2 O. Ici les résulltats principaux sont résumés.

Grâce à leur grande flexibilité et à leur polyvalence, les ligands salen ((N,N-bis(salicylidène) éthylènediamine) et salophen ((N,N-bis(salicylidène) phénylènediamine) sont largement utilisés en chimie de coordination pour former des complexes avec des atomes métalliques, ce qui donne lieu à un large éventail de propriétés magnétiques, électroniques et catalytiques [160]. Grâce à l'énorme polyvalence des substituants qui peuvent être placés sur les cycles phénoliques et le pont diamine, ils sont des candidats potentiels pour être utilisés comme des blocs de construction pour l'auto-assemblage moléculaire et les architectures supramoléculaires. Jusqu'à présent, seules quelques études STM ont été rapportées sur ces complexes.

7.4.1 Précurseurs de type Cu-salen

Les complexes de type Cu-salen ont été déposés sur la surface Ag(100) à $T = 5K$, afin d'obtenir un aperçu de l'intégrité des molécules uniques, de leur taille apparente et de leurs propriétés électroniques. Différentes espèces ont été identifiées sur la surface, comme un complexe bromé intact présentant une forme de C et un ligand tourné sans ion métallique présentant une forme de S. Une espèce en forme de V pouvait être attribuée à un ligand non-tourné sans l'ion métallique central. Une série d'images STM a été enregistrée après d'un recuit à différentes températures favorisant l'auto-assemblage. À une température de $T = 300K$, des régions désordonnées correspondant à un mélange de S, de V et de C, ainsi que des régions ordonnées ne contenant que des espèces en forme de S étaient trouvées. En montant la température du recuit ($T \geq 373K$) les C disparaissaient. Une analyse détaillée des images STM révèlait la présence d'atomes intercalés entre les S, qui peuvent être attribués à des atomes de brome.

Sur la surface de Ag(111) les résultats sont similaires avec le même mélange des 3 espèces qui était trouvé sur la surface de Ag(100). A température ambiante elles s'agglomèrent. Les zones contenantes les 3 espèces mélangées se trouvent désordonnées sans aucune structure périodique. Cependant, les espèces séparées s'assemblent dans un motif régulier, dans le cas des molécules intactes avec une forte influence du substrat sous-jacent avec une symétrie hexagonale de la reconstruction formée. Malgré des auto-assemblages de haute symmetrie trouvés sur des grandes surfaces, un résultat essentiel de cette étude doit être formulé, qu'aucune réaction de couplage d'Ullmann n'a eu lieu. Le fait qu'aucun atome de brome n'ait été trouvé jusqu'a un recuit à $T = RT$, pourrait signifier, qu'à cette température les liaisons C-Br étaient encore intactes, les Br encore attachés à la molécule, même après d'avoir perdu l'ion central. Dans ce cas là, l'énergie d'activation du couplage

d'Ullmann, le clivage de la liaison C-Br, serait supérieure à l'énergie de la liaison de coordination du Cu, ce qui rendrait impossible une réaction de couplage entre des molécules intactes. Les liaisons de coordination du Cu se briseraient toujours avant l'activation de la réaction de couplage. Après un recuit supplémentaire au-dessus de $T = 370K$, toutes les molécules avaient perdu leur ion central. Des espèces en forme de S (la plupart) et en forme de V étaient trouvées sur la surface, organisées dans des reconstructions auto-assemblées de grande surface. Cette fois les atomes de brome clivés étaient clairement visibles sur le scan STM. Différent à des molécules intactes, les reconstructions très régulières des molécules cassées ne montrent pas de symétrie hexagonale, ce qui indique que la géométrie de ces reconstructions est plutôt régie par des interactions intermoléculaires que par des influences du substrat. Même si les atomes de brome ont apparemment été clivés pendant le recuit, aucune réaction de couplage d'Ullmann n'a eu lieu.

Les reconstructions présentes sur la surface changent avec la température de recuit. Après un recuit à $T = 420K$ finalement, eventuellement des dimères étaient trouvés, ce qui est plutôt surprenant à cette température. Un coup d'oeil sur un modèle calculé de la molécule sous forme de gaz peut nous aider à comprendre mieux les réactions ayant lieu. Il montre que la molécule n'est pas plane, mais que les bras sont orientés dans une direction déviée du plan moléculaire. Cette structure $3D$ évite l'effet stérique, lorsque les molécules se rapprochent les unes des autres, ce qui permet d'effectuer le couplage Ullmann. Les ligands sans atome central de Cu ont par contre adapté une géométrie plane. Il est probable qu'une réaction de couplage entre plusieurs molécules ne soit plus possible, ce qui expliquerait pourquoi aucune structure polymérisée n'a été observée après un recuit élevé à $T = 370K$. La situation changerait, si la structure $3D$ était récupérée par une nouvelle coordination avec un atome d'Ag du substrat remplacant les atomes de Cu perdus. Cela conduirait à nouveau à des espèces en forme de C, conforme avec la forme des molécules visible dans le scan STM. Cette réaction nécessiterait de l'énergie, ce qui, en comparaison avec les autres reconstructions trouvées avant, expliquerait la température de recuit plus élevée, nécessaire pour former cette reconstruction et pourquoi après un recuit à $T = 420K$ des dimères seraient finalement créés. Surement un examen plus approfondi serait nécessaire pour confirmer cette hypothèse. Tout aussi surprenant est un autre type de reconstruction contenant des paires de molécules du type S, qui est apparu après un recuit à $T = 530K$. La température de recuit serait suffisament élevée, que ces groupes "tandem" soient polymérisés par déshydrogénation.

En fin de compte, pour surmonter les difficultés rencontrées dans cette étude, différentes stratégies peuvent être suivies: (1) Un ion central plus fortement lié, comme Co, Ni ou Zn, peut être utilisé dans le but de que la décomposition ait lieu à une température plus élevée que la réaction de couplage. (2) Dans le même but, des précurseurs avec des autres halogènes comme substituants, par exemple iode, peuvent être utilisés, diminuant la température d'activation. (3) La décomposition peut être évitée par le choix du substrat, vu qu'un substrat isolant a une activité plus faible. Malheureusement il y a également moins d'activité catalytique sur cette surface pour exciter la réaction de couplage, un problème qui peut être résolu en utilisant la lumière UV. (4) L'utilisation de la lumière

UV abaisse la température de réaction et permet une activité catalytique sur des films minces isolants. (5) Enfin, une stratégie inverse peut être suivie en utilisant des molécules sans ion central et en les métallisant sur le substrat, une fois que la réaction de couplage d'Ullmann ait eu lieu. Il est donc nécessaire de déposer séparément sur le substrat le squelette de la molécule et les atomes métalliques.

7.4.2 Précurseurs de type Ni-salen

Afin d'éviter la même fragmentation que celle subie par les précurseurs de type Cu-salen sur l'Ag(100) et l'Ag(111), un second type de précurseur basé sur un atom central de Ni a été synthétisé au CEMES par Andrej Jancarik. Il a été déposé sur le substrat d'Ag(100) préparé avec des îlots de MgO cultivés dessus et maintenu à $T = 300K$ pendant le dépôt. Un recuit subséquent à $T = 373K$ accompagné de lumière UV a été effectué pendant 16 heures. Les molécules s'adsorbaient préférentiellement sur le MgO plutôt que sur les parties non couvertes du métal, ce qui nous permet de conclure qu'elles étaient encore intactes après le dépôt (Ni toujours présent), en vu à l'interaction attendue entre l'atom central polarisé avec le MgO. En évaluant leur apparence dans le scan STM, elles devraient être fortement déformés sur la surface. La forte influence du substrat s'est également manifestée par le fait que les molécules étaient trouvées dans un auto-assemblage aligné en doubles rangées, gouverné par le registre avec le substrat le long de la direction <110> ou <1 − 10> du MgO. Les forces intermoléculaires qui stabilisent la structure devraient être des forces de Van der Waals. Des calculs DFT pronostiquent une forte distorsion lors d'une adsorption du Ni au-dessus de l'oxygène du MgO, qui est attendu pour des raisons électrostatiques. L'atome de Ni pointe vers un oxygène du substrat et les halogènes vers le haut. Le fait que la liaison substituée par un halogène soit dirigée vers le haut empêche tout couplage Ullmann en raison de la longue distance entre Br et la surface d'Ag. Même après le recuit à $T = 373K$ avec lumière UV, la débromation n'a pas eu lieu, ce qui indique que ce système ne permet pas d'obtenir un couplage d'Ullmann.

Une autre stratégie a donc été employée, de tenter de polymériser les précurseurs par déshydrogénation. L'échantillon a été recuit à la température élevée de $T = 573K$ pendant 15 minutes. Deux dimères différentes ont été trouvés. Un dimer consiste de deux molécules attachés "dos à dos" donnant lieu à une forme rectangulaire et l'autre avec des molécules un peu décalées l'une de l'autre. La haute efficacité de découplage du MgO (voir § 3.3) permettait d'accéder directement par imagerie STM à l'extension spatiale de l'état électronique de l'adsorbat. La dimérisation a donc été prouvée sans ambiguïté par le changement de la distribution spatiale des états électroniques par rapport aux molécules simples. Les images STM correspondantes se trouvent dans § 5.

Bien que le couplage d'Ullmann n'ait pas été atteint dans ce cas, cette étude pourrait être utilisée comme une preuve de concept pour des réactions chimiques directes sur des films ultraminces de MgO, ce qui, à notre connaissance, n'a jamais été rapporté avant. En concevant soigneusement des précurseurs spécifiques, des autres réactions chimiques pourraient être imaginées sur cette surface.

List of Tables

List of Figures

Bibliography

[1] K. S. Mali and S. De Feyter: "Principles of molecular assemblies leading to molecular nanostructures". In *Phil Trans R Soc A* **371**. DOI: `10.1098/rsta.2012.0304` (2013) (cit. on pp. 3, 4).

[2] A. A. Ahmad Zebari, M. Kolmer, and J. S. Prauzner-Bechcicki: "STM tip-assisted engineering of molecular nano-structures: PTCDA islands on Ge(001):H surfaces". In *Beilstein J. Nanotechnol* **4**, 927–932. DOI: `10.3762/bjnano.4.104` (2013) (cit. on p. 5).

[3] A. Kahn, N. Koch, and W. Gao: "Electronic Structure and Electrical Properties of Interfaces between Metals and π-Conjugated Molecular Films". In *J Polym Sci Part B: Polym Phys* **41**, 2529–2548. DOI: `10.1002/polb.10642` (2003) (cit. on pp. 5, 88).

[4] N. Koch, A. Kahn, J. Ghijsen, J.-J. Pireaux, J. Schwartz, R.L. Johnson, and A. Elschner: "Conjugated organic molecules on metal versus polymer electrodes: Demonstration of a key energy level alignment mechanism". In *Appl.Phys.Letters* **82**, 70–72. DOI: `10.1063/1.1532102` (2003) (cit. on p. 6).

[5] C. Nacci, A. Viertel, S. Hecht, and L. Gill: "Covalent Assembly and Characterization of Nonsymmetrical Single-Molecule Nodes". In *Angew.Chem. Int. Ed.* **55**, 13724–13728. DOI: `10.1002/anie.201605421` (2016) (cit. on p. 7).

[6] B. Cirera, Y.-Q. Zhang, J. Björk, S. Klyatskaya, Z. Chen, M. Ruben, J.V. Barth, and F. Klappenberger: "Synthesis of Extended Graphdiyne Wires by Vicinal Surface Templating". In *Nano Lett.* **14**, 1891–1897. DOI: `10.1021/nl4046747` (2014) (cit. on p. 7).

[7] D.G. Oteyza et al.: "Direct Imaging of Covalent Bond Structure in Single-Molecule Chemical Reactions". In *Science* **340**, 1434–1437. DOI: `10.1126/science.1238187` (2013) (cit. on p. 7).

[8] M. Treier, C.A. Pignedoli, T. Laino, R. Rieger, K. Müllen, D. Passerone, and R. Fasel: "Surface-Assisted Cyclodehydrogenation Provides a Synthetic Route towards Easily Processable and Chemically Tailored Nanographenes". In *Nat. Chem.* **3**, 61–67. DOI: `10.1038/nchem.891` (2011) (cit. on p. 7).

[9] A.C. Aragonès, N.L. Haworth, N. Darwish, S. Ciampi, N.J. Bloomfield, G.G. Wallace, I. Diez-Perez, and M.L. Coote: "Electrostatic Catalysis of a Diels–Alder Reaction". In *Nature* **531**, 88–91. DOI: `10.1038/nature16989` (2016) (cit. on p. 7).

[10] Z. Gong et al.: "Structural Variation in Surface-Supported Synthesis by Adjusting the Stoichiometric Ratio of the Reactants". In *ACS Nano* **10**, 4228–4235. DOI: `10.1021/acsnano.5b07601` (2016) (cit. on p. 7).

[11] X.H. Liu, C.-Z. Guan, S.-Y. Ding, W. Wang, H.-J. Yan, D. Wang, and L.-J. Wan: "On-Surface Synthesis of Single-Layered Two-Dimensional Covalent Organic Frameworks via Solid–Vapor Interface Reactions". In *J.Am.Chem.Soc.* **135**, 10470–10474. DOI: `10.1021/ja403464h` (2013) (cit. on p. 7).

[12] M. Piantek, D. Serrate, M. Moro-Lagares, P. Algarabel, J.I. Pascual, and M.R. Ibarra: "Manganese Phthalocyanine Derivatives Synthesized by On-Surface Cyclotetramerization". In *J.Phys.Chem.C.* **118**, 7895–7899. DOI: `10.1021/jp506652j` (2014) (cit. on p. 7).

[13] J. Cai et al.: "Atomically Precise Bottom-up Fabrication of Graphene Nanoribbons". In *Nature* **466**, 470–473. DOI: `10.1038/nature09211` (2010) (cit. on pp. 9, 12).

[14] M. Liu, S. Chen, T. Li, J. Wang, and D. Zhong: "Tuning On-Surface Synthesis of Graphene Nanoribbons by Noncovalent Intermolecular Interactions". In *J. Phys. Chem. C* **122**, 24415–24420. DOI: `10.1021/acs.jpcc.8b07618` (2018) (cit. on p. 9).

[15] R. Zuzak, R. Dorel, M. Kolmer, M. Szymonski, S. Godlewski, and A. M. Echavarren: "Higher Acenes by On-Surface Dehydrogenation: From Heptacene to Undecacene". In *Angew. Chem. Int. Ed* **57**, 10500–10505. DOI: `10.1002/anie.201802040` (2018) (cit. on p. 9).

[16] T. Wang and J. Zhu: "Confined On-Surface Organic Synthesis: Strategies and Mechanisms". In *Surf. Sci. Rep.* **74**, 97–140. DOI: `10.1016/j.surfrep.2019.05.001` (2019) (cit. on p. 9).

[17] S. Clair and D.G. Oteyza: "Controlling a Chemical Coupling Reaction on a Surface: Tools and Strategies for On-Surface Synthesis". In *Chem. Rev.* **119**, 4717–4776. DOI: `10.1021/acs.chemrev.8b00601` (2019) (cit. on pp. 9, 11, 12, 88).

[18] Q. Shen, H.-Y. Gao, and H. Fuchs: "Frontiers of on-surface synthesis: From principles to applications". In *nanotoday* **13**, 77–96. DOI: `10.1016/j.nantod.2017.02.007` (2017) (cit. on pp. 9, 11, 88).

[19] Q. Sun, R. Zhang, J. Qiu, R. Liu, and W. Xu: "On-Surface Synthesis of Carbon Nanostructures". In *Adv. Mater.* **30**, 1705630. DOI: `10.1002/adma.201705630` (2018) (cit. on p. 9).

[20] M. Di Giovannantonio and G. Contini: "Reversibility and Intermediate Steps as Key Tools for the Growth of Extended Ordered Polymers via On-Surface Synthesis". In *J. Phys. Condens. Matter* **30**, 093001. DOI: `10.1088/1361-648X/aaa8cb` (2018) (cit. on p. 9).

[21] L. Dong, P. N. Liu, and N. Lin: "Surface-Activated Coupling Reactions Confined on a Surface". In *Acc. Chem. Res.* **48**, 2765–2774. DOI: `10.1021/acs.accounts.5b00160` (2015) (cit. on p. 9).

[22] J. Björk and F. Hanke: "Towards Design Rules for Covalent Nanostructures on Metal Surfaces". In *Chem. - Eur. J.* **20**, 928–934. DOI: `10.1002/chem.201303559` (2014) (cit. on p. 9).

[23] Q. Fan, J. Dai, T. Wang, J. Kuttner, G. Hilt, J.M. Gottfried, and J. Zhu: "Confined Synthesis of Organometallic Chains and Macrocycles by Cu-O Surface Templating". In *ACS Nano* **10**, 3747–3754. DOI: `10.1021/acsnano.6b00366` (2016) (cit. on p. 13).

[24] M.V. Makarova, Y. Okawa, E. Verveniotis, K. Watanabe, T. Taniguchi, C. Joachim, and M. Aono: "Self-Assembled Diacetylene Molecular Wire Polymerization on an Insulating Hexagonal Boron Nitride (0001) Surface". In *Nanotechnology* **27**, 395303. DOI: `10.1088/0957-4484/27/39/395303` (2016) (cit. on pp. 14, 88).

[25] A. Richter, V. Haapasilta, C. Venturini, R. Bechstein, A. Gourdon, A.S. Foster, and A. Kühnle: "Diacetylene Polymerization on a Bulk Insulator Surface". In *Phys. Chem. Chem. Phys.* **19**, 15172–15176. DOI: `10.1039/C7CP01526G` (2017) (cit. on pp. 14, 88).

[26] M. Kittelmann, M. Nimmrich, R. Lindner, A. Gourdon, and A. Kühnle: "Sequential and Site-Specific On-Surface Synthesis on a Bulk Insulator". In *ACS Nano* **7**, 5614–5620. DOI: `10.1021/nn402018w` (2013) (cit. on pp. 14, 88).

[27] R. Lindner, P. Rahe, M. Kittelmann, A. Gourdon, R. Bechstein, and A. Kühnle: "Substrate Templating Guides the Photoinduced Reaction of C 60 on Calcite". In *Angew. Chem. Int. Ed.* **53**, 7952–7955. DOI: `10.1002/anie.201309128` (2014) (cit. on pp. 14, 88).

[28] F. Para et al.: "Micrometre-Long Covalent Organic Fibres by Photoinitiated Chain-Growth Radical Polymerization on an Alkali-Halide Surface". In *Nat. Chem.* **10**, 1112–1117. DOI: `10.1038/s41557-018-0120-x` (2018) (cit. on pp. 14, 88).

[29] M. Kolmer, R. Zuzak, A. K. Steiner, L. Zajac, M. Engelund, S. Godlewski, M. Szymonski, and K. Amsharov: "Fluorine-Programmed Nanozipping to Tailored Nanographenes on Rutile TiO 2 Surfaces". In *Surf. Sci.* **363**, 57–60. DOI: `10.1126/science.aav4954` (2019) (cit. on p. 14).

[30] M. Kolmer et al.: "On-Surface Polymerization on a Semiconducting Oxide: Aryl Halide Coupling Controlled by Surface Hydroxyl Groups on Rutile TiO 2 (011)". In *Chem. Commun.* **51**, 11276–11279. DOI: `10.1039/C5CC02989A` (2015) (cit. on p. 14).

[31] P. Olszowski, B. Zapatoczny, J.S. Prauzner-Bechcicki, M. Vilas-Varela, D. Pérez, E. Guitián, D. Peña, and M. Szymonski: "Aryl Halide C–C Coupling on Ge(001):H Surfaces". In *J. Phys. Chem. C* **119**, 27478–27482. DOI: `10.1021/acs.jpcc.5b08883` (2015) (cit. on p. 14).

[32] N. C. Berner, Y. N. Sergeeva, N. N. Sergeeva, M. O. Senge, A. A. Cafolla, and I. T. McGovern: "Intermolecular Dehalogenation Reactions on Passivated Germanium(001)". In *Cond-Mat.* DOI: `ArXiv150506031` (2015) (cit. on p. 14).

[33] F. Eisenhut et al.: "Hexacene Generated on Passivated Silicon". In *Nanoscale* **10**, 12582–12587. DOI: `10.1039/C8NR03422B` (2018) (cit. on p. 14).

[34] C. Morchutt, J. Björk, S. Krotzky, R. Gutzler, and K. Kern: "Covalent Coupling via Dehalogenation on Ni(111) Supported Boron Nitride and Graphene". In *Chem. Commun.* **51**, 2440–2443. DOI: `10.1039/C4CC07107G` (2015) (cit. on p. 14).

[35] N. Pavliček, Z. Majzik, S. Collazos, G. Meyer, D. Pérez, E. Guitián, D. Peña, and L. Gross: "Generation and Characterization of a Meta-Aryne on Cu and NaCl Surfaces". In *ACS Nano* **11**, 10768–10773. DOI: `10.1021/acsnano.7b06137` (2017) (cit. on p. 14).

[36] S. Clair, O. Ourdjini, M. Abel, and L. Porte: "Two-Dimensional Polymer as a Mask for Surface Nanopatterning". In *Adv. Mater.* **24**, 1252–1254. DOI: `10.1002/adma.201200063` (2012) (cit. on p. 14).

[37] Y. Bao et al.: "Substoichiometric Molybdenum Sulfide Phases with Catalytically Active Basal Planes". In *J. Am. Chem. Soc.* **138**, 14121–14128. DOI: `10.1021/jacs.6b09042` (2016) (cit. on p. 14).

[38] M. Lackinger: "Surface-Assisted Ullmann Coupling". In *Chem. Commun.* **53**, 7872–7885. DOI: `10.1039/C7CC03402D` (2017) (cit. on pp. 14–16, 89).

[39] X. Zhou et al.: "On-Surface Synthesis Approach to Preparing One-Dimensional Organometallic and Poly-p-Phenylene Chains". In *Mater. Chem. Front.* **1**, 119–127. DOI: `10.1039/C6QM00142D` (2017) (cit. on pp. 15, 55, 64).

[40] S. Schintke, S. Messerli, M. Pivetta, F. Patthey, L. Libioulle, M. Stengel, A. De Vita, and W.-D. Schneider: "Insulator at the Ultrathin Limit: MgO on Ag(001)". In *Phys. Rev. Lett.* **87**, 276801. DOI: `10.1103/PhysRevLett.87.276801` (2001) (cit. on pp. 17, 34, 35, 41, 42, 44, 91, 93, 95).

[41] S. Schintke and W.-D. Schneider: "Insulators at the Ultrathin Limit: Electronic Structure Studied by Scanning Tunnelling Microscopy and Scanning Tunnelling Spectroscopy". In *J. Phys. Condens. Matter* **16**, R49–R81. DOI: `10.1088/0953-8984/16/4/R02` (2004) (cit. on pp. 17, 33, 34, 91, 93).

[42] S. Yadavalli, M. H. Yang, and C. P. Flynn: "Low-Temperature Growth of MgO by Molecular-Beam Epitaxy". In *Phys. Rev. B* **41**, 7961–7963. DOI: `10.1103/PhysRevB.41.7961` (1990) (cit. on p. 17).

[43] K. Nashimoto, D. K. Fork, and T. H. Geballe: "Epitaxial Growth of MgO on GaAs(001) for Growing Epitaxial BaTiO 3 Thin Films by Pulsed Laser Deposition". In *Appl. Phys. Lett.* **60**, 1199–1201. DOI: `10.1063/1.107404` (1992) (cit. on p. 17).

[44] K.-R. Jeon, C.-Y. Park, and S.-C. Shin: "Epitaxial Growth of MgO and CoFe/MgO on Ge(001) Substrates by Molecular Beam Epitaxy". In *Cryst. Growth Des.* **10**, 1346–1350. DOI: `10.1021/cg901380b` (2010) (cit. on p. 17).

[45] G. X. Miao, J. Y. Chang, M. J. van Veenhuizen, K. Thiel, M. Seibt, G. Eilers, M. Münzenberg, and J. S. Moodera: "Epitaxial Growth of MgO and Fe-MgO-Fe Magnetic Tunnel Junctions on (100)-Si by Molecular Beam Epitaxy". In *Appl. Phys. Lett.* **93**, 142511. DOI: `10.1063/1.2999633` (2008) (cit. on p. 17).

[46] M. M. Sung, C. Kim, C. G. Kim, and Y. Kim: "Epitaxial Growth of MgO Films on Si(111) by Metal Organic Chemical Vapor Deposition". In *J. Cryst. Growth* **210**, 651–654. DOI: `10.1016/S0022-0248(99)00847-7` (2000) (cit. on p. 17).

[47] M. C. Gallagher, M. S. Fyfield, L. A. Bumm, J. P. Cowin, and S. A. Joyce: "Structure of Ultrathin MgO Films on Mo(001)". In *Thin Solid Films* **445**, 90–95. DOI: 10.1016/j.tsf.2003.09.016 (2003) (cit. on p. 17).

[48] M. C. Gallagher, M. S. Fyfield, J. P. Cowin, and S. A. Joyce: "Imaging Insulating Oxides: Scanning Tunneling Microscopy of Ultrathin MgO Films on Mo(001)". In *Surf. Sci.* **339**, L909–L913. DOI: 10.1016/0039-6028(95)80056-5 (1995) (cit. on p. 17).

[49] J. Wollschläger, D. Erdös, H. Goldbach, R. Höpken, and K. M. Schröder: "Growth of NiO and MgO Films on Ag(100)". In *Thin Solid Films* **400**, 1–8. DOI: 10.1016/S0040-6090(01)01482-1 (2001) (cit. on pp. 17, 33, 34, 92).

[50] M. Kiguchi, T. Goto, K. Saiki, T. Sasaki, Y. Iwasawa, and A. Koma: "Atomic and Electronic Structures of MgO/Ag() Heterointerface". In *Surf. Sci.* **512**, 97–106. DOI: 10.1016/S0039-6028(02)01577-7 (2002) (cit. on pp. 17, 34).

[51] A. Ouvrard, J. Niebauer, A. Ghalgaoui, C. Barth, C. R. Henry, and B. Bourguignon: "Characterization of Thin MgO Films on Ag(001) by Low-Energy Electron Diffraction and Scanning Tunneling Microscopy". In *J. Phys. Chem. C* **115**, 8034–8041. DOI: 10.1021/jp1095823 (2011) (cit. on pp. 17, 34, 35, 93).

[52] C. Giovanardi, A. di Bona, T. S. Moia, S. Valeri, C. Pisani, M. Sgroi, and M. Busso: "Experimental and Theoretical Study of the MgO on Ag() Interface". In *Surf. Sci.* **505**, L209–L214. DOI: 10.1016/S0039-6028(02)01319-5 (2002) (cit. on pp. 17, 34, 38).

[53] J. Pal et al.: "How Growing Conditions and Interfacial Oxygen Affect the Final Morphology of MgO on Ag(100) Films". In *J. Phys. Chem. C* **118**, 26091–26102. DOI: 10.1021/jp507718n (2014) (cit. on pp. 17, 40, 94).

[54] T. König: "Investigation of Defects on MgO Films Grown on Ag(001) - A Combined Dynamic Force and Scanning Tunneling Microscopy Study". In. DOI: 10.14279/DEPOSITONCE-2509 (2010) (cit. on p. 17).

[55] T. König: "Investigation of Defects on MgO Films Grown on Ag(001) - A Combined Dynamic Force and Scanning Tunneling Microscopy Study". Doctoral Thesis. Technische Universität Berlin, Fakultät II - Mathematik und Naturwissenschaften (2010) (cit. on p. 17).

[56] T. Jaouen, S. Tricot, G. Delhaye, B. Lépine, D. Sébilleau, G. Jézéquel, and P. Schieffer: "Layer-Resolved Study of Mg Atom Incorporation at the MgO on Ag (001) Buried Interface". In *Phys. Rev. Lett.* **111**, 027601. DOI: 10.1103/PhysRevLett.111.027601 (2013) (cit. on p. 17).

[57] N. Lopez and S. Valeri: "MgO on Ag (001) Interface Structure and STM Images from First Principles". In *Phys. Rev. B* **70**, 125428. DOI: 10.1103/PhysRevB.70.125428 (2004) (cit. on p. 17).

[58] S. Valeri, S. Altieri, U. del Pennino, A. di Bona, P. Luches, and A. Rota: "Scanning Tunnelling Microscopy of MgO Ultrathin Films on Ag(001)". In *Phys. Rev. B* **65**, 245410. DOI: 10.1103/PhysRevB.65.245410 (2002) (cit. on pp. 17, 34, 41, 42, 95).

[59]   J. Wollschläger, J. Viernow, C. Tegenkamp, D. Erdös, K. M. Schröder, and H. Pfnür: "Stoichiometry and Morphology of MgO Films Grown Reactively on Ag(100)". In *Appl. Surf. Sci.* **142**, 129–134. DOI: `10.1016/S0169-4332(98)00656-4` (1999) (cit. on pp. 17, 34).

[60]   S. Valeri, S. Altieri, A. di Bona, C. Giovanardi, and T. S. Moia: "Structural Study of Thin MgO Layers on Ag(001) Prepared by Either MBE or Sputter Deposition". In *Thin Solid Films* **400**, 16–21. DOI: `10.1016/S0040-6090(01)01486-9` (2001) (cit. on pp. 17, 33).

[61]   J. Wollschläger, D. Erdös, and K.-M. Schröder: "The Formation of Mosaics during the Reactive Growth of MgO Films on Ag(100)". In *Surf. Sci.* **402–404**, 272–276. DOI: `10.1016/S0039-6028(97)00988-6` (1998) (cit. on p. 17).

[62]   M. S. Chen and D. W. Goodman: "Ultrathin, Ordered Oxide Films on Metal Surfaces". In *J. Phys. Condens. Matter* **20**, 264013. DOI: `10.1088/0953-8984/20/26/264013` (2008) (cit. on pp. 17, 33, 34, 91, 93).

[63]   A. Hellman, S. Klacar, and H. Grönbeck: "Low Temperature CO Oxidation over Supported Ultrathin MgO Films". In *J. Am. Chem. Soc.* **131**, 16636–16637. DOI: `10.1021/ja906865f` (2009) (cit. on pp. 17, 91).

[64]   A. Gonchar, T. Risse, H.-J. Freund, L. Giordano, C. Di Valentin, and G. Pacchioni: "Activation of Oxygen on MgO, O2 Radical Ion Formation on Thin, Metal-Supported MgO(001) Films". In *Angew. Chem. Int. Ed.* **50**, 2635–2638. DOI: `10.1002/anie.201005729` (2011) (cit. on pp. 17, 91).

[65]   J. Jung, H.-J. Shin, Y. Kim, and M. Kawai: "State-Selective Dissociation of a Single Water Molecule on an Ultrathin MgO Film". In *Nat. Mater.* **9**, 442–447. DOI: `10.1038/nmat2740` (2010) (cit. on pp. 18, 44, 91).

[66]   H.-J. Shin, J. Jung, K. Motobayashi, S. Yanagisawa, Y. Morikawa, Y. Kim, and M. Kawai: "Controlling Water Dissociation on an Ultrathin MgO Film by Tuning Film Thickness". In *Phys. Rev. B* **82**, 085413. DOI: `10.1103/PhysRevB.82.085413` (2010) (cit. on pp. 18, 44, 91).

[67]   E. Hasselbrink: "Mechanisms in photochemistry on metal surfaces". In *Appl. Surf. Sci.* **79-80**, 34–40. DOI: `10.1016/0169-4332(94)90384-0` (1994) (cit. on pp. 18–20, 92).

[68]   R. Franchy: "Surface and bulk photochemistry of solids". In *Rep. Prog. Phys.* **61**, 691. DOI: `10.1088/0034-4885/61/6/003` (1998) (cit. on pp. 18–20, 92).

[69]   F. Engel, T. Dieterle, F. Hummel, C. Fey, P. Schmelcher, R. Löw, T. Pfau, and F. Meinert: "Precision Spectroscopy of Negative-Ion Resonances in Ultralong-Range Rydberg Molecules". In *Phys. Rev. Lett.* **123**, 073003. DOI: `10.1103/PhysRevLett.123.073003` (2019) (cit. on p. 18).

[70]   E. Illenberger: "Formation and Evolution of Negative Ion Resonances at Surfaces". In *Surf. Sci.* **528**, 67–77. DOI: `10.1016/S0039-6028(02)02612-2` (2003) (cit. on p. 18).

[71] D. C. Marinica, C. Ramseyer, D. Teillet-Billy, and J. P. Gauyacq: "Negative Ion Resonance of a Molecule Adsorbed on a Metal Surface Covered with a Rare Gas Monolayer". In *Surf. Sci.* **600**, 803–814. DOI: 10.1016/j.susc.2005.11.035 (2006) (cit. on p. 18).

[72] P. Tegeder and E. Illenberger: "Evolution of Negative Ion Resonances at Surfaces: Effect of Environment and Orientation". In *J. Phys. Conf. Ser.* **86**, 012007. DOI: 10.1088/1742-6596/86/1/012007 (2007) (cit. on p. 18).

[73] D. Menzel and R. Gomer: "Desorption from Metal Surfaces by Low-Energy Electrons". In *J. Chem. Phys.* **41**, 3311–3328. DOI: 10.1063/1.1725730 (1964) (cit. on pp. 19, 91).

[74] P. A. Redhead: "Interaction of Slow Electrons with Chemisorbed Oxygen". In *Can. J. Phys.* **42**, 886–905. DOI: 10.1139/p64-083 (1964) (cit. on pp. 19, 91).

[75] W. Hoheisel, K. Jungmann, M. Vollmer, R. Weidenauer, and F. Träger: "Desorption Stimulated by Laser-Induced Surface-Plasmon Excitation". In *Phys. Rev. Lett.* **60**, 1649–1652. DOI: 10.1103/PhysRevLett.60.1649. (1988) (cit. on p. 19).

[76] M. Rocca, F. Biggio, and U. Valbusa: "Surface-Plasmon Spectrum of Ag(001) Measured by High-Resolution Angle-Resolved Electron-Energy-Loss Spectroscopy". In *Phys. Rev. B* **42**, 2835–2841. DOI: 10.1103/PhysRevB.42.2835 (1990) (cit. on pp. 20, 92).

[77] M. Kim, M. Lin, J. Son, H. Xu, and J.-M. Nam: "Hot-Electron-Mediated Photochemical Reactions: Principles, Recent Advances, and Challenges". In *Adv. Opt. Mater.* **5**, 1700004. DOI: 10.1002/adom.201700004 (2017) (cit. on pp. 20, 21, 92).

[78] J. Liu et al.: "Plasmonic Hot Electron-Mediated Hydrodehalogenation Kinetics on Nanostructured Ag Electrodes". In *J. Am. Chem. Soc.* **142**, 17489–17498. DOI: 10.1021/jacs.0c07027 (2020) (cit. on pp. 20, 92).

[79] Stratton J. A.: *Electromagnetic Theory.* New York: McGraw-Hill Book Company, Inc. (1941) (cit. on pp. 21, 92).

[80] G. Binnig, H. Rohrer, Ch. Gerber, and E. Weibel: "Tunneling through a controllable vacuum gap". In *Appl. Phys. Lett.* **40**. DOI: 10.1063/1.92999 (1982) (cit. on p. 22).

[81] J. Kügel: "3d-Übergangsmetallphthalocyanin-Moleküle auf Metalloberflächen: Der Einfluss der d-Orbitalbesetzung". Dissertation. Universität Würzburg (2015) (cit. on pp. 22–24).

[82] G. Binnig, H. Rohrer, Ch. Gerber, and E. Weibel: "Surface Studies by Scanning Tunneling Microscopy". In *Phys. Rev. Lett.* **49**, 57–61. DOI: 10.1103/PhysRevLett.49.57 (1982) (cit. on p. 22).

[83] M. Ternes: "Scanning tunneling spectroscopy at the single atom scale". Dissertation. École Polytechnique Fédérale de Lausanne (2006) (cit. on pp. 24–26).

[84] R.M. Feenstra, J.A. Stroscio, J. Tersoff, and A.P. Fein: "Atom-Selective Imaging of GaAs(110) Surface". In *Phys. Rev. Lett.* **58**, 1192–1195. DOI: 10.1103/PhysRevLett.58.1192 (1986) (cit. on p. 24).

[85] N.D. Lang: "Spectroscopy of single atoms in the scanning tunneling microscope". In *Phys. Rev. Lett. B* **34**, 5947–5950. DOI: `10.1103/PhysRevB.34.5947` (1986) (cit. on p. 25).

[86] J. Tersoff and D.R. Hamann: "Theory of the scanning tunneling microscope". In *Phys. Rev. Lett. B* **31**, 805–813. DOI: `10.1103/PhysRevB.31.805` (1985) (cit. on p. 26).

[87] J. Tersoff and D.R. Hamann: "Theory and application for the scanning tunneling microscope". In *Phys. Rev. Lett.* **50**, 1998–2001. DOI: `10.1103/PhysRevLett.50.1998` (1983) (cit. on p. 26).

[88] J. Bardeen: "Tunnelling from a many-particle point of view". In *Phys. Rev. Lett.* **6**, 57–59. DOI: `10.1103/PhysRevLett.6.57` (1961) (cit. on p. 26).

[89] C. J. Chen: "Tunnelling from a many-particle point of view". In *Phys. Rev. Lett.* **65**, 448–451. DOI: `10.1103/PhysRevLett.65.448` (1990) (cit. on p. 26).

[90] INTERREG V-A Spain France Andorra: *Project EFA194/16/TNSI*. 2016-2021 (cit. on pp. 27, 47).

[91] L. Vernisse: "Etude par Microscopie à Effet Tunnel sous Ultra-Vide et à Basse Température de Complexes de Ruthénium". Dissertation. Université Toulouse III Paul Sabatier (2014) (cit. on p. 28).

[92] Vacgen: *Fused Silica Quartz Viewport*. 2020. Product description: `https://vacgen.com/fused-silica-quartz-viewport` (cit. on p. 29).

[93] Oriel: *Oriel Product Training, Spectral Irradiance*. 2020. Product description: `https://www.newport.com/medias/sys_master/images/images/hfb/hdf/8797196451870/Light-Sources.pdf` (cit. on p. 31).

[94] S. Heo, E. Cho, H.-I. Lee, G. S. Park, H. J. Kang, T. Nagatomi, P. Choi, and B.-D. Choi: "Band Gap and Defect States of MgO Thin Films Investigated Using Reflection Electron Energy Loss Spectroscopy". In *AIP Adv.* **5**, 077167. DOI: `10.1063/1.4927547` (2015) (cit. on pp. 33, 44, 92, 93).

[95] S. Valeri, S. Altieri, A. di Bona, P. Luches, C. Giovanardi, and T. S. Moia: "Thickness-Dependent Strain in Epitaxial MgO Layers on Ag(001)". In *Surf. Sci.* **507-510**, 311–317. DOI: `10.1016/S0039-6028(02)01263-3` (2002) (cit. on pp. 33, 34, 92).

[96] G. H. Rosenblatt, M. W. Rowe, G. P. Williams, R. T. Williams, and Y. Chen: "Luminescence of F and F + Centers in Magnesium Oxide". In *Phys. Rev. B* **39**, 10309–10318. DOI: `10.1103/PhysRevB.39.10309` (1989) (cit. on p. 33).

[97] B. Nourozi, A. Aminian, N. Fili, Y. Zangeneh, A. Boochani, and P. Darabi: "The Electronic and Optical Properties of MgO Mono-Layer: Based on GGA-MBJ". In *Results Phys.* **12**, 2038–2043. DOI: `10.1016/j.rinp.2019.02.054` (2019) (cit. on pp. 33, 44, 93).

[98] M. Heyde, M. Sterrer, H.-P. Rust, and H.-J. Freund: "Atomic Resolution on MgO(001) by Atomic Force Microscopy Using a Double Quartz Tuning Fork Sensor at Low-Temperature and Ultrahigh Vacuum". In *Appl. Phys. Lett.* **87**, 083104. DOI: `10.1063/1.2012523` (2005) (cit. on p. 34).

[99] E. Carrasco, M. A. Brown, M. Sterrer, H.-J. Freund, K. Kwapien, M. Sierka, and J. Sauer: "Thickness-Dependent Hydroxylation of MgO(001) Thin Films". In *J. Phys. Chem. C* **114**, 18207–18214. DOI: `10.1021/jp105294e` (2010) (cit. on p. 34).

[100] M. Sterrer, T. Risse, U. Martinez Pozzoni, L. Giordano, M. Heyde, H.-P. Rust, G. Pacchioni, and H.-J. Freund: "Control of the Charge State of Metal Atoms on Thin MgO Films". In *Phys. Rev. Lett.* **98**, 096107. DOI: `10.1103/PhysRevLett.98.096107` (2007) (cit. on p. 34).

[101] M. Sterrer, M. Heyde, M. Novicki, N. Nilius, T. Risse, H.-P. Rust, G. Pacchioni, and H.-J. Freund: "Identification of Color Centers on MgO(001) Thin Films with Scanning Tunneling Microscopy". In *J. Phys. Chem. B* **110**, 46–49. DOI: `10.1021/jp056306f` (2006) (cit. on p. 34).

[102] H.-J. Shin, J. Jung, K. Motobayashi, S. Yanagisawa, Y. Morikawa, Y. Kim, and M. Kawai: "State-Selective Dissociation of a Single Water Molecule on an Ultrathin MgO Film". In *Nat. Mater.* **9**, 442–447. DOI: `10.1038/nmat2740` (2010) (cit. on pp. 34, 45, 84).

[103] Y. Cui, C. Stiehler, N. Nilius, and H.-J. Freund: "Probing the Electronic Properties and Charge State of Gold Nanoparticles on Ultrathin MgO versus Thick Doped CaO Films". In *Phys. Rev. B* **92**, 075444. DOI: `10.1103/PhysRevB.92.075444` (2015) (cit. on pp. 34, 44).

[104] I. K. Robinson and D. J. Tweet: "Surface X-Ray Diffraction". In *Rep. Prog. Phys.* **55**, 599–651. DOI: `10.1088/0034-4885/55/5/002` (1992) (cit. on pp. 36, 37, 94).

[105] E. Vlieg: "ROD: A Program for Surface X-Ray Crystallography". In *J. Appl. Crystallogr.* **33**, 401–405. DOI: `10.1107/S0021889899013655` (2000) (cit. on pp. 36, 94).

[106] E. Vlieg, J. F. Van Der Veen, S. J. Gurman, C. Norris, and J. E. Macdonald: "X-Ray Diffraction from Rough, Relaxed and Reconstructed Surfaces". In *Surf. Sci.* **210**, 4301–321. DOI: `10.1016/0039-6028(89)90598-0` (1989) (cit. on p. 36).

[107] I. K. Robinson: "Handbook on Synchrotron Radiation". In **3**, 221 (1991) (cit. on p. 36).

[108] M. Sgroi, C. Pisani, and M. Busso: "Ab Initio Density Functional Simulation of Structural and Electronic Properties of MgO Ultra-Thin Adlayers on the (001) Ag Surface". In *Thin Solid Films* **400**, 64–70. DOI: `10.1016/S0040-6090(01)01450-X` (2001) (cit. on pp. 37, 44).

[109] H. L. Meyerheim, S. Pflanz, R. Schuster, and I. K. Robinson: "Surface X-Ray Diffraction on Clean and Cs-Covered Ag(001)". In *Z. Für Krist. - Cryst. Mater.* **212**. DOI: `10.1524/zkri.1997.212.5.327` (1997) (cit. on p. 37).

[110] S. Baumann, I. G. Rau, S. Loth, C. P. Lutz, and A. J. Heinrich: "Measuring the Three-Dimensional Structure of Ultrathin Insulating Films at the Atomic Scale". In *ACS Nano* **8**, 1739–1744. DOI: `10.1021/nn4061034` (2014) (cit. on p. 37).

[111] G. Cabailh, J. Goniakowski, C. Noguera, J. Jupille, R. Lazzari, J. Li, P. Lagarde, and N. Trcera: "Understanding Nanoscale Effects in Oxide/Metal Heteroepitaxy". In *Phys. Rev. Mater.* **3**, 046001. DOI: `10.1103/PhysRevMaterials.3.046001` (2019) (cit. on p. 38).

[112] P. Luches, S. D'Addato, S. Valeri, E. Groppo, C. Prestipino, C. Lamberti, and F. Boscherini: "X-Ray Absorption Study at the Mg and O K Edges of Ultrathin MgO Epilayers on Ag(001)". In *Phys. Rev. B* **69**, 045412. DOI: `10.1103/PhysRevB.69.045412` (2004) (cit. on p. 38).

[113] B. Kim, S. Hong, R. Liu, and D. W. Lynch: "Angle-Resolved Inverse Photoemission from the Ag(100) Surface". In *Phys. Rev. B* **40**, 10238–10240. DOI: `10.1103/PhysRevB.40.10238` (1989) (cit. on pp. 42, 95).

[114] H.-C. Ploigt, C. Brun, M. Pivetta, F. Patthey, and W.-D. Schneider: "Local Work Function Changes Determined by Field Emission Resonances: NaCl/Ag(100)". In *Phys. Rev. B* **76**, 195404. DOI: `10.1103/PhysRevB.76.195404` (2007) (cit. on p. 42).

[115] K. Bobrov, A. J. Mayne, and G. Dujardin: "Atomic-Scale Imaging of Insulating Diamond through Resonant Electron Injection". In *Nature* **413**, 616–619. DOI: `10.1038/35098053` (2001) (cit. on p. 43).

[116] O. Yu. Kolesnychenko, Yu. A. Kolesnichenko, O. I. Shklyarevskii, and H. van Kempen: "Field-Emission Resonance Measurements with Mechanically Controlled Break Junctions". In *Phys. B Condens. Matter* **291**, 246–255. DOI: `10.1016/S0921-4526(99)02884-7` (2000) (cit. on pp. 43, 44).

[117] A. W. Dweydari and C. H. B. Mee: "Work Function Measurements on (100) and (110) Surfaces of Silver". In *Phys. Status Solidi A* **27**, 223–230. DOI: `10.1002/pssa.2210270126` (1975) (cit. on p. 43).

[118] L. Giordano, F. Cinquini, and G. Pacchioni: "Tuning the Surface Metal Work Function by Deposition of Ultrathin Oxide Films: Density Functional Calculations". In *Phys. Rev. B* **73**, 045414. DOI: `10.1103/PhysRevB.73.045414` (2006) (cit. on pp. 43, 44).

[119] M. Bieletzki et al.: "Topography and Work Function Measurements of Thin MgO(001) Films on Ag(001) by Nc-AFM and KPFM". In *Phys. Chem. Chem. Phys.* **12**, 3203. DOI: `10.1039/b923296f` (2010) (cit. on p. 44).

[120] T. Jaouen, P. Aebi, S. Tricot, G. Delhaye, B. Lépine, D. Sébilleau, G. Jézéquel, and P. Schieffer: "Induced Work Function Changes at Mg-Doped MgO/Ag(001) Interfaces: Combined Auger Electron Diffraction and Density Functional Study". In *Phys. Rev. B* **90**, 125433. DOI: `10.1103/PhysRevB.90.125433` (2014) (cit. on p. 44).

[121] S. Prada, U. Martinez, and G. Pacchioni: "Work Function Changes Induced by Deposition of Ultrathin Dielectric Films on Metals: A Theoretical Analysis". In *Phys. Rev. B* **78**, 235423. DOI: `10.1103/PhysRevB.78.235423` (2008) (cit. on pp. 44, 95).

[122] M. R. Castell: "STM and STS of Oxide Ultrathin Films". In *Encyclopedia of Interfacial Chemistry*, 332–337. DOI: `10.1016/B978-0-12-409547-2.12880-X` (2018) (cit. on p. 44).

[123] N. Nilius: "Properties of Oxide Thin Films and Their Adsorption Behavior Studied by Scanning Tunneling Microscopy and Conductance Spectroscopy". In *Surf. Sci. Rep.* **64**, 595–659. DOI: `10.1016/j.surfrep.2009.07.004` (2009) (cit. on p. 44).

[124] A. Gonchar, T. Risse, H. Freund, L. Giordano, C. Di Valentin, and G. Pacchioni: "Activation of Oxygen on MgO: O2-Radical Ion Formation on Thin, Metal-Supported MgO(001)Films". In *Angew. Chem. Int. Ed.* **50**, 2635–2638. DOI: `10.1002/anie.201005729` (2011) (cit. on p. 44).

[125] A. Hellman, S. Klacar, and H. Grönbeck: "Low Temperature CO Oxidation over Supported Ultrathin MgO Films". In *J. Am. Chem. Soc.* **131**, 16636–16637. DOI: `10.1021/ja906865f` (2009) (cit. on p. 44).

[126] L. Giordano, M. Baistrocchi, and G. Pacchioni: "Bonding of Pd, Ag, and Au Atoms on MgO(100) Surfaces and MgO/Mo(100) Ultra-Thin Films: A Comparative DFT Study". In *Phys. Rev. B* **72**, 115403. DOI: `10.1103/PhysRevB.72.115403` (2005) (cit. on p. 44).

[127] L. Giordano and G. Pacchioni: "Charge Transfers at Metal/Oxide Interfaces: A DFT Study of Formation of K delta+ and Au delta- Species on MgO/Ag(100) Ultra-Thin Films from Deposition of Neutral Atoms". In *Phys Chem Chem Phys* **8**, 3335–3341. DOI: `10.1039/B604288K` (2006) (cit. on p. 44).

[128] P. Hurdax, M. Hollerer, P. Puschnig, D. Lüftner, L. Egger, M. G. Ramsey, and M. Sterrer: "Controlling the Charge Transfer across Thin Dielectric Interlayers". In *Adv. Mater. Interfaces* **7**, 2000592. DOI: `10.1002/admi.202000592` (2020) (cit. on pp. 44, 81).

[129] G. Pacchioni and H. Freund: "Electron Transfer at Oxide Surfaces. The MgO Paradigm: From Defects to Ultrathin Films". In *Chem. Rev.* **113**, 4035–4072. DOI: `10.1021/cr3002017` (2013) (cit. on p. 44).

[130] G. Pacchioni, L. Giordano, and M. Baistrocchi: "Charging of Metal Atoms on Ultrathin MgO/Mo(100) Films". In *Phys. Rev. Lett.* **94**, 226104. DOI: `10.1103/PhysRevLett.94.226104` (2005) (cit. on p. 44).

[131] M. Hollerer et al.: "Charge Transfer and Orbital Level Alignment at Inorganic/Organic Interfaces: The Role of Dielectric Interlayers". In *ACS Nano* **11**, 6252–6260. DOI: `10.1021/acsnano.7b02449` (2017) (cit. on pp. 44, 95).

[132] C. Wäckerlin et al.: "Giant Hysteresis of Single-Molecule Magnets Adsorbed on a Nonmagnetic Insulator". In *Adv. Mater.* **28**, 5195–5199. DOI: `10.1002/adma.201506305` (2016) (cit. on p. 45).

[133] F. D. Natterer, K. Yang, W. Paul, P. Willke, T. Choi, T. Greber, A. J. Heinrich, and C. P. Lutz: "Reading and Writing Single-Atom Magnets". In *Nature* **543**, 226–228. DOI: `10.1038/nature21371` (2017) (cit. on p. 45).

[134] F. Donati et al.: "Magnetic Remanence in Single Atoms". In *Science* **352**, 318–321. DOI: `10.1126/science.aad9898` (2016) (cit. on p. 45).

[135] G. Cavallo, P. Metrangolo, R. Milani, T. Pilati, A. Priimagi, G. Resnati, and G. Terraneo: "The Halogen Bond". In *Chem. Rev.* **116**, 2478–2601. DOI: `10.1021/acs.chemrev.5b00484` (2016) (cit. on pp. 49–51, 54, 96, 97).

[136] J. P. D. C. Calupitan, O. Galangau, O. Guillermet, R. Coratger, T. Nakashima, G. Rapenne, and T. Kawai: "Scanning Tunneling Microscope Tip-Induced Formation of a Supramolecular Network of Terarylene Molecules on Cu(111)". In *J. Phys. Chem. C* **121**, 25384–25389. DOI: `10.1021/acs.jpcc.7b09370` (2017) (cit. on p. 52).

[137] G. R. Desiraju and R. Parthasarathy: "The Nature of Halogen-Halogen Interactions: Are Short Halogen Contacts Due to Specific Attractive Forces or Due to Close Packing of Nonspherical Atoms?" In *J.Am.Chem.Soc.* **111**, 8725–8726. DOI: `10.1021/ja00205a027` (1989) (cit. on pp. 52, 97).

[138] K-H. Chung, J. Park, K. Y. Kim, J. K. Yoon, H. Kim, S. Han, and S-J. Kahng: "Polymorphic porous supramolecular networks mediated by halogen bonds on Ag(111)". In *Chem. Commun.* **47**, 11492–11494. DOI: `10.1039/c1cc14679c` (2011) (cit. on pp. 52, 53, 60, 97, 98).

[139] J.K. Yoon, W-J. Son, K.-H. Chung, H. Kim, S. Han, and S.J. Kahng: "Visualizing Halogen Bonds in Planar Supramolecular Systems". In *J.Phys.Chem.C* **115**, 2297–2301. DOI: `10.1021/jp110891y` (2011) (cit. on pp. 52, 97).

[140] W.J. Jang, K.-H. Chung, M.W. Lee, H. Kim, and S. Lee: "Tetragonal porous networks made by rod-like molecules on Au(111) with halogen bonds". In *Applied Surface Science* **309**, 74–78. DOI: `10.1016/j.apsusc.2014.04.174` (2014) (cit. on pp. 53, 55, 98).

[141] Q. Shen, J.H. He, J.L. Zhang, K. Wu, G.Q. Xu, A. Thye, S. Wee, and W. Chen: "Self-assembled two-dimensional nanoporous molecular arrays and photoinduced polymerization of 4-bromo-4'-hydroxybiphenyl on Ag(111)". In *The Journal of Chemical Physics* **142**, 101902. DOI: `10.1063/1.4906116` (2015) (cit. on pp. 55, 64, 65).

[142] A. Abdulkarim, F. Hinkel, D. Jänsch, J. Freudenberg, F. E. Golling, and K. Müllen: "A New Solution to an Old Problem: Synthesis of Unsubstituted Poly(Para-Phenylene)". In *J. Am. Chem. Soc.* **138**, 16208–16211. DOI: `10.1021/jacs.6b10254` (2016) (cit. on p. 55).

[143] K. Friedrich, H. J. Sue, P. Liu, and A. A. Almajid: "Scratch Resistance of High Performance Polymers". In *Tribol. Int.* **44**, 1032–1046. DOI: `10.1016/j.triboint.2011.04.008` (2011) (cit. on pp. 55, 98).

[144] J. A. Lipton-Duffin, O. Ivasenko, D. F. Perepichka, and F. Rosei: "Synthesis of Polyphenylene Molecular Wires by Surface-Confined Polymerization". In *Small* **5**, 592–597. DOI: `10.1002/smll.200801943` (2009) (cit. on p. 55).

[145] W. Wang, X. Shi, S. Wang, M. A. Van Hove, and N. Lin: "Single-Molecule Resolution of an Organometallic Intermediate in a Surface-Supported Ullmann Coupling Reaction". In *JACS* **133**, 13264–13267. DOI: `10.1021/ja204956b` (2011) (cit. on pp. 55, 57, 64).

[146] A. Basagni, F. Sedona, C.A. Pignedoli, M. Cattelan, L. Nicolas, M. Casarin, and M. Sambi: "Molecules-oligomers-nanowires-graphene nanoribbons: a bottom-up stepwise on-surface covalent synthesis preserving long-range order". In *J. Am. Chem. Soc.* **137**, 1802–1808. DOI: `10.1021/ja510292b` (2015) (cit. on p. 55).

[147] S. Song, T. Kojima, T. Nakae, and H. Sakaguchi: "Wide Graphene Nanoribbons Produced by Interchain Fusion of Poly(p-Phenylene) via Two-Zone Chemical Vapor Deposition". In *Chem. Commun.* **53**, 7034–7036. DOI: `10.1039/C7CC02849K` (2017) (cit. on p. 55).

[148] Q. Fan, C. Wang, Y. Han, J. Zhu, W. Hieringer, J. Kuttner, G. Hilt, and M. Gottfried: "Surface-Assisted Organic Synthesis of Hyperbenzene Nanotroughs". In *Angew. Chem. Int. Ed.* **52**, 4668–4672. DOI: `10.1002/anie.201300610` (2013) (cit. on p. 55).

[149] Q. Fan, C. Wang, Y. Han, J. Zhu, J. Kuttner, G. Hilt, and M. Gottfried: "Surface-Assisted Formation, Assembly, and Dynamics of Planar Organometallic Macrocycles and Zigzag Shaped Polymer Chains with C-Cu-C Bonds". In *ACS Nano* **8**, 709–718. DOI: `10.1021/nn405370s` (2013) (cit. on pp. 55, 59).

[150] C.J. Judd, S. L. Haddow, N. R. Champness, and A. Saywell: "Ullmann Coupling Reactions on Ag(111) and Ag(110); Substrate Influence on the Formation of Covalently Coupled Products and Intermediate Metal-Organic Structures". In *Scientific Reports* **7**. DOI: `10.1038/s41598-017-13315-1` (2017) (cit. on p. 55).

[151] C.J. Judd, F.L.Q. Junqueira, S. L. Haddow, N. R. Champness, D.A. Duncan, R.G. Jones, and A. Saywell: "Structural characterisation of molecular conformation and the incorporation of adatoms in an on-surface Ullmann-type reaction". In *Commun. Chem.* **3**, 166. DOI: `10.1038/s42004-020-00402-0` (2020) (cit. on p. 58).

[152] S. Kawai et al.: "Organometallic Bonding in an Ullmann-Type On-Surface Chemical Reaction Studied by High-Resolution Atomic Force Microscopy". In *Small* **38**, 5303–5311. DOI: `10.1002/smll.201601216` (2016) (cit. on p. 58).

[153] M. Giovannantonio M.and Garah et al.: "Insight into Organometallic Intermediate and Its Evolution to Covalent Bonding in Surface-Confined Ullmann Polymerization". In *ACS Nano* **7**, 8190–8198. DOI: `10.1021/nn4035684` (2013) (cit. on p. 59).

[154] J. Dai, Q. Fan, T. Wang, J. Kuttner, G. Hilt, M. Gottfried, and J. Zhu: "The role of the substrate structure in the on-surface synthesis of organometallic and covalent oligophenylene chains". In *Phys. Chem. Chem. Phys.* **18**, 20627–20634. DOI: `10.1039/C6CP03551E` (2016) (cit. on p. 59).

[155] S. Grimme: "Semiempirical GGA-Type Density Functional Constructed with a Long-Range Dispersion Correction". In *J. Comput. Chem.* **27**, 1787–1799. DOI: `10.1002/jcc.20495` (2006) (cit. on p. 61).

[156] G. Henkelman, B. P. Uberuaga, and H. Jonsson: "A Climbing Image Nudged Elastic Band Method for Finding Saddle Points and Minimum Energy Paths". In *J. Chem. Phys.* **113**, 9901–9904. DOI: `10.1063/1.1329672.` (2000) (cit. on p. 61).

[157] J. Bjork, F. Hanke, and S. Stafstrom: "Mechanisms of Halogen-Based Covalent Self-Assembly on Metal Surfaces". In *J. Am. Chem. Soc.* **113**, 9901–9904. DOI: `10.1063/1.1329672.` (2000) (cit. on p. 62).

[158] L. Basagni A.and Ferrighi et al.: "On-surface photo-dissociation of C–Br bonds: towards room temperature Ullmann coupling". In *Chem. Commun.* **51**, 12593. DOI: `10.1039/c5cc04317d` (2015) (cit. on pp. 64, 65).

[159] Y. P. Zhang, J. H. He, G. Q. Xu, and E. S. Tok: "Architecturing Covalently Bonded Organic Bilayers on the Si(111)-(7x7) Surface via in Situ Photoinduced Reaction". In *J. Phys. Chem. C* **116**, 8943–8949. DOI: `10.1021/jp300173d` (2012) (cit. on p. 65).

[160] L. Leoni and A. Dalla Cort: "The Supramolecular Attitude of Metal–Salophen and Metal–Salen Complexes". In *Inorganics* **6**, 42–59. DOI: `10.3390/inorganics6020042` (2018) (cit. on pp. 67, 68, 101).

[161] H. Chen, Z. Sun, X. Liu, A. Han, and P. Du: "Cobalt–Salen Complexes as Catalyst Precursors for Electrocatalytic Water Oxidation at Low Overpotential". In *J. Phys. Chem. C* **119**, 8998–9004. DOI: `10.1021/jp511584z` (2015) (cit. on p. 67).

[162] Y. Feng, M. E. Lydon, and C. W. Jones: "Polymer Resin Supported Cobalt-Salen Catalysts: Role of Co (II) Salen Species in the Regioselective Ring Opening of 1,2-Epoxyhexane with Methanol". In *ChemCatChem* **5**, 3636–3643. DOI: `10.1002/cctc.201300578` (2013) (cit. on p. 67).

[163] P. G. Cozzi: "Metal–Salen Schiff Base Complexes in Catalysis: Practical Aspects". In *Chem Soc Rev* **33**, 410–421. DOI: `10.1039/B307853C` (2004) (cit. on p. 67).

[164] M. Viciano-Chumillas, J. Hieulle, F. Silly, and T. Mallah: "Compact Hydrogen-Bonded Self-Assembly of Ni(II)–Salen Derivative Investigated Using Scanning Tunneling Microscopy". In *J. Phys. Chem. C* **116**, 23404–23407. DOI: `10.1021/jp307168k` (2012) (cit. on p. 68).

[165] M. Viciano-Chumillas, D. Li, A. Smogunov, S. Latil, Y.J. Dappe, C. Barreteau, T. Mallah, and F. Silly: "Tailoring the Structure of Two-Dimensional Self-Assembled Nanoarchitectures Based on Ni–Salen Building Blocks". In *Chem. A European J.* **20**, 13566–13575. DOI: `10.1002/chem.201403169` (2014) (cit. on p. 68).

[166] S. Kuck, S.-H. Chang, J.P. Kloeckner, M. H. Prosenc, G. Hoffmann, and R. Wiesendanger: "Steering Two-Dimensional Molecular Growth via Dipolar Interaction". In *Chem. Phys. Chem* **10**, 2008–2011. DOI: `10.1002/cphc.200900281` (2009) (cit. on p. 68).

[167] M. S. Alam, A. Scheurer, and P. Saalfrank R. W.and Müller: "STM Analysis of a Chiral Helical Onedimensional Nickel(III) Coorination Polymer". In *Z. Für Naturforschung B* **63**, 1443–1446. DOI: `10.1515/znb-2008-1218` (2008) (cit. on p. 68).

[168] K. Lämmle, T. Trevethan, A. Schwarz, M. Watkins, A. Shluger, and R. Wiesen-
       danger: "Unambiguous Determination of the Adsorption Geometry of a Metal-
       Organic Complex on a Bulk Insulator". In *Nano Lett.* **10**, 2965–2971. DOI: `10.`
       `1021/nl101290t` (2010) (cit. on p. 68).

[169] S. Fremy, A. Schwarz, K. Lämmle, M. Prosenc, and R. Wiesendanger: "The Monomer-
       to-Dimer Transition and Bimodal Growth of Co–Salen on NaCl(001): A High Res-
       olution Atomic Force Microscopy Study". In *Nanotechnology* **20**, 405608. DOI: `10.`
       `1088/0957-4484/20/40/405608` (2009) (cit. on p. 68).

[170] S. Song et al.: "On-surface synthesis of graphene nanostructures with pi-magnetism".
       In *Chem. Soc. Rev.* **50**, 3238–3262. DOI: `10.1039/D0CS01060J` (2021) (cit. on p. 86).

[171] Science News: *Doped graphene nanoribbons with potential.* 2014. eprint: `https:`
       `//www.sciencedaily.com/releases/2014/09/140908083342.htm` (cit. on p. 86).

Acknowledgments